ADVANCED ANALYSIS OF THE SUB-GLACIAL ENVIRONMENT USING RADAR ECHO SOUNDING SIMULATIONS

by

Christopher Richard Pierce

A dissertation submitted in partial fulfillment
of the requirements for the degree

of

Doctor of Philosophy

in

Engineering - Applied Mechanics

MONTANA STATE UNIVERSITY
Bozeman, Montana

December 2024

©COPYRIGHT

by

Christopher Richard Pierce

2024

All Rights Reserved

DEDICATION

I dedicate this work to Dr. Chris Borstad. He gave me the opportunity to come to Montana State University and inspired my interest in glaciology. His untimely illness and passing should inspire us all to seize the day and pursue our passions. Rest In Peace, Chris.

ACKNOWLEDGEMENTS

This research was supported by the National Aeronautics and Space Administration (Award: 80NSSC20K1134), Korea Institute of Marine Science & Technology Promotion (KIMST) funded by the Ministry of Oceans and Fisheries (RS-2023-00256677; PM23020), the G Unger Vetlesen Foundation, and Montana State University Office for Research and Economic Development. KIMST and Canadian Helicopters Limited (CHL) provided additional logistics, equipment, and personnel supporting RES data collection over Thwaites Glacier. The Canadian Polar Continental Shelf Program (PCSP) provided logistics support for the Devon Island field season. Computational efforts were performed on the Tempest High Performance Computing System, operated and supported by University Information Technology Research Cyberinfrastructure at Montana State University.

I would like to acknowledge many individuals who contributed directly to this work. Dillon Buhl, Lucas Beem, Anja Rutishauser, Natalie Wolfenbarger, Jamey Stutz, Corey Skender, Clint Baumgartner, Joshua Brett, Dominic O'Rourke, Tony Harden, and John Bishop participated in the field seasons collecting data over Thwaites Glacier and Devon Island. Further, Dr. Christopher Gerekos, Greg Nguyen, and Dr. Kirk Scanlan provided valuable insights on many aspects of the data processing and analysis contained in this text.

Finally I would like to acknowledge my advisors Drs. Ed Adams and Mark Skidmore, as well as the rest of my Ph.D. committee Drs. Lucas Beem, Don Blankenship, Kevin Hammonds, and Ladean McKittrick. Their guidance has been critical to completing this work.

TABLE OF CONTENTS

1. INTRODUCTION 1

2. CHARACTERIZING SUB-GLACIAL HYDROLOGY USING RADAR SIMULATIONS 4

Contribution of Authors and Co-Authors 4
Manuscript Information 6
Abstract 7
Introduction 8
Simulation Methodology 10
Dielectric Material Model 13
Geometric Model 15
Surface Roughness 15
Simulation Radius 17
Channel Geometry 19
Simulated Data Processing 21
Hypothetical Simulation Cases 23
Results - Hypothetical Simulation Cases 23
Application to Thwaites Glacier 26
Study Area 27
THW2/ UBH0c/ X243a Simulation Methodology 28
THW2/ UBH0c/ X243a Simulation Results 30
Discussion 35
Conclusions 41

3. EXPLORING CANYONS BENEATH DEVON ICE CAP FOR SUB-GLACIAL DRAINAGE USING RADAR AND THERMODYNAMIC MODELING 43

Contribution of Authors and Co-Authors 43
Manuscript Information 44
Abstract 45
Introduction 45
Data and Methods 49
Radar Data and Methods 49
RES Simulation Method 51
2-D Thermodynamic Modeling Method 55
Results 59
RES Results 59
RES Simulations of Canyon B Topography 63

TABLE OF CONTENTS – CONTINUED

2-D Thermodynamic Model Results 65
Discussion 65
Existence of Liquid Hydrology 65
Thermodynamic Modelling and Sub-Glacial Hydrology 68
Impact of Topography on RES Interpretation 69
Conclusions 72
Acknowledgements 73
Appendix 74
Appendix A - Selected Radargrams, Reflectivity, and Specularity Content 74
Appendix B - Modeled Canyon Geometry 79
Appendix C - Basal Roughness Approximation 79

4. CHARACTERIZING THE SUB-GLACIAL ENVIRONMENT OF LOWER THWAITES GLACIER USING RADAR MODELING 86

Contribution of Authors and Co-Authors 86
Manuscript Information 88
Abstract 89
Introduction 89
Methodology 93
RES Data Collection and Processing 93
RES Simulations 94
Homogeneous Simulations 98
Evaluating Simulation Fit Quality 99
Results 101
RES Specularity Content 101
Comparing RES and Simulated Reflectivity 102
Homogeneous Fits 103
Hydrologic Fits 107
Substrate Transitions 109
Heterogeneous 111
Discussion 116
Geographic Interpretation of Bed Heterogeneity 116
Sensitivity of RES Simulations to Model Parameters 117
RES Simulation Limitations 120
Conclusions 121
Appendix 122
Appendix A - Homogeneous Fits 122
Appendix B - Hydrologic Fits 127

TABLE OF CONTENTS – CONTINUED

Appendix C - Substrate Transition Fits 130
Appendix D - Heterogeneous Fits 132

5. CONCLUSION 138

Future Work 139

REFERENCES CITED 140

LIST OF TABLES

Table Page

2.1 Summary of RES simulation parameters. Parameters were chosen to replicate helicopter-based MARFA ice sounding experiments. 13

2.2 Complex dielectric constants for materials in radar simulations [22, 29, 54, 65]. For each material, we chose a value within the range published in the literature. Further analysis of sensitivity to these material parameters is presented in the discussion. 14

2.3 Summary of RES simulation parameters for each channel geometry. 24

3.1 Summary of parameters as described in [67] used in RES simulations of *DEV3_PER0a_Y86a*. 52

3.2 Summary of parameters used in 2-D heat transfer model. 60

3.3 Model parameters used for each intersection between survey flight line and Canyon *B*. 66

4.1 Summary of parameters used in RES simulations of Thwaites Glacier. 97

4.2 Specularity content for various subsets of the 2020/2022 Thwaites Survey data. 102

4.3 Fit quality metrics for homogeneous simulation segments. Locations correspond to numbered locations in Fig. C8. 106

4.4 Fit quality metrics for heterogeneous simulation segments. Locations correspond to numbered locations in Fig. C8. 114

LIST OF FIGURES

Figure Page

2.1 2-D Conceptual model of a RES simulation, defined in the direction of flight: a) The material and geometric model for a radar observation. b) The radar's spherical wavefront is approximated as rays directed at facets within a footprint beneath the aircraft. The simulator calculates a reflected and transmitted field strength, based on the dielectric constant at the surface (ϵ_{ice}). We do not show the surface reflection for simplicity. c) The rays propagate through the ice, with a direction obeying Snell's Law. At the bed, reflected field strength and direction are controlled by dielectric contrast and incidence angle with the basal facet. d) The backscattered electric field strength (E_b) is approximated with the Stratton-Chu integral. e) The aircraft's position is incremented and the process is repeated. 11

2.2 Radar simulation geometry a) Flight path (red), aircraft / channel orientation, simulation radius (R) across model footprint. b) A flat canal with width c_w. c) Geometry of a Röthlisberger or round channel with width c_w. 16

2.3 a) Schematic of simulation geometry for an elliptical cross-section of the Röthlisberger channel at nadir. A second, smaller facet length scale l_{f2} is introduced to facilitate accurate representation of curvature and divergent reflection character. b) Relationship between R and l_{f2} is defined for a range of c_w. We seek to limit $R \leq 300m$ for computational efficiency, imposing an upper limit on l_{f2} when simulating Röthlisberger channels..... 20

2.4 Simulated along track R_{rel} for $20m$ channels compared to a dry substrate with a) $\sigma_{bed} = 0.2m$. b) $\sigma_{bed} = 1m$. All simulations had the same Gaussian roughness correlation length $l_c = 15m$..... 25

2.5 Positive correlation between c_w and R_{rel} for both Röthlisberger channels and flat canals. The increase in R_{rel} is much more pronounced for flat canals. 26

LIST OF FIGURES – CONTINUED

Figure Page

2.6 The grounding line region of Thwaites Glacier, with region of channelized hydrology proposed by [83] highlighted. UTIG MARFA radar survey lines collected between 2020 and 2022 are shown in grey. Likely high volume channel routes suggested by [31] are shown in blue, and the location of THW2/ UBH0c/ X243a is highlighted for reference. 28

2.7 Focused radargram for THW2/ UBH0c/ X243a. The bright bed reflection corresponding to the proposed channel location is boxed. Vertical lines represent extent of the flight line re-produced in simulations. 29

2.8 a) A $4km$ region from actual THW2/ UBH0c/ X243a radargram containing the [31] channel location. b) Simulated THW2/ UBH0c/ X243a radargram with no water, $\sigma_{bed} = 0.2m$. c) Bed relative reflectivity from the actual THW2/ UBH0c/ X243a. The proposed channel location is highlighted in red as the area of interest. d) Simulated THW2/ UBH0c/ X243a relative reflectivity with no water, $\sigma_{bed} = 0.2m$. The along-track location corresponding to the area of interest is highlighted in red. 31

2.9 a) Simulated radargram with a single 20m canal at the bed. b) Relative reflectivity for simulation with 20m canal at the bed. 32

2.10 R_{rel} for distributed hydrology simulations at $2300 - 2900m$ along-track. a) a 600m wet bed surface (Weertman sliding), b) 30 flat canals with $c_w = 10m$, c) 8 flat canals with $c_w = 30m$, d) 6 flat canals with $c_w = 50m$, e) the entire $600m$ area covered with a flat, specular water body (e.g. sub-glacial lake). 34

2.11 Mean difference between actual and simulated R_{rel} over the area of interest at $2300 - 2900m$, for all simulations of THW2/ UBH0c/ X243a. Positive error bars show the difference between mean and peak R_{rel} over $2300 - 2900m$. 35

2.12 Actual specularity content from THW2/ UBH0c/ X243a. 38

LIST OF FIGURES – CONTINUED

Figure Page

2.13 Dielectric contrast between liquid water ($\epsilon = 78$) and substrates with permittivity from $\epsilon = 2.7 - 36$. Example bed material permittivity ranges from [96] are provided as reference. 39

3.1 Map of airborne RES surveys using the UTIG MARFA instrument in 2018 (grey) and 2023 (red). Location of sub-glacial lakes (light blue) and brine network (dark blue) proposed by [78, 80] are near the summit of DIC. 48

3.2 Attenuation rate determined by linear regression fit of ice thickness vs. bed returned power (corrected for geometric spreading). The full RES survey is shown in blue, while the "Near Canyon" data (orange/red) is the subset of points located within $3km$ of Canyons A and B from Figs. 3.6a and b. 51

3.3 a) 3-D view of RES simulation DEM and flight path over canyon topography at *DEV3_PER0a_Y86a* (label "B" in Figs. 3.6a, b). Note that simulation increments y_i along the flight path are not drawn to scale. Actual simulated increments in y are $v_a/PRF = 1m$ (Table 3.1) b) Cartoon of ray tracing in a 2-D cross-section of a simulation. Given our simulation radius $R = 300m$ and $l_f = 5m$, returned power is estimated by tracing over 10^4 rays at each position increment y_i. 54

3.4 Representative model geometry is superimposed over actual canyon cross-section derived from radar bed and surface picks for *DEV3_PER0a_Y86a* (label "B" in Figs. 3.6a, b). Similar figures demonstrating modeled and actual canyon topography at all modeled radar transects are found in *Appendix B*. 57

3.5 Geothermal heat flux boundary conditions for *DEV3_PER0a_Y86a*. The Lachenbruch boundary condition exhibits large variations in heat flux along the x direction, which is dependent upon the canyon geometry. 59

LIST OF FIGURES – CONTINUED

Figure Page

3.6 a) Relative reflectivity and b) specularity content from the 2023 RES survey in the transition zone between the DIC summit and Sverdrup Glacier. The locations of A and B on *DEV3_PER0a_Y86a* are shown. The grey diamonds trace Canyon A's location from the hypothesized brine network to Sverdrup Glacier. c) 1-D focused radargram for *DEV3_PER0a_Y86a*. Points A and B are the canyon features mapped on panels a and b above. d) Relative reflectivity and specularity content for *DEV3_PER0a_Y86a*. e) and f) zoomed in images of Canyons A and B from the radargram in c). 62

3.7 Simulated relative bed reflectivity results along an $8km$ segment of *DEV3_PER0a_Y86a*, centered on Canyon B, a) with a $10m$ flat canal at the floor and b) with a frozen bed and no canal. c) and d) zoomed view of R_{bed} response near the bottom of Canyon B. 64

3.8 a) Modeled 2-D bed temperature profile locations in the Sverdrup transition zone. Colors indicate temperature of the Canyon B floor and terraces (constant boundary condition). The grayscale indicates ice thickness, derived from ArcticDEM [69] and bed elevation data provided in [78]. Location of [80] hypothesized brine network is shown in blue. b) Comparison of modeled bed temperatures for the Constant and Lachenbruch boundary conditions along Canyon B. The points represent the positions where the flight lines intersect Canyon B and bed temperatures were modeled. Shaded areas represent the modeled temperature range due to uncertainty in accumulation rate β. 67

A1 Radargram, reflectivity, and specularity content for *DEV3_PER0a_Y79a* 74

A2 Radargram, reflectivity, and specularity content for *DEV3_PER0a_Y80a* 75

A3 Radargram, reflectivity, and specularity content for *DEV3_PER0a_Y81a* 75

A4 Radargram, reflectivity, and specularity content for *DEV3_PER0a_Y82a* 76

A5 Radargram, reflectivity, and specularity content for *DEV3_PER0a_Y83a* 76

LIST OF FIGURES – CONTINUED

Figure Page

A6 Radargram, reflectivity, and specularity content for *DEV3_PER0a_Y84a* 77

A7 Radargram, reflectivity, and specularity content for *DEV3_PER0a_Y85a* 77

A8 Radargram, reflectivity, and specularity content for *DEV3_PER0a_Y86a* 78

A9 Radargram, reflectivity, and specularity content for *DEV3_PER0a_Y87a* 78

B1 Canyon *B* model geometry for *DEV3_PER0a_Y79a* 79

B2 Canyon *B* model geometry for *DEV3_PER0a_Y80a* 80

B3 Canyon *B* model geometry for *DEV3_PER0a_Y81a* 80

B4 Canyon *B* model geometry for *DEV3_PER0a_Y82a* 81

B5 Canyon *B* model geometry for *DEV3_PER0a_Y83a* 81

B6 Canyon *B* model geometry for *DEV3_PER0a_Y84a* 82

B7 Canyon *B* model geometry for *DEV3_PER0a_Y85a* 82

B8 Canyon *B* model geometry for *DEV3_PER0a_Y86a* 83

B9 Canyon *B* model geometry for *DEV3_PER0a_Y87a* 83

C1 a) Location of ATLAS/ICESat-2 photons (C-C') with Landsat-09 imagery from July 31,2023 as background [97]. Canyons, brine network, and Sverdrup Glacier are labeled for reference. b) Photon height and location of three sampled terraces. c) - e) show photon height $S(x)$ and smoothed height $S_{SG}(x)$ for each sample, with resulting calculated roughness σ 85

LIST OF FIGURES – CONTINUED

Figure Page

C1 The downstream region of Thwaites Glacier, with locations and specularity content of all UTIG survey lines from 2020 and 2022. The 30 simulated flight segments in this study are outlined in grey. Segments A-A', B-B', C-C' and D-D' are described in greater detail in the results section. The hypothesized channel routes from [31], subglacial lake locations from [91], and hydrological transition from [83] are also shown. The estimated grounding line location from [3] is shown for reference. The dividing line at 106.5° longitude is proposed in the results as the boundary between eastern and western Thwaites. 91

C2 Conceptual model of an RES simulation is depicted. a) Antenna position at height h is incremented in the y direction along a flight path above an ice and bed surface. b) A 2-D cross-section of the simulation is shown at a single position of the radar antenna in time and space, with location y_i. The radar directs an incident electromagnetic ray $\bar{k_{inc}}$ at each facet (length=l_f) within a footprint of radius R. The ray's direction and magnitude are traced through the ice and back to the surface, where the backscattered electric field $\bar{E_b}$ is estimated at the antenna. 95

C3 a) Focused radargram for the simulated segment between *A* and *A'*. The bright reflector is boxed. b) Graph of hydraulic potential, R_{bed} variation, and specularity content for the same simulated segment. c) Along-track reflectivity variation R_{bed} and simulated homogeneous $R_{bed,S}$. Locations *A* and *A'* correspond to the locations in Figs. C1 and C8. The hypothesized lake boundaries from [91] intersect this segment from $\sim 1500m$ to $7000m$ along-track. 105

C4 a) 1-D focused radargram for the $11km$ simulated segment from *B* to *B'* (see Figs. C1 and C8) The bright basal reflector is highlighted. b) Comparison of R_{bed} and $R_{bed,S}$ for the homogeneous simulation. c) Hydrologic simulation comparision of R_{bed} vs. $R_{bed,S}$, where the basal material is changed to liquid water ($\epsilon = 78$) from $-4.1km$ to $-1.8km$ along-track. 108

LIST OF FIGURES – CONTINUED

Figure Page

C5 a)1-D focused radargram for the $14km$ simulated segment from C to C' (Figs. C1 and C8) b) Comparison of along-track R_{bed} and $R_{bed,S}$ for the homogeneous scenario c) Specularity content from the RES data for the simulated segment d) R_{bed} vs. $R_{bed,S}$ comparison for a roughness only transition (constant ϵ_{sub}) e) R_{bed} vs. $R_{bed,S}$ comparison for a substrate material transition (coupled ϵ_{sub} and roughness change). 110

C6 Improvement for all simulations with hydrologic and substrate transition fits. The numbers correspond to simulated segment locations in Fig. C8. Segments 12 and 19 correspond to B to B' and C to C' in Figs. C1 and C8. 111

C7 a)1-D focused radargram and b) plot of R_{bed} and $R_{bed,S}$ for the simulated segment between D and D' exhibiting complex heterogeneity. D and D' correspond to locations in Figs. C1 and C8.....113

C8 Map of all simulated flight segments, categorized by fit quality. Grayscale background indicates MEaSURES ice speed in $m\,yr^{-1}$ [52, 73]. 115

C9 Fit quality metric dependence on a) ϵ_{sub} and b) σ_{bed} for homogeneous simulations of B to B'.....119

C10 Simulated segment 1, R_{bed} vs. $R_{bed,S}$ comparison 122

C11 Simulated segment 2, R_{bed} vs. $R_{bed,S}$ comparison 123

C12 Simulated segment 3, R_{bed} vs. $R_{bed,S}$ comparison 123

C13 Simulated segment 4, R_{bed} vs. $R_{bed,S}$ comparison 124

C14 Simulated segment 5, R_{bed} vs. $R_{bed,S}$ comparison 124

C15 Simulated segment 6, R_{bed} vs. $R_{bed,S}$ comparison 125

C16 Simulated segment 7, R_{bed} vs. $R_{bed,S}$ comparison 125

C17 Simulated segment 8, R_{bed} vs. $R_{bed,S}$ comparison 126

C18 Simulated segment 9, R_{bed} vs. $R_{bed,S}$ comparison 126

C19 Simulated segment 10, R_{bed} vs. $R_{bed,S}$ comparison 127

LIST OF FIGURES – CONTINUED

Figure Page

C20 Simulated segment 11, R_{bed} vs. $R_{bed,S}$ comparison 127
C21 Simulated segment 12, R_{bed} vs. $R_{bed,S}$ comparison 128
C22 Simulated segment 13, R_{bed} vs. $R_{bed,S}$ comparison 128
C23 Simulated segment 14, R_{bed} vs. $R_{bed,S}$ comparison 129
C24 Simulated segment 15, R_{bed} vs. $R_{bed,S}$ comparison 129
C25 Simulated segment 16, R_{bed} vs. $R_{bed,S}$ comparison 130
C26 Simulated segment 17, R_{bed} vs. $R_{bed,S}$ comparison 130
C27 Simulated segment 18, R_{bed} vs. $R_{bed,S}$ comparison 131
C28 Simulated segment 19, R_{bed} vs. $R_{bed,S}$ comparison 131
C29 Simulated segment 20, R_{bed} vs. $R_{bed,S}$ comparison 132
C30 Simulated segment 21, R_{bed} vs. $R_{bed,S}$ comparison 132
C31 Simulated segment 22, R_{bed} vs. $R_{bed,S}$ comparison 133
C32 Simulated segment 23, R_{bed} vs. $R_{bed,S}$ comparison 133
C33 Simulated segment 24, R_{bed} vs. $R_{bed,S}$ comparison 134
C34 Simulated segment 25, R_{bed} vs. $R_{bed,S}$ comparison 134
C35 Simulated segment 26, R_{bed} vs. $R_{bed,S}$ comparison 135
C36 Simulated segment 27, R_{bed} vs. $R_{bed,S}$ comparison 135
C37 Simulated segment 28, R_{bed} vs. $R_{bed,S}$ comparison 136
C38 Simulated segment 29, R_{bed} vs. $R_{bed,S}$ comparison 136
C39 Simulated segment 30, R_{bed} vs. $R_{bed,S}$ comparison 137

NOMENCLATURE

Symbol	Definition	Units
a	Time scale for radar observations along track (azimuth)	s
b	reference function amplitude scaling function	
B	Radar birefringent loss	W
B_w	Radar bandwidth	Hz
c	Speed of light in free space	$m\,s^{-1}$
c_b	Canyon bottom width	m
c_h	Channel height	m
c_p	Heat capacity	$J\,kg^{-1}\,K{-}1$
c_w	Channel width	m
d	Canyon depth	m
d_{ice}	Nominal ice thickness	m
$\bar{E}_{b,n}$	Backscattered electric field strength	$V\,m^{-1}$
$\bar{E}_{i,n}$	Incident electric field strength	$V\,m^{-1}$
$\bar{E}_{r,n}$	Reflected electric field strength	$V\,m^{-1}$
$\bar{E}_{t,n}$	Transmitted electric field strength from S_{ice} to $Sbed$	$V\,m^{-1}$
f_c	Radar central frequency	Hz
f_s	Sampling frequency	Hz
g	Radar chirp signal	
G	Geometric spreading loss	W
h	Aircraft height	m
$_j$	Fast-time (τ) incremental index	
k	Thermal diffusivity	$mm^2\,s^{-1}$
K	Thermal conductivity	$W\,m^{-1}\,K^{-1}$
$_k$	Azimuth time (a) incremental index	
$\bar{k}_{i,n}$	Wavevector from radar antenna to facet n on $Sice$	
$\bar{k}_{r,n}$	Reflected wavevector from facet on S_{bed} to S_{ice}	
$\bar{k}_{t,n}$	Transmitted wavevector from facet n on S_{ice} to S_{bed}	
L_a	Aperture length for SAR focusing	m
l_c	Roughness correlation length	m
l_f	Facet length	m
l_{f2}	Secondary facet length	m
$\langle N_{ice} \rangle$	One-way radar attenuation rate in ice	$dB\,km^{-1}$
P_r	Bed returned power	W
PRF	Pulse repetition frequency	Hz
Q	Geothermal heat flux	$mW\,m^{-1}\,K^{-1}$
R	Simulation radius	m
R_{abs}	Absolute reflectivity	dB
$R_{abs,0}$	Absolute reflectivity of frozen bed	dB

NOMENCLATURE – CONTINUED

R_{bed}	Bed relative reflectivity coefficient	
$R_{bed,S}$	Simulated bed relative reflectivity coefficient	
R_{pl}	Pulse limited radius	m
R_{rel}	Relative reflection coefficient	dB
r_{air}	one-way travel distance from radar to ice surface	m
r_{ice}	one-way travel distance from ice surface to target	m
RCM	range migration, number of discrete fast-time cells	
S	Radar system gain	W
S_{bed}	Discretized bed surface	
S_{ice}	Discretized ice surface	
S^{BM}	2-D topography matrix derived from BedMachine V2	m
S^{rad}	2-D topography matrix derived directly from radar data	m
S^{rough}	2-D matrix of random isotropic Gaussian roughness	m
T	Temperature	$^{\circ}C$
T_r	Radar receiving window	s
T_s	Ice surface temperature	$^{\circ}C$
$\tan\delta$	Loss tangent	
v	Aircraft velocity	$m\,s^{-1}$
$\bar{\mathbf{w}}$	Ice velocity vector	$m\,s^{-1}$
x	Cartesian spatial coordinate, across track	m
y	Cartesian spatial coordinate, along track	m
z	Cartesian spatial coordinate, elevation	m
z_0	Polynomial interpolation of ice elevation	m
z_s	Surface elevation	m
β	Ice accumulation rate	$m\,yr^{-1}$
ϵ_{H_2O}	Relative dielectric constant of water	
ϵ_{ice}	Relative dielectric constant of ice	
ϵ_{rock}	Relative dielectric constant of rock	
ϵ_{sub}	Relative dielectric constant of substrate	
η_{H_2O}	Refractive index of water	
η_{ice}	Refractive index of ice	
η_{rock}	Refractive index of rock	
θ	Canyon wall slope angle	rad
λ	Radar center wavelength	m
ξ_f	Focused radargram	$V\,m^{-1}$
ξ_{raw}	Raw radargram	$V\,m^{-1}$
ξ_{RC}	Range compressed radargram	$V\,m^{-1}$
ρ	Density	$kg\,m^{-3}$
σ_{bed}	Roughness amplitude for bed DEM	m
σ_{RS}	Standard deviation ratio between R_{bed} and $R_{bed,S}$	

NOMENCLATURE – CONTINUED

τ	Fast-time scale for returned radar echoes	s
τ_s	Fast-time value for radargram ice surface reflection	s
Υ	Radar pulse length	s
ϕ	1-D reference function for radargram focusing	
Φ	Slow-time Fourier transform of reference function ϕ	
Φ_{RS}	Pearson correlation coefficient	
χ_{RS}	Ratio of the total range between R_{bed} and $R_{bed,S}$	
ψ	Hydraulic potential	m
ω	Across track quadratic weighting function (values [0,1])	
$[\,]_{dB}$	denotes quantities expressed in decibels	
$\langle\,\rangle$	denotes a depth averaged quantity	

ABSTRACT

Sub-glacial conditions beneath large ice masses, especially the sub-glacial hydrological system, exert control on ice velocity and melting near the grounding zone. Despite the importance, the hydrological system beneath the Earth's polar ice sheets remain one of the greatest uncertainties when projecting climate-induced sea level rise. Analyzing variations in airborne ice penetrating Radar Echo Sounding (RES) reflectivity is an established technique for investigating sub-glacial topography. The high dielectric contrast between glacier ice, liquid water, and other substrate materials is exploited, with observations of elevated RES reflectivity commonly interpreted as sub-glacial water. Although this technique is powerful and enables wide geographic coverage, RES analysis is subject to several uncertainties which can lead to data misinterpretation.

In this work, a radar backscattering simulator is adapted to model RES reflections from sub-glacial water structures within defined topography. In the second chapter, the methodology is established, with outputs demonstrating that RES reflections from flat sub-glacial canals will be much brighter than from rounded Röthlisberger channels. Simulated outputs are then compared to actual reflectivity from an RES flight line collected over Thwaites Glacier in West Antarctica. Ultimately, the study demonstrates consistency between a bright reflector in the actual RES data and simulated flat canals or a sub-glacial lake.

In the third chapter, we combine the same simulation method with a 2-dimensional finite difference model of englacial temperatures. This study evaluates whether sub-glacial channels can exist in canyons identified beneath Devon Ice Cap in Nunavut, Canada (DIC). Results indicate that observed along-track variations in bed reflectivity could be induced by topography instead of extensive sub-glacial water, and basal temperatures could not support connected freshwater canals.

Finally, the fourth chapter applies the simulation methodology to over $400km$ of RES observations across the downstream region of Thwaites Glacier. Results demonstrate wide variability in the fit quality between actual and simulated RES reflectivity. These differences are interpreted as material homogeneity or heterogeneity in the glacial bed, correlating geospatially with some previous hypotheses for the Thwaites hydrological system. The simulation method may ultimately reduce ambiguity in RES interpretations by distinguishing between bed reflectivity variations induced by topography vs. material transitions.

1

INTRODUCTION

Understanding the sub-glacial environment, especially the distribution and extent of sub-glacial water, is vital to projecting ice sheet dynamics and sea-level rise in a changing climate [61]. The sub-glacial hydrological system directly influences grounding line retreat and shear stress at the ice/bed interface. Distributed water features (e.g. lakes and canals) provide basal lubrication [19, 36], while concentrated structures (e.g. Röthlisberger channels, Nye channels) transport basal meltwater toward the grounding line [83, 106, 107].

Airborne Radar Echo Sounding (RES) has been employed for several decades to explore polar sub-glacial hydrology [9, 30, 59, 80, 83, 89]. The technique is capable of scanning relatively large geographic footprints quickly, and low attenuation at common radar wavelengths ($\sim 2-5m$) enables imaging of bed surfaces beneath several thousand meters of ice. High dielectric contrast between water and common substrate materials such as bedrock and clay is often exploited to infer the location of sub-glacial water [65, 78, 83, 84, 107]. Interpretations of water beneath large ice sheets based on elevated RES reflected power is common, although ambiguity in both attenuation estimates and dielectric properties creates uncertainty [45, 96]. Conclusive validation of RES results is best accomplished through borehole access [12, 43, 71], although complex and expensive logistics often make such independent verification infeasible.

Given the challenges, advanced and cost-effective methods for enhancing the specificity and accuracy of RES interpretations are appealing. Backscattering simulators have proven especially useful in modeling radar returns for celestial targets [26, 77, 92], where it is common to test hypotheses with limited in situ evidence about surface or sub-surface characteristics. Each of these simulators functions similarly, by approximating RES returns as the aggregated

electromagnetic field reflected from a series of discrete facets in digital elevation model (DEM) [26, 77, 92]. The simulator in [26] is especially appealing to the study of sub-glacial environments using RES because it was designed to analyze layered targets using computationally efficient algorithms.

This dissertation demonstrates several use cases for an RES simulation method in the exploration of the sub-glacial environment. The simulator from [26] was adapted to model sub-glacial radar returns from the University of Texas Institute for Geophysics (UTIG) Multifrequency Airborne Radar Sounder with Full-phase Assessment (MARFA) instrument [10, 48]. In the second chapter, we establish the theoretical basis for the methodology, then compare theoretical returns from two common geometries in sub-glacial hydrology. This chapter ends by comparing real and simulated RES reflectivity for a $4km$ segment of data from Thwaites Glacier in West Antarctica. Possible constraints on hydrological features capable of producing the observed RES reflectivity profile are diagnosed.

The final two chapters apply the simulation methodology more broadly to evaluate sub-glacial hypotheses beneath the Devon Ice Cap (DIC) on Devon Island, Nunavut, Canada and Thwaites Glacier in West Antarctica. Both locations have been the subject of recent helicopter-based MARFA radar surveys. In Chapter 3, the potential for channelized hydrology within a system of canyons beneath the DIC is explored. This represents an extension of the hydrological hypothesis proposed in [79], which identifies a hypothesized distributed saline hydrological system draining from the DIC summit to Sverdrup Glacier. Sub-glacial temperatures are calculated using a 2-dimensional finite difference model as additional evidence for likely sub-glacial conditions. Both models appear to corroborate a conclusion that only a limited saline water system could exist within the DIC canyons.

The final chapter compares simulated RES outputs to real RES reflectivity across the downstream region of Thwaites Glacier. Thwaites Glacier is the largest in the Amundsen Sea Embayment in West Antarctica, and contains enough ice to raise global sea levels by

approximately $60cm$ [37, 55, 81, 108]. The glacier's geometry is recognized as inherently unstable, and the distribution of hydrological structures has been widely hypothesized [31, 51, 83, 91]. Simulated outputs are compared with real reflectivity from over $400km$ of RES survey data across the Thwaites downstream region. Results demonstrate relative homogeneity or heterogeneity in the basal environment, which varies geospatially across the study area. This is considered in the context of previous Thwaites hydrological studies and additional evidence in the 2020 and 2022 RES data.

This body of work demonstrates the potential for backscattering simulations as a tool in analyzing the sub-glacial environment from RES surveys. Each chapter builds progressively more complex use cases for the methodology. Several common themes arise, including the potential for topography to generate large variations in radar returns, and uncertainty in basal roughness at length scales near common ice penetrating RES wavelengths ($\sim 2 - 5m$). These represent ample opportunities for future research as methods and computational resources improve.

CHARACTERIZING SUB-GLACIAL HYDROLOGY USING RADAR SIMULATIONS

Contribution of Authors and Co-Authors

Manuscript in following chapter

Author: Chris Pierce

Contributions: prepared the original draft, wrote modifications to the simulator, led the design and execution of experiments, and participated in the field work to collect RES data from Thwaites Glacier.

Author: Christopher Gerekos

Contributions: contributed the original simulator software, assisted in experimental design, model validation, and provided significant editorial support.

Author: Mark Skidmore Contributions: provided oversight and partial funding, as well as significant editorial contributions.

Author: Lucas Beem

Contributions: provided important context for the project conceptualization, made significant editorial contributions, and led the field team responsible for RES data collection over Thwaites Glacier.

Author: Don Blankenship

Contributions: provided leadership support, funding, and programmatic resources for the investigation and RES data collection over Thwaites.

Author: Won Sang Lee

Contributions: provided funding and logistics support for the Thwaites RES data collection, as well as editorial contributions. EA provided significant editorial review and advisory support.

Author: Ed Adams

Contributions: provided significant editorial support and contributed to experimental design.

Author: Choon-Ki Lee

Contributions: made a significant contribution to planning and execution of the Thwaites Glacier RES survey, provided input on the simulation experimental design, and provided editoral support.

Author: Jamey Stutz

Contributions: participated in the collection and validation of RES data from Thwaites Glacier.

Manuscript Information

Chris Pierce, Christopher Gerekos, Mark Skidmore, Lucas Beem, Don Blankenship, Won Sang Lee, Ed Adams, Choon-Ki Lee, and Jamey Stutz

The Cryosphere

Status of Manuscript:
____ Prepared for submission to a peer-reviewed journal
____ Officially submitted to a peer-reviewed journal
____ Accepted by a peer-reviewed journal
_X_ Published in a peer-reviewed journal

Copernicus Publications
Volume 18, Issue 4
https://doi.org/10.5194/tc-18-1495-2024

Abstract

The structure and distribution of sub-glacial water directly influences Antarctic ice mass loss by reducing or enhancing basal shear stress, and accelerating grounding line retreat. A common technique for detecting sub-glacial water involves analyzing the spatial variation in reflectivity from an airborne radar echo sounding (RES) survey. Basic RES analysis exploits the high dielectric contrast between water and most other substrate materials, where a reflectivity increase $\geq 15\,dB$ is frequently correlated with the presence of sub-glacial water. There are surprisingly few additional tools to further characterize the size, shape, or extent of hydrological systems beneath large ice masses.

We adapted an existing radar backscattering simulator to model RES reflections from sub-glacial water structures using the University of Texas Institute for Geophysics (UTIG) Multifrequency Airborne Radar Sounder with Full-phase Assessment (MARFA) instrument. Our series of hypothetical simulation cases modeled water structures from $5m$ to $50m$ wide, surrounded by bed materials of varying roughness. We compared the relative reflectivity from rounded Röthlisberger channels and specular flat canals, showing both types of channels exhibit a positive correlation between size and reflectivity. Large ($> 20m$), flat canals can increase reflectivity by more than $20\,dB$, while equivalent Röthlisberger channels show only modest reflectivity gains of $8-13\,dB$. Changes in substrate roughness may also alter observed reflectivity by $3-6\,dB$. All of these results indicate that a sophisticated approach to RES interpretation can be useful in constraining the size and shape of sub-glacial water features. However, a highly nuanced treatment of the geometric context is necessary.

Finally, we compared simulated outputs to actual reflectivity from a single RES flight line collected over Thwaites Glacier in 2022. The flight line crosses a previously proposed Röthlisberger channel route, with an obvious bright bed reflection in the radargram. Through multiple simulations comparing various water system geometries, such as canals and sub-

glacial lakes, we demonstrated the important role that topography and water geometry can play in observed RES reflectivity. From the scenarios that we tested, we concluded the bright reflector from our RES flight line cannot be a Röthlisberger channel, but could be consistent with a series of flat canals or a sub-glacial lake. However, we note our simulations were not exhaustive of all possible sub-glacial water configurations.

The approach outlined here has broad applicability for studying the basal environment of large glaciers. We expect to apply this technique when constraining the geometry and extent of many sub-glacial hydrologic structures in the future. Further research may also include comprehensive investigations of the impact of sub-glacial roughness, substrate heterogeneity, and computational efficiencies enabling more complex and complete simulations.

Introduction

The size, shape, and distribution of sub-glacial water is important to ice dynamics, and remains a significant uncertainty in projecting sea level rise due to ice mass loss. Hydrological structures directly influence basal shear stress distribution, which defines the boundary condition for rheology at the ice/bed interface [7, 28, 36]. Widely distributed water has been shown to lubricate the base and weaken sediments [19, 36]. Conversely, narrow water channels may have little impact on shear stress at the bed [83], but act as conduits for concentrating meltwater produced upglacier. The size and location of such channels can directly influence grounding line retreat by controlling the volume of water transported to the grounding line [83, 106, 107].

Airborne Radar Echo Sounding (RES) is an established technique for studying sub-glacial hydrology throughout Earth's cryosphere [13, 65, 83]. Attenuation loss through ice at common radar wavelengths ($\sim 2 - 5m$) is relatively low, enabling reliable imaging of bed surfaces beneath ice masses several thousand meters thick. The dielectric contrast at

an ice / water interface is much higher than at an ice / rock interface, resulting in higher bed reflectivity when water is present. Additionally, some ice / water interfaces may be relatively smooth, depending on the geometry of the hydrological structure. These properties are commonly exploited in RES surveys to infer the location of sub-glacial water, based on reflected power $>\sim 15\,dB$ higher than the surrounding area [65, 78, 83, 84, 107].

Deducing the presence of water beneath large ice sheets using RES is relatively common, however methods for testing further hypotheses regarding size, geometry, or hydrological structure remain challenging. Direct observation of the glacier bed over any significant spatial extent is infeasible with current methods (e.g. drilling [71]), limiting our ability to calibrate radar returns to observed hydrological features.

This problem has precedent in inter-planetary science, where radar experiments are designed to test hypotheses with limited in situ evidence about surface or sub-surface characteristics. Backscattering simulators have proven especially useful in modeling radar returns for celestial targets [26, 77, 92]. Most simulators approximate a target surface as a series of flat facets acting as point backscatterers. The backscattered electric field strength at the radar antenna position is estimated with common mathematical approximations such as the Stratton-Chu integral. In such a point-scatterer formulation, facets much smaller than the radar wavelength (typically $< \lambda/10$) are required to approximate real world instrument results [26]. This constraint necessitates access to high-end computing resources, often making point-scattering radar simulators unrealistic for RES modeling.

However, as algorithms improve and computational costs decrease, it is increasingly attractive to attempt such a simulation method with ice penetrating RES problems. [26] described a simulation technique that is particularly intriguing for the study of sub-glacial hydrology. The methodology is unique in two distinct ways from other simulators, which are helpful in modeling ice penetrating RES. First, the simulator can estimate strength and direction of signals transmitted through multiple layered material interfaces. This makes it

conducive to targets such as the ice / bedrock system. Second, the algorithm allows phase to vary linearly across the facet (termed the Linear Phase Approximation or LPA). This feature enables modeling with significantly larger facets ($\sim \lambda$ or larger), drastically reducing computational resources needed for accurate simulations.

This paper demonstrates the radar simulator's application to geometric scattering from common hydrological targets: flat canals and Röthlisberger channels. We discuss the relevant parameters to achieve accurate model results, and illustrate its utility in interpreting radar signatures from hydrological features beneath the ice. Finally, as an example, we demonstrate simulations of a hydrological target beneath Thwaites Glacier. In the future, we anticipate the technique will have broad applicability to interpreting RES data in the context of the sub-glacial environment.

Simulation Methodology

Figure 2.1 describes a generic conceptual model for a RES radar simulation. Parameters were chosen to emulate a typical helicopter-based airborne radar survey with the University of Texas Institute for Geophysics (UTIG) Multifrequency Airborne Radar Sounder with Full-phase Assessment (MARFA) instrument [10, 48]. An ice surface and a bed surface are defined in a 3-dimensional Cartesian coordinate system, noted as S_{ice} and S_{bed} respectively. Figure 2.1a illustrates a 2-D representation of these surfaces, divided into N facets using a Delaunay triangulation algorithm, with characteristic length l_f. The linear phase approximation (LPA) employed in [26] allows the phase of the incident and reflected electric fields to vary linearly across each facet. LPA enables accurate simulations of coherent radar using relatively large facets ($\sim \lambda$ vs. $\lambda/10$ with other methods). The facet size should be constrained according to Eq. 2.1, where h is the aircraft height and λ is the free space radar wavelength [26]. For simulations presented here, $h = 500m$ and $\lambda = 5m$, consistent with a typical UTIG MARFA

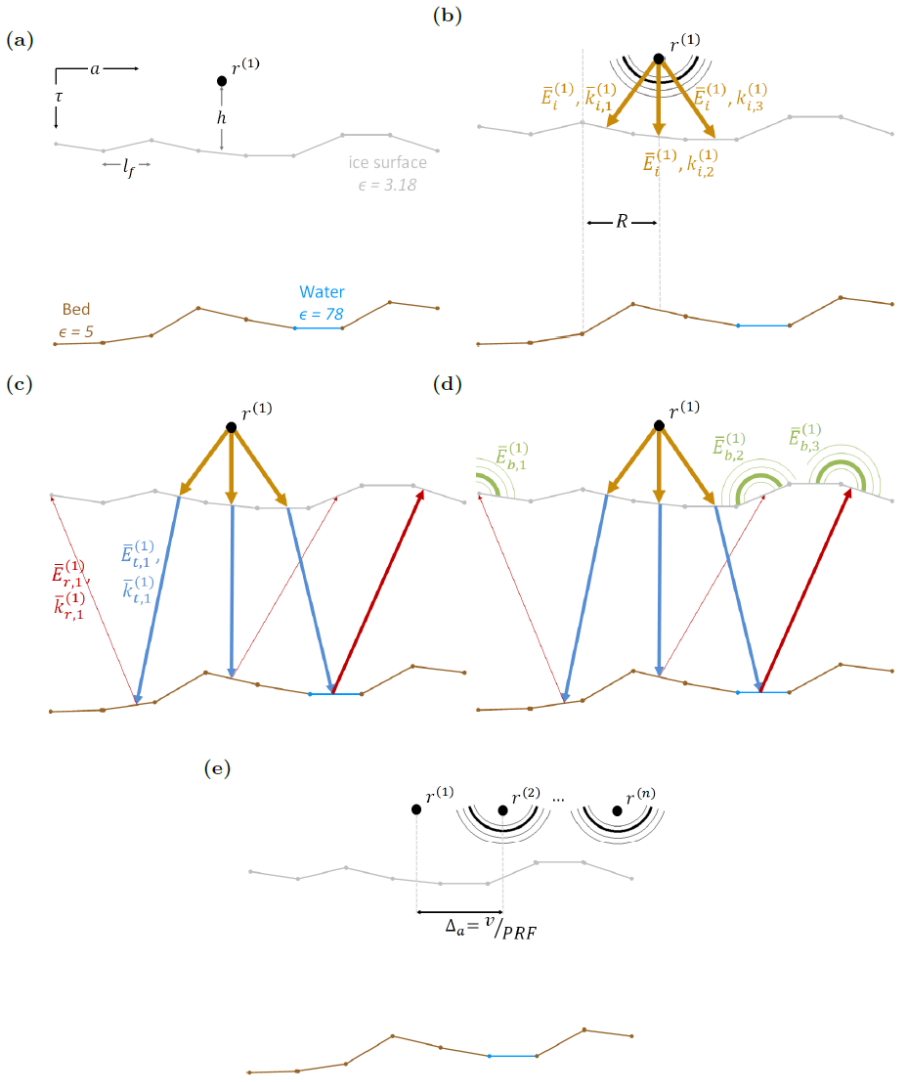


Figure 2.1: 2-D Conceptual model of a RES simulation, defined in the direction of flight: a) The material and geometric model for a radar observation. b) The radar's spherical wavefront is approximated as rays directed at facets within a footprint beneath the aircraft. The simulator calculates a reflected and transmitted field strength, based on the dielectric constant at the surface (ϵ_{ice}). We do not show the surface reflection for simplicity. c) The rays propagate through the ice, with a direction obeying Snell's Law. At the bed, reflected field strength and direction are controlled by dielectric contrast and incidence angle with the basal facet. d) The backscattered electric field strength (E_b) is approximated with the Stratton-Chu integral. e) The aircraft's position is incremented and the process is repeated.

helicopter experiment. $l_f = 5m$ was chosen, consistent with Eq. 2.1.

$$l_f \leq 0.2\sqrt{\lambda h/2} \tag{2.1}$$

The radar's spherical wavefront is simulated as a series of plane waves, with wavevectors $\bar{k}_i$ and field strength vector $\bar{E}_i$ directed at each ice surface facet within a radius R beneath the aircraft (Fig. 2.1b). A wider R will provide a more complete approximation of the radiated and returned electric field, but comes at a computational cost proportional to R^2. Therefore, R is chosen to balance these competing priorities, as we will discuss in detail.

Each ray's path is traced through transmission at S_{ice} using Snell's Law, then reflection from S_{bed} (Fig. 2.1c). In Fig. 2.1, the reflection from the ice surface is omitted for simplicity, since we are most concerned with reflections from the bed in this study. Reflected and transmitted field strengths ($\bar{E}_t$ and $\bar{E}_r$) are calculated from the real component of the dielectric constant at S_{ice} and S_{bed}, as discussed below. Attenuation loss between the surfaces is dependent on the complex component of the dielectric constant for ice [27], which is assumed constant over the short simulation distances presented here.

The total field at the radar antenna is then approximated as a summation of the backscattered electric fields ($\bar{E}_b$) from individual propagated waves using the Stratton-Chu integral (Fig. 2.1d). A detailed treatment of the simulation mathematics is presented in [26]. Because of higher ice/water dielectric contrast, rays reflecting from a facet within S_{bed} identified as water will have higher amplitude than facets comprised of rock.

The radar pulse repetition frequency (PRF) and aircraft velocity v determine the spatial resolution between radar observations in the azimuth direction, Δ_a, as shown in Fig. 2.1e. In the field, the MARFA instrument employs a native pulse repetition frequency (PRF) of 6400 Hz and peak power of 8 kW, then these observations are coherently stacked in post processing to achieve along track resolution of $1m$ before focusing [66]. We chose to simulate

Table 2.1: Summary of RES simulation parameters. Parameters were chosen to replicate helicopter-based MARFA ice sounding experiments.

Parameter	**MARFA Value** [a]
Geometric	
Aircraft height (h)	$500\,m$
Aircraft velocity (v)	$30\ m/s$
Instrument	
Center frequency (f_c)	60 MHz
Bandwidth (B_w)	15 MHz
PRF*	6.4 kHz (30 Hz)
Power*	8 kW (1.71 MW)
Sampling frequency (f_s)	50 MHz
Pulse length (Υ)	$1\ \mu s$
Receiving window (T_r)	$50\ \mu s$

[a]For fields marked with an asterisk, the native MARFA radar value differs from the parameter used in the simulation. Simulation parameters are in parentheses, and represent values after coherent pre-summing of raw MARFA data.

the final (stacked) PRF and power instead of the native parameters for computational efficiency.

Dielectric Material Model

It is instructive to consider energy returned to the radar as the superposition of dielectric and geometric effects. Dielectric effects result from material property changes at an interface, while geometric effects result from the orientation of the interface's topography and the radar antenna. We will begin by discussing the implications of dielectric parameters then move on

Table 2.2: Complex dielectric constants for materials in radar simulations [22, 29, 54, 65]. For each material, we chose a value within the range published in the literature. Further analysis of sensitivity to these material parameters is presented in the discussion.

Material	**Literature Range ϵ**	**Simulated ϵ**
Ice	$3.18 - 3.2$	$3.18 + .02i$
Water	$77 - 80$	$78 + .1i$
Bedrock	$4 - 6$	$5 + .15i$

to geometric considerations.

A material model is applied to the simulation, where all facets on S_{ice} and S_{bed} are assigned a complex dielectric constant, ϵ. The refractive index η for each material is derived from ϵ (Eq. 2.2). For simplicity, we have chosen a three material model consisting of ice, rock, and water, with dielectric constants as presented in Table 2.2. Facets across S_{ice} are assigned ϵ_{ice}. Facets on S_{bed} are assigned ϵ_{rock} unless they are part of a water structure, which are assigned ϵ_{H_2O}.

For a facet at nadir, absolute reflectivity R_{abs} results from contrast between the refractive indices of ice and the bed material (η_{ice} and η_{rock}, respectively). A horizontal facet assigned ϵ_{rock} will have a lower reflectivity than one assigned ϵ_{H_2O} by about $15\,dB$ (Eq. 2.2). Real RES instruments are rarely calibrated to measure absolute reflectivity, and thus changes in received power, corrected for ice attenuation loss and geometric scattering, are assumed proportional to relative changes in reflectivity at the bed (R_{rel}). This forms the basis for the widely accepted assumption that $R_{rel} \geq 10 - 15\,dB$ over surrounding reflections implies the presence of liquid water (e.g. [66, 80, 107]).

$$R_{abs,m} = \left(\frac{\eta_{ice} - \eta_m}{\eta_{ice} + \eta_m} \right)^2, \quad \eta_m = \sqrt{Re(\epsilon_m)}, \quad m = rock, H_2O \tag{2.2}$$

The simulations presented in this paper assume only the three materials described in Table 2.2, with well defined boundaries between hydrological and bedrock features. In real-world sub-glacial environments, additional material heterogeneity such as clays or hydrated tills exist, in addition to ambiguity in hydrological boundaries. We address the implications of this relatively simplistic material model in the *Discussion* section.

Geometric Model

We ultimately seek to develop the Stratton-Chu simulation method for constraining the extent and cross-sectional geometry of sub-glacial water features. Given this objective, it imperative to consider a menu of geometric constraints and how simulation parameters will emulate real-world RES returns from different targets. A basic simulation geometry for a hypothetical case is shown in Fig. 2.2a. These simulations consist of flat surfaces S_{ice} at elevation $0m$ and S_{bed} at $-d_{ice}$, where d_{ice} is the nominal ice thickness in m. The flight path is defined along the y-direction, with the radar's dipole antenna oriented along the x-direction. On the bed surface, a straight channel of width c_w is oriented perpendicular to the flight path.

Surface Roughness Small-scale topography variation below the radar's detection limit, which we will refer to as roughness, can impact reflectivity by diffusely scattering incident radar energy. To account for this effect, random isotropic Gaussian variation is introduced to both S_{ice} and S_{bed} via Eq. 2.3. l_c is the correlation length in both the x and y directions. To capture scattering behavior due to topography changes at the radar wavelength scale, l_c should be at least a few times the facet length l_f, while remaining near λ. In our simulations, both l_f and λ are $\sim 5m$, leading us to select $l_c = 15m$.

$$cov_{x,y} = \sigma_m e^{-(x^2+y^2)/l_c^2}, \quad m = ice, bed \tag{2.3}$$

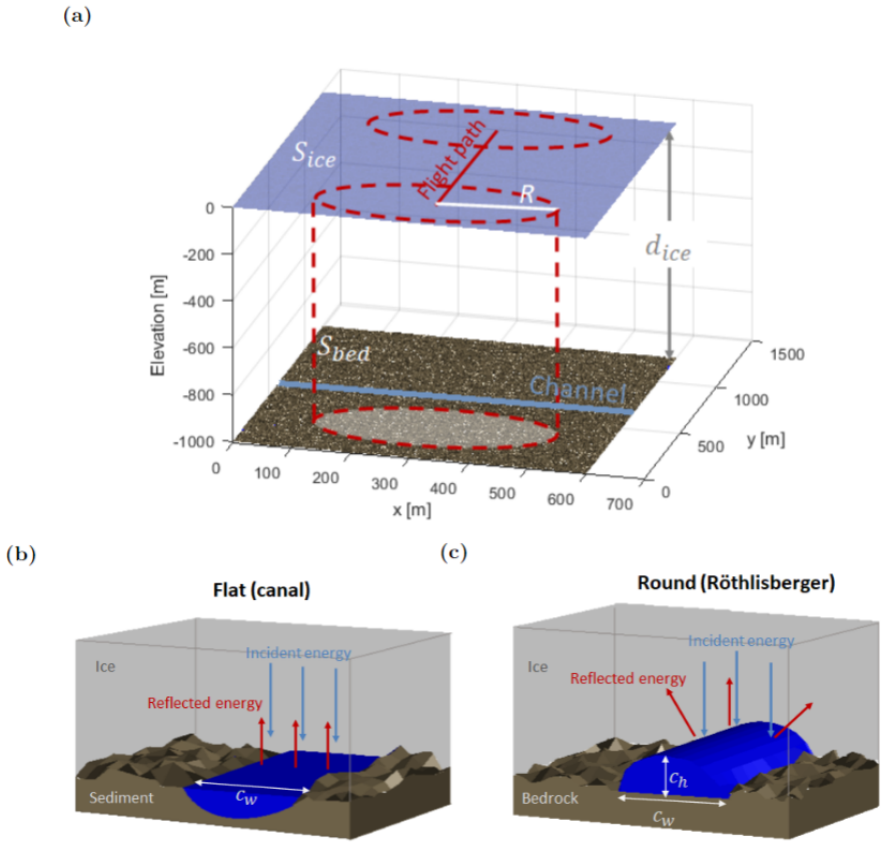


Figure 2.2: Radar simulation geometry a) Flight path (red), aircraft / channel orientation, simulation radius (R) across model footprint. b) A flat canal with width c_w. c) Geometry of a Röthlisberger or round channel with width c_w.

When we assume our surfaces are smooth relative to λ, we must add at least a negligible, non-zero roughness to avoid simulation artifacts, such as Bragg resonance [27]. We always make this assumptions for S_{ice}, therefore $\sigma_{ice} = 0.2m$ in all simulations presented here. We also use $\sigma_{bed} = 0.2m$ in "smooth" bed simulations.

[38] measured topography of recently deglaciated bedrock at high resolution in the Swiss Alps. They showed variations near $1m$ over horizontal distances of $15m$, which serves as our upper bound on σ_{bed}. We acknowledge this Alpine sub-glacial environment may differ considerably from common RES survey targets such as Thwaites Glacier in Antarctica. However, roughness studies from the Thwaites region integrate over long horizontal scales irrelevant to radar scattering [4, 35]. We proceed with the understanding that our range for σ_{bed} from $0.2m$ to $1m$ may represent an imperfect but reasonable range of expected variation in small-scale topography.

Simulation Radius An appropriate choice of simulation radius R is vital to accurately simulate radar geometric scattering from the sub-glacial environment. R defines the radius of a vertical cylinder, bounding the simulation scope at each aircraft position increment. If R is sufficiently large to capture the entire antenna beam pattern cast on the bed surface, then the simulation will provide a complete representation of off-nadir clutter and target range migration. In many layered radar simulation experiments, R is chosen primarily to capture off-nadir clutter at the sub-surface target's apparent depth [26]. Our experiments involve both a thick ice material layer and smooth S_{ice} relative to λ, limiting the impact of off-nadir clutter. Therefore, we base our choice for R on two alternative criteria:

- R must be greater than pulse limited radius R_{pl} at the glacier bed.
- R captures adequate range migration to facilitate along track focusing.

The first criterion assumes the majority of returned energy from a nadir-directed radar will come from within the pulse-limited footprint (R_{pl}) beneath the aircraft. Eq. 2.4

approximates an upper limit on R_{pl} for a radar instrument with bandwidth B_w, where c is the speed of light in a vacuum. Actual R_{pl} will always be smaller than Eq. 2.4 predicts, due to refraction at the air/ice interface. For our simulations, with $d_{ice} \sim 1000m$, $R_{pl} \approx 130m$ (Eq. 2.4). We consider this the minimum acceptable simulation radius, although clearly changes in aircraft height or simulated ice thickness will alter this limit.

$$R > R_{pl} \approx \sqrt{\frac{c\,(d_{ice} + h)}{B_w\,\eta_{ice}}} \tag{2.4}$$

An appropriate choice for R must also consider the desired range cell migration (RCM) at the bed surface. RCM is proportional to the change in physical distance a signal travels through air (r_{air}) and ice (r_{ice}) to reach a target as the radar moves past (Eq. 2.5). In Synthetic Aperture Radar (SAR) processing, an aperture length L_a is chosen with sufficient range cell migration to optimize along-track focusing. This process improves signal-to-noise ratio and along-track resolution [16]. In order to facilitate simulated data focusing, R must be greater than the aperture required for desired range migration. Selection of L_a and the focusing process is described at length in *Simulated Data Processing*.

$$RCM(y) = \frac{2f_s}{c}\left[(r_{air}(y) - h) + \eta_{ice}(r_{ice}(y) - d_{ice})\right] \tag{2.5}$$

Our simulations target 3 cells of range migration at the bed surface ($RCM(L_a) \geq 3$). For $d_{ice} = 1000m$, and sampling frequency $f_s = 50MHz$, this translates to $L_a = 277m$. All simulations presented here use $R = 300m$, meeting both the pulse-limited and range migration criteria. Real airborne RES focusing typically includes more range cell migration ($RCM(L_a) = 5$ fast-time samples for MARFA), however such a simulation radius would be computationally unrealistic. Therefore, our choice of R represents a compromise, and

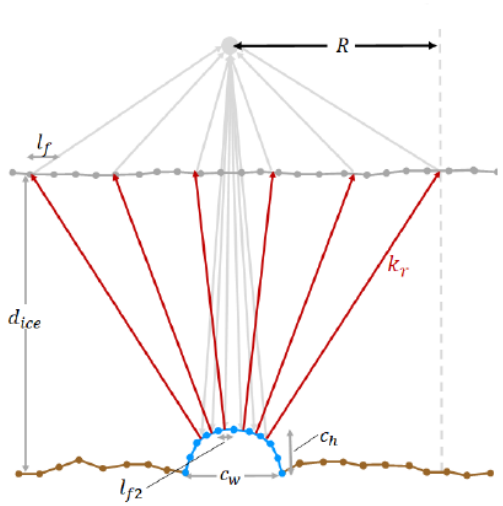
the implications will be discussed in the *Discussion* section. Simulations in thicker ice may require significantly larger R or further compromises in range migration.

Channel Geometry We seek to distinguish between two channel geometries common to sub-glacial hydrology. A canal-like structure (Fig. 2.2b) will have a flat cross-section and produce a specular reflection. This type of feature is common when the surrounding bed is comprised of sediment or other soft material, and the water pressure is high. Conversely, in a Röthlisberger channel (Fig. 2.2c), sub-glacial water carves a path through the ice above the bed surface ([76]). This type of channel is likely to form in areas where the substrate is impermeable bedrock with low water pressure [83, 102]. We have confined ourselves to Röthlisberger channels and flat canals in this study as examples of common large-scale hydrological structures. Other known hydrologic features, such as Nye channels, may appear radiometrically similar to small canals, depending on their size and the radar wavelength. As algorithms and computational power enable higher resolution models, additional sub-glacial structures are a logical extension of this work.

A Röthlisberger channel has a semi-elliptical cross section, with height c_h in addition to channel width c_w. We can infer from basic geometry it will reflect radar energy divergently (Fig. 2.2c), therefore the actual radar signature of a sub-glacial channel will be the superposition of its geometry and dielectric contrast. When representing the Röthlisberger curvature with flat facets, we must approximate the divergent scattering behavior by capturing reflections from multiple facets in the channel cross-section at nadir. In our simulations, we seek to capture reflections from at least the upper 6 facets within the simulation footprint as a reasonable estimate of Röthlisberger channel scattering (Fig. 2.3a).

Given our desired range of c_w and the constraint already imposed on R, it is clear that $l_f = 5m$ is too large to capture the scattering effect of a Röthlisberger channel. For our smallest channels ($c_w = 5m$), $l_f \leq .25m$ is required to capture the desired facet reflections

(a)



(b)

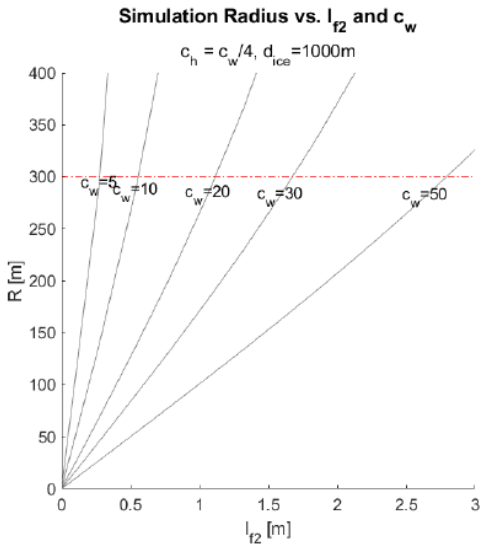


Figure 2.3: a) Schematic of simulation geometry for an elliptical cross-section of the Röthlisberger channel at nadir. A second, smaller facet length scale l_{f2} is introduced to facilitate accurate representation of curvature and divergent reflection character. b) Relationship between R and l_{f2} is defined for a range of c_w. We seek to limit $R \leq 300m$ for computational efficiency, imposing an upper limit on l_{f2} when simulating Röthlisberger channels

(Fig. 2.3b). Setting such a high resolution over all of S_{ice} and S_{bed} is computationally unrealistic and negates many of the benefits of the Stratton-Chu simulation method [26]. Therefore, we introduce a second facet length scale, l_{f2}, which defines the facet length on S_{ice} and S_{bed} only in a Röthlisberger channel location. l_{f2} has a maximum of $\sim c_w/20$, for $d_{ice} = 1000m$ and $c_h = c_w/4$ (Fig. 2.3b). When simulating flat canals, higher resolution channel facets are unnecessary due to the specular nature of the reflection, and therefore $l_{f2} = l_f$.

Simulated Data Processing

The simulator outputs rangelines, which represent the electric field strength vs. fast-time τ returned from a single pulse, at azimuth time a. τ is discretized into range bins (index j) with increments of $1/f_s$, where f_s is the sampling frequency. The rangelines are compiled sequentially in azimuth, or slow-time, into a 2-D raw radargram matrix (ξ_{raw}). Azimuth increments (index k) are equally spaced in time at $1/PRF$.

The rangelines are then focused using a version of the Range Doppler Algorithm (RDA) [16, 34]. We first perform range compression by convolving each raw rangeline with the complex conjugate of the radar chirp, $g(\tau)$ over the radar receiving window T_r. The operation is performed by multiplication in the fast-time frequency domain.

$$g(\tau) = e^{-i\pi\, B_w\, \tau^2/\Upsilon} \tag{2.6a}$$

$$\xi_{RC}(a,\tau) = \int_0^{T_r} \xi_{raw}(a, \tau+\tau')\, g(\tau)^* d\tau' \tag{2.6b}$$

We produce the focused radargram (ξ_f) by convolving the range compressed radargram (ξ_{RC}) with a 1-D reference function (ϕ) in along-track blocks (Eq. 2.7). The block size, L_a, for each fast-time value of τ is chosen such that range migration equals 3 fast-time samples.

Thus it is important to note that L_a increases with depth, and simulation radius R must be greater than the maximum anticipated L_a.

$$\xi_f(a,\tau) = \int_{-L_a/2}^{L_a/2} \xi_{RC}(a+a',\tau)\,\phi(a',\tau)^* da' \tag{2.7}$$

A deeper discussion of mathematics and block processing required for along-track focusing is presented in the *Appendix A1.*

In all radargrams, we convert fast-time to physical depth (d) and slow time to along-track distance (y) via Eqs. 2.8 and 2.9, where $\tau_s = 2h/c$ is the fast-time value for the surface reflection, and PRF is the radar pulse repetition frequency.

$$d_j = \frac{c}{2\eta_{ice}}(\tau_j - \tau_s), \quad \eta_{ice} = \sqrt{Re(\epsilon_{ice})} \tag{2.8}$$

$$y_k = k\,\frac{v}{PRF} \tag{2.9}$$

The focused field in ξ_f is converted to power in decibels. We define along-track bed reflectivity in absolute terms (R_{abs}) by taking the maximum reflected power beneath the ice surface (Eq. 2.10a). Relative reflectivity (R_{rel}) compares R_{abs} to the mean reflectivity for a simulation with the same σ_{bed} and σ_{ice}, but no channel present ($R_{abs,0}$). R_{rel} therefore measures the relative reflectivity gain observed by the radar due to the channel's presence vs. surrounding frozen bed material.

$$R_{abs}(y_k) = max\{RG_{f,\,dB}(d,y_k)\}, \quad d>0 \tag{2.10a}$$

$$R_{rel}(y_k) = R_{abs}(y_k) - mean\{R_{abs,0}\} \tag{2.10b}$$

Hypothetical Simulation Cases

A basic simulation geometry is shown in Fig. 2.2. Our hypothetical simulation cases consisted of flat surfaces S_{ice} and S_{bed} with elevations of $0m$ and $-1000m$, respectively. Each surface had isotropic Gaussian roughness as defined above. On the bed surface a single channel of width c_w was oriented perpendicular to the flight path. Channel cross-sections were either flat canal-like structures (Fig. 2.2b), or round Röthlisberger channels with channel height of $c_w/4$ (Fig. 2.2c).

A series of simulation experiments were run for both types of channels. Channel width and basal roughness were varied according to Table 2.3. Simulations involving flat canals used a single facet length of $5\,m$, while Röthlisberger channels necessitated a smaller l_{f2} in the channel location to accurately represent geometric scattering. Rangelines from each simulation were processed as described above, and along track bed reflectivity from the focused radargram R_{rel} was compared for various scenarios.

Results - Hypothetical Simulation Cases

Basal roughness (σ_{bed}) impacted the absolute reflectivity of the solid bed material in our simulations ($R_{abs,0}$), which we use as a baseline for calculating the relative impact of channels on the radar echo (Eq. 2.10b). Simulations excluding liquid water, with σ_{bed} of $0.2m$ and $1m$ produced mean $R_{abs,0}$ equal to $-107.9 \pm 2.5\,dB$ and $-114.1 \pm 2.4\,dB$, respectively.

Simulations of hypothetical Röthlisberger channels and flat canals with the same c_w demonstrate the distinctly different radar signatures expected for the two geometries. Figure 2.4 shows along-track relative reflectivity for the two channel types, with $c_w = 20m$, compared to a frozen substrate with no liquid water. Flat canals have a distinct peak centered near the canal location, with maximum $R_{rel} = 19.5\,dB$ when $\sigma_{bed} = 0.2m$ and $22.9\,dB$ when $\sigma_{bed} = 1m$. Regardless of roughness, a $20m$ flat canal influences the radar echo

Table 2.3: Summary of RES simulation parameters for each channel geometry.

Parameter	**All Simulations**	
Nominal ice thickness(d_{ice})	$1000\,m$	
Simulation Radius (R)	$300\,m$	
Facet length (l_f)	$5\,m$	
Range migration for SAR Aperture (RCM)	$3\,$cells	
Correlation length (l_c)	$15\,m$	
Surface roughness (σ_{ice})	$0.2\,m$	
Basal roughness (σ_{bed})	$0.2, 1\,m$	
Channel width (c_w)	$0, 5, 10, 20, 30, 50\,m$	
Parameter	**Flat Canals**	**Round Channels**
Channel facet size (l_{f2})	$5\,m$	$0.25 - 2.5\,m$
Channel height(c_h)	0	$c_w/4$

for a few hundred meters along-track. The reduced gain of $3.4\,dB$ for a canal surrounded by a smoother substrate is consistent with the higher absolute reflectivity of the surrounding surface as discussed above.

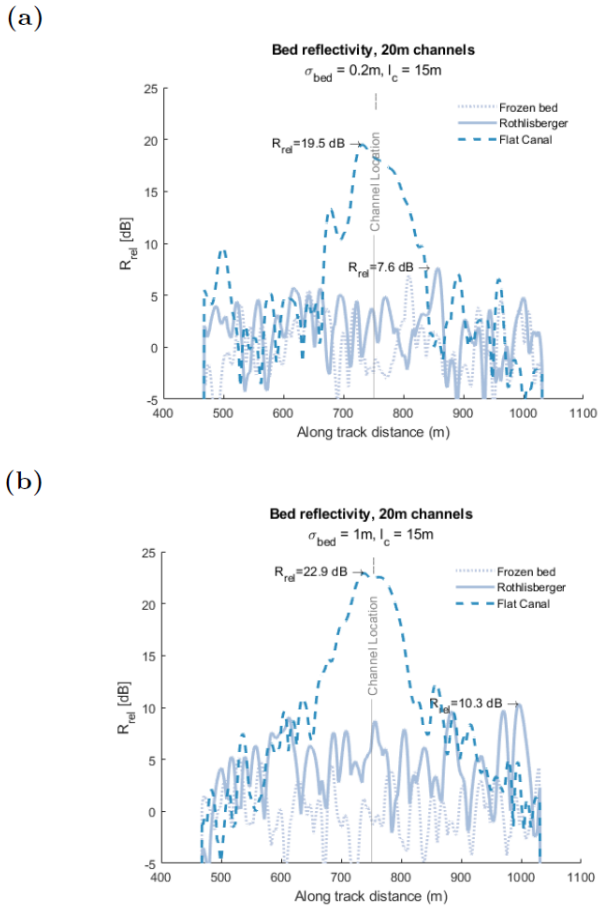


Figure 2.4: Simulated along track R_{rel} for $20m$ channels compared to a dry substrate with a) $\sigma_{bed} = 0.2m$. b) $\sigma_{bed} = 1m$. All simulations had the same Gaussian roughness correlation length $l_c = 15m$.

When flowing through a rough bed (Fig. 2.4b), a $20m$ simulated Röthlisberger channel increased along-track R_{rel} for more than $500m$. The maximum peak in R_{rel} for this channel is $10.3\,dB$, and occurring when the channel is far from nadir. In our smoother bed simulations, the same $20m$ Röthlisberger cross-section produced peak R_{rel} of only $7.6\,dB$ (Fig. 2.4a), which could be nearly indistinguishable from fluctuations in reflectivity from the frozen

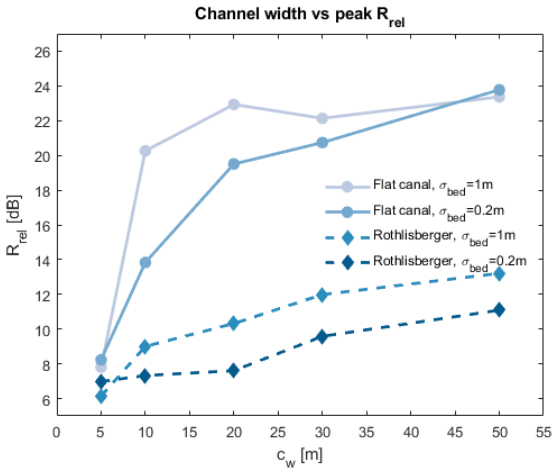


Figure 2.5: Positive correlation between c_w and R_{rel} for both Röthlisberger channels and flat canals. The increase in R_{rel} is much more pronounced for flat canals.

substrate. Larger Röthlisberger channels produce only moderate gains in R_{rel}, with the largest ($50m$) channels having peak $R_{rel} = 13.2\,dB$ (Fig. 2.5).

Figure 2.5 shows peak R_{rel} generally increases with width for both channels and canals, as an increasing proportion of the area within the radar's footprint contains liquid water. Flat canals exhibit a much stronger correlation between radar reflectivity response and c_w than Röthlisberger channels when $c_w < 20m$. At $c_w > 20m$, R_{rel} for flat canals increases more gradually as it appears to reach an asymptote of $\sim 24\,dB$.

Application to Thwaites Glacier

To demonstrate the simulator's utility in sub-glacial hypothesis testing, we compared simulated reflectivity to a single flight line collected with UTIG's 60 MHz MARFA instrument aboard an AS-350 B2 helicopter. The $16km$ line (THW2/ UBH0c/ X243a) was part of an airborne radar survey of Thwaites Glacier conducted between 2020 and 2022. The helicopter was flown at a nominal height of $500m$ above ground level with target velocity of $30m/s$. Precise aircraft positioning and orientation were recorded with an onboard Renishaw

laser altimeter, Trimble Net-R9 dual frequency GNSS, and Novatel SPAN IGM-1A inertial navigation, as described in [48].

Study Area

[83] first postulated a hydrological system dominated by channelized drainage within $\sim 45 - 70\,km$ of the Thwaites grounding line (Fig. 2.6), based on data interpretation from the extensive 2004-2005 Airborne Geophysics of the Amundsen Sea Embayment, Antarctica (AGASEA) radar survey. The hypothesis was largely derived from observations of high local bed reflectivity, combined with anisotropy in the radar specularity content. Specularity content measures the relative diffuse or specular nature of radar returned power. [83] postulated that extensive Röthlisberger channels could produce such radiometric signatures due to their geometric orientation.

[31] ran a suite of sub-glacial hydrology simulations to evaluate the probability of persistent channelization routes beneath Thwaites. Their analysis concluded that Thwaites' near terminus hydrology is most likely comprised of a few persistent, high volume channels flowing toward the central grounding zone. Two probable routes were proposed, also shown in Fig. 2.6.

Although evidence for sub-glacial hydrology dominated by channelization in this region of Thwaites Glacier is strong, structures such as canals or lakes are possible. For example, [91] identified a series of four active sub-glacial lakes that drained between June 2013 and January 2014. As seen in Fig. 2.6, at least one of these lakes is within the channelized region as defined in [83].

Our chosen flight line, THW2/ UBH0c/ X243a, transects one of the proposed [31] channel routes, and the radargram shows an isolated bright reflection coincident with this location, as shown in Fig. 2.7. Data from THW2/ UBH0c/ X243a were range compressed, corrected for geometric spreading loss and aircraft position, and focused in azimuth as

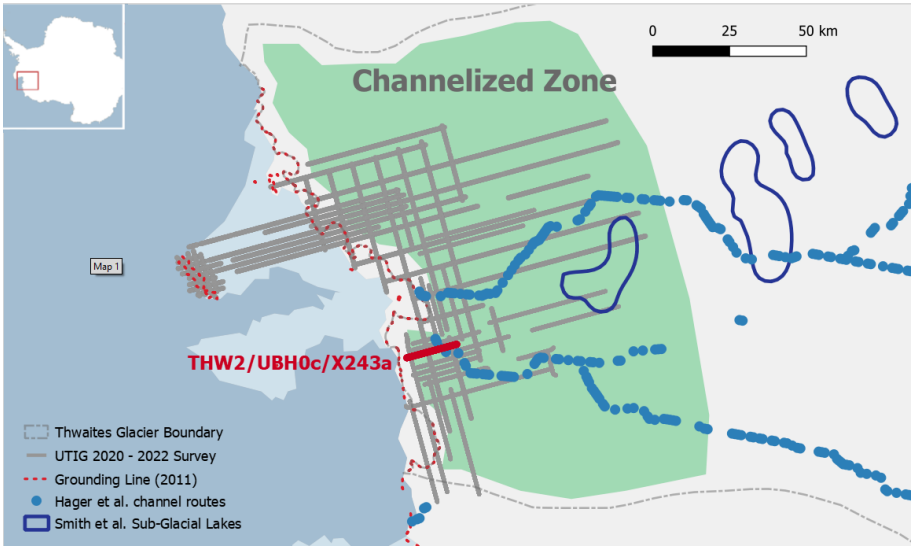


Figure 2.6: The grounding line region of Thwaites Glacier, with region of channelized hydrology proposed by [83] highlighted. UTIG MARFA radar survey lines collected between 2020 and 2022 are shown in grey. Likely high volume channel routes suggested by [31] are shown in blue, and the location of THW2/ UBH0c/ X243a is highlighted for reference.

described in [66]. This azimuth focusing is analogous to the procedure described in the *Simulated Data Processing* section, although a longer aperture sufficient for range migration of 5 cells is used.

The along-track surface and bed profiles were picked from the radargram. One-way attenuation loss of $13.8\,dB/km \pm 1.4\,dB/km$ was estimated using a spatially constrained linear regression model as outlined in [86].

THW2/ UBH0c/ X243a Simulation Methodology

We simulated a $4km$ segment of THW2/ UBH0c/ X243a containing the proposed channel, as depicted in Fig. 2.7. Along-track ice and surface elevations at nadir were calculated from the THW2/ UBH0c/ X243a focused radargram. From these data, we built elevation matrices for both the ice and bed surfaces (S_{ice}^{rad}, S_{bed}^{rad}) which vary in y according to the respective radar profiles, but have no x variation.

To build appropriate across-track (x) topography, separate 2-D topographic matrices

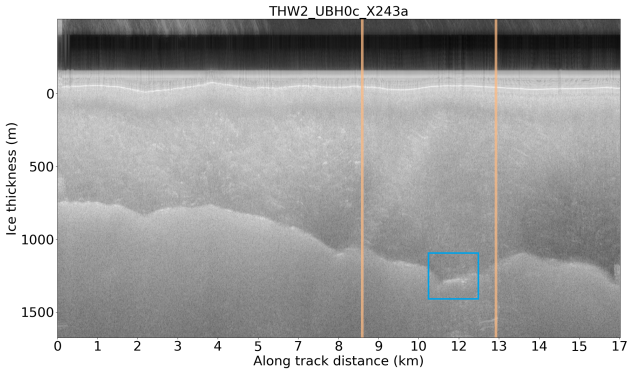


Figure 2.7: Focused radargram for THW2/ UBH0c/ X243a. The bright bed reflection corresponding to the proposed channel location is boxed. Vertical lines represent extent of the flight line re-produced in simulations.

were created from BedMachine V2 data (S_{ice}^{BM}, S_{bed}^{BM}) [56]. The radar and BedMachine derived topography were superimposed to create simulation surfaces S_{ice} and S_{bed} via Eq. 2.11, where ω is a quadratic weighting function varying between 1 at the surface edges and 0 at nadir. S^{rough} is an isotropic Gaussian surface, adding random roughness with $\sigma = 0.2m$ over correlation length $l_c = 15m$.

$$S = \omega\, S^{BM} + (1 - \omega)\, S^{rad} + S^{rough} - z_0(y) \tag{2.11}$$

In an ice penetrating RES survey, the aircraft attempts to "drape" the ice surface by flying at a constant height above ground level ($500m$ for UTIG helicopter based surveys). We simulate this with a polynomial interpolation of the radar-derived ice elevation along track, $z_0(y)$. For our simulations of THW2/ UBH0c/ X243a, z_0 is a 7th order polynomial, although in practice the polynomial order is somewhat subjective. The fitted function should approximate major terrain features in S_{ice}^{rad} with gentle elevation changes, consistent with actual aircraft operation.

$z_0(y)$ is subtracted from S_{ice} and S_{bed}, setting the average ice surface elevation to $\sim 0m$ (Eq. 2.11). The simulated aircraft elevation h is a constant $500m$. This approach preserves

known ice geometry at nadir, and minor topographic features appear as variations in aircraft range to target.

The dielectric material model was applied to S_{ice} and S_{bed} as described previously. We ran individual simulations using the same surfaces, varying the width and geometry of across-track oriented channels in the location identified in [31]. Relative bed reflectivity from each simulation result was compared to the actual relative reflectivity from the focused THW2/ UBH0c/ X243a radargram (Fig. 2.8c). The comparison between simulated and real data provides constraints on the extent and geometry of any real hydrological features at this location.

THW2/ UBH0c/ X243a Simulation Results

Figure 2.8 compares a $4km$ segment from THW2/ UBH0c/ X243a RES data with a simulation containing no water and $\sigma_{bed} = 0.2m$. There are two bright reflections in this section of the radargram (Fig. 2.8a). The first is centered around $1100m$ along-track with a maximum $R_{rel} = 11.6\,dB$. The second is a broad area of high reflectivity between $2300 - 2900m$, with R_{rel} peaks ranging from 13 to $15\,dB$ (Fig. 2.8c). This reflector coincides with the location of persistent Röthlisberger channelization proposed in [31], and is the primary area of interest along THW2/ UBH0c/ X243a for this study.

The radargram from our frozen bed simulation (Fig. 2.8b) captures the basic bed topography well, but along-track reflectivity is not always aligned with the real THW2/ UBH0c/ X243a radargram. Simulated reflectivity near $1100m$ is consistent with the real data, indicating that this reflectivity peak could be the result of geometric effects from topography, rather than dielectric contrast from a water feature. However, for the region between $2300 - 2900m$, mean simulated R_{rel} is $22.8\,dB$ below the value observed in the real THW2/ UBH0c/ X243a data (Fig. 2.11). In our material model, a gain of this magnitude could only be consistent with a change in dielectric properties from rock to liquid water. It

is also unlikely to be a Röthlisberger channel, since we have demonstrated such geometry is not conducive to increased reflectivity of more than $13.2\,dB$ for very large channels. We therefore propose that this basal reflector at $2300 - 2900m$ along-track could represent a specular hydrological structure, such as a flat canal, of unknown dimensions.

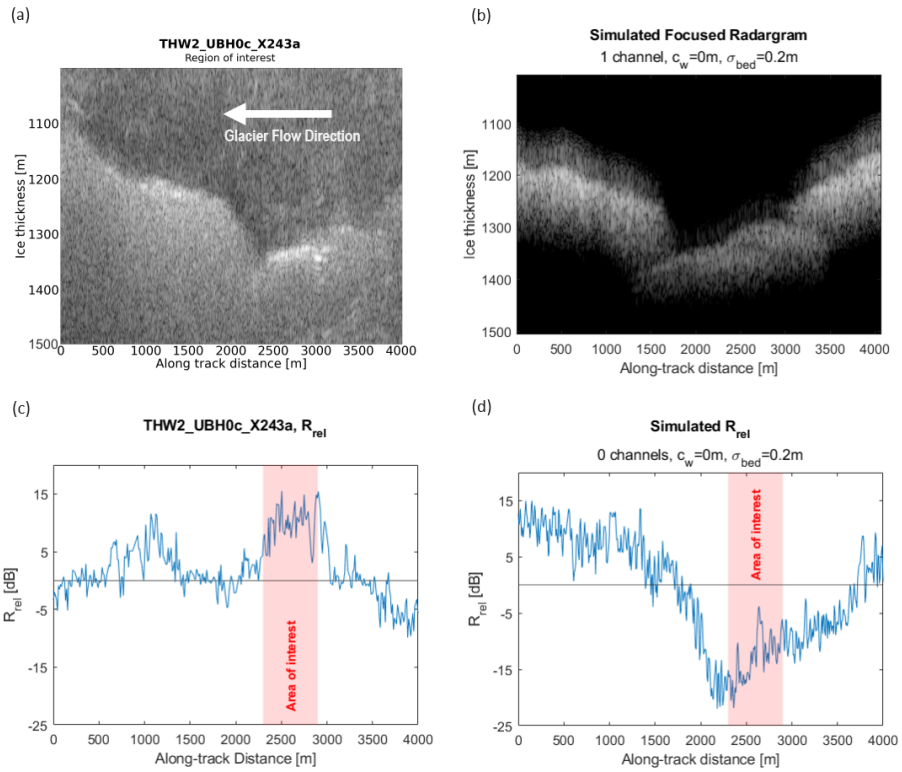


Figure 2.8: a) A $4km$ region from actual THW2/ UBH0c/ X243a radargram containing the [31] channel location. b) Simulated THW2/ UBH0c/ X243a radargram with no water, $\sigma_{bed} = 0.2m$. c) Bed relative reflectivity from the actual THW2/ UBH0c/ X243a. The proposed channel location is highlighted in red as the area of interest. d) Simulated THW2/ UBH0c/ X243a relative reflectivity with no water, $\sigma_{bed} = 0.2m$. The along-track location corresponding to the area of interest is highlighted in red.

When a single flat canal with $c_w = 20m$ was added to the simulation, we observe a peak R_{rel} of $6.8\,dB$ over a narrow $150m$ range along-track (Fig. 2.9). This reflectivity gain is consistent with our findings from hypothetical simulation cases described above. However, the gain in reflectivity and along-track extent are insufficient to match the reflectivity profile

observed in the real THW2/ UBH0c/ X243a RES data (Fig. 2.9b, Fig. 2.8c). Therefore, we conclude that the reflector cannot be a narrow, isolated flat canal.

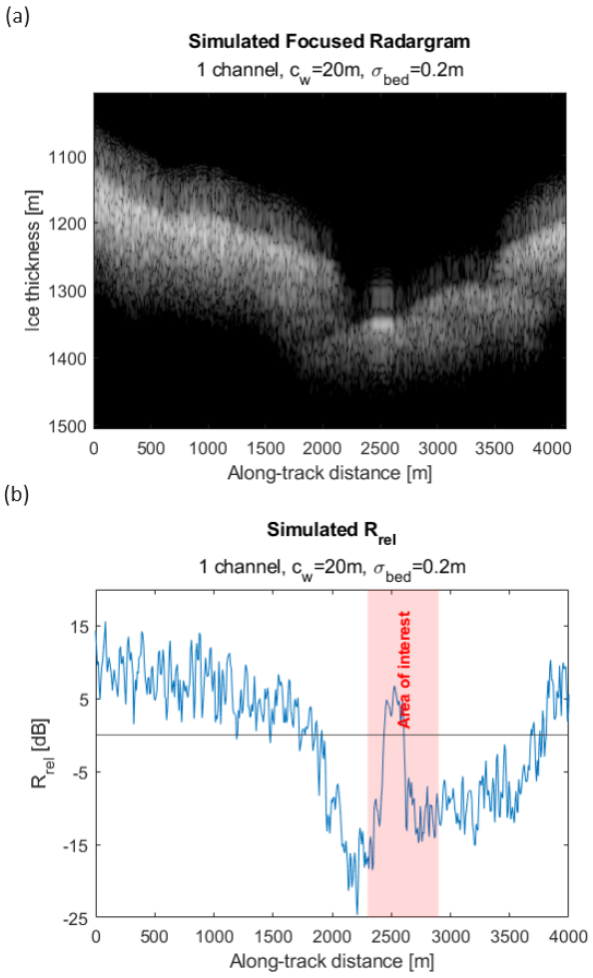


Figure 2.9: a) Simulated radargram with a single 20m canal at the bed. b) Relative reflectivity for simulation with 20m canal at the bed.

The above results imply the reflector between $2300 - 2900m$ may be a broader hydrological feature, such as an area with multiple flat canals. This hypothesis is compatible with the topographic context, given that it is in a low-lying area with steep topography just down-glacier. This is an ideal location for till and liquid water to accumulate if the ice exists at its pressure melting point.

Figure 2.11 compares the difference between THW2/ UBH0c/ X243a and simulated R_{rel} for five simulations of such hydrological features. We compare both the mean and peak difference in R_{rel} between $2300 - 2900m$, and conclude that each more closely approximates THW2/ UBH0c/ X243a than our frozen bed or single $20m$ channel simulation. First, we consider the glacier sliding condition originally proposed by [104]. In this scenario, a thin water film (perhaps a few centimeters thick) coats the basal interface. We model this by maintaining the basal topography with $\sigma_{bed} = 0.2m$, but all facets from $2300m \leq y \leq 2900m$ are assigned ϵ_{H_2O}. This simulation has a broad increase in reflectivity in the area of interest (Fig. 2.10a), however the mean R_{rel} between $2300 - 2900m$ is $9.4\,dB$ below the actual THW2/ UBH0c/ X243a value (Fig. 2.11).

Figure 2.10b shows simulated R_{rel} when 30 narrow, flat canals ($c_w = 10m$) were placed over the same $600m$ region along-track. This creates a region where 50% of the area is covered with $10m$ flat canals between areas of bed material with smooth basal roughness ($\sigma_{bed} = 0.2m$). Mean R_{rel} at $2300 - 2900m$ for this simulation is slightly higher than the Weertman film scenario in Fig. 2.10a, but still $8.2\,dB$ below the target R_{rel} from THW2/ UBH0c/ X243a.

The third simulation in Fig. 2.10c has 8 larger flat canals ($c_w = 30m$) evenly spaced across the same $600m$ region. This simulation has less water coverage than the $30x10m$ flat canal simulation (40% vs. 50%), yet the wider channels increased mean R_{rel} by $3.5\,dB$ (Fig. 2.11). This result reinforces that the shape of hydrological feature, not just the extent, makes a significant difference to the resulting reflectivity profile. Mean R_{rel} for the $8x30m$ simulation was $4.8\,dB$ below actual. When the geometry is changed to 6 canals of $50m$ (Fig. 2.10d), mean R_{rel} improves to just $2.3\,dB$ below THW2/ UBH0c/ X243a.

The final simulation includes a very broad area of specular ($\sigma_{bed} = 0m$) water covering the bed between $2300 - 2900m$. Due to its size, we refer to this feature as the "$600m$ lake" in Figs. 2.10 and 2.11. Mean R_{rel} over $2300 - 2900m$ for this simulation deviates by only $0.6\,dB$

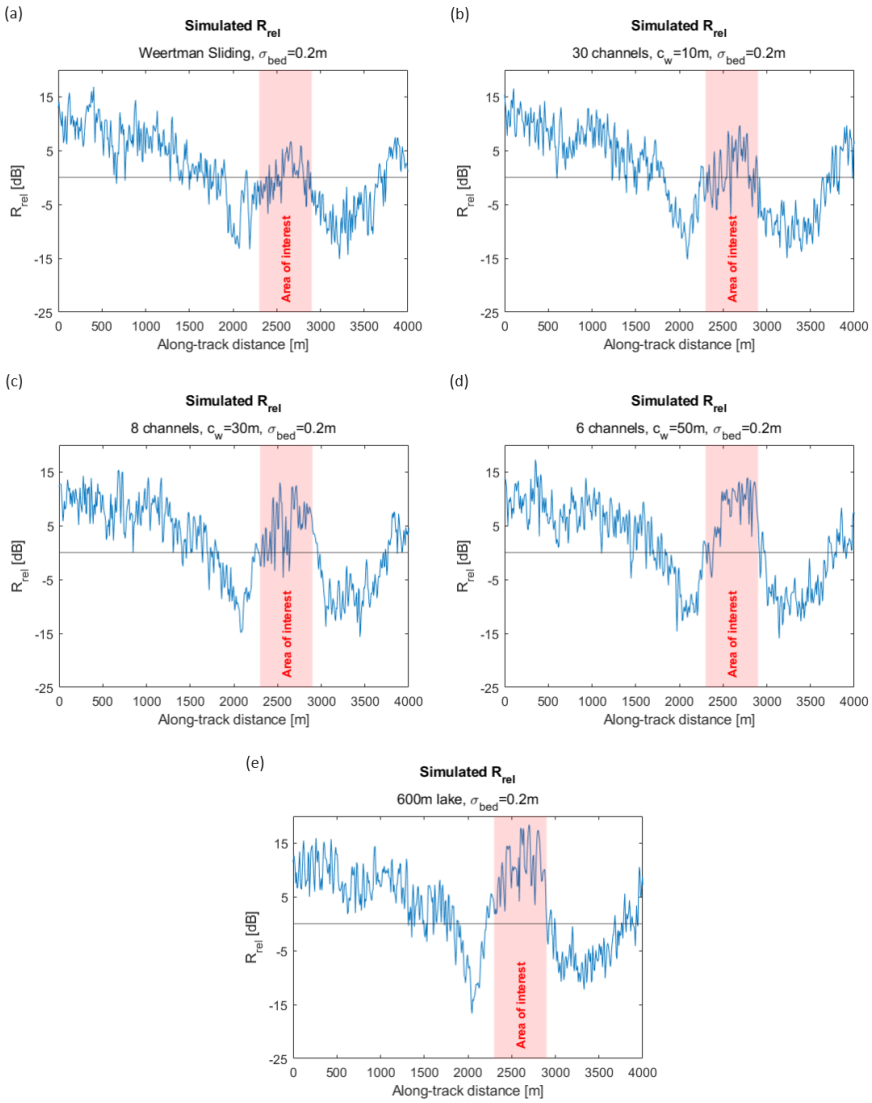


Figure 2.10: R_{rel} for distributed hydrology simulations at $2300 - 2900m$ along-track. a) a 600m wet bed surface (Weertman sliding), b) 30 flat canals with $c_w = 10m$, c) 8 flat canals with $c_w = 30m$, d) 6 flat canals with $c_w = 50m$, e) the entire $600m$ area covered with a flat, specular water body (e.g. sub-glacial lake).

from the actual THW2/ UBH0c/ X243a data. However, this $600m$ lake simulation includes several peaks as high as $18\,dB$, which is $3\,dB$ higher than the maximum peaks observed in THW2/ UBH0c/ X243a. The maximum R_{rel} from both the $8x30m$ and $6x50m$ simulations more closely matched the peaks observed in THW2/ UBH0c/ X243a.

We infer our feature at $2300 - 2900m$ could be a wide area of sub-glacial water. Of the scenarios we tested, simulated reflectivity was most consistent with canals averaging $\sim 30 - 50m$, with at least 50% water coverage, or a sub-glacial lake. Although THW2/ UBH0c/ X243a and our simulations demonstrate similar reflectivity profiles, we have not explored a comprehensive range of bed materials or water geometries. In the *Discussion* section, we address these omissions and the resulting limitations.

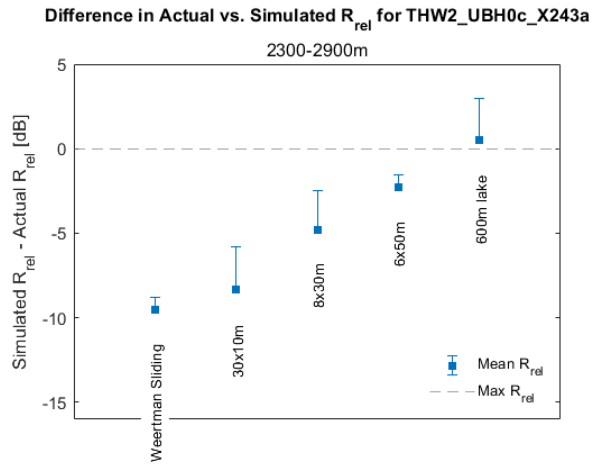


Figure 2.11: Mean difference between actual and simulated R_{rel} over the area of interest at $2300 - 2900m$, for all simulations of THW2/ UBH0c/ X243a. Positive error bars show the difference between mean and peak R_{rel} over $2300 - 2900m$.

Discussion

Our comparison of Röthlisberger vs. flat canal reflectivity implies that a real world Röthlisberger channel, even one of significant size, may not exhibit an obvious reflectivity increase. Röthlisberger channels will scatter energy divergently (Fig. 2.2c), therefore we see

a smaller magnitude impact to R_{rel} over a greater distance than an equivalent flat canal. The simulator also demonstrates the radar's sensitivity to relatively narrow, flat canals. A single canal $\sim 10m$ can exhibit a reflectivity peak $> 15\,dB$ (Fig. 2.5, *Flat canal*). Such a hydrological feature would cover $< 5\%$ of the radar's pulse-limited footprint under $1000m$ of ice.

In our simulations of hypothetical cases, increasing σ_{bed} from $0.2m$ to $1m$ reduced radar echo power by $6.2\,dB$. These results are intuitive. Scattering loss from a rougher surface will be larger and more variable, resulting in lower absolute reflectivity. Increasing roughness also alters the geometric contrast between the hydrological feature and surrounding material. The effect is most pronounced for flat canals with $c_w = 10 - 20m$. The impact of the bed roughness near flat canals diminishes as c_w exceeds $30m$, when reflected energy from the water feature dominates the radar return.

Our examination of roughness in this study was deliberately limited, as the relationship between roughness and scattering is complex and dependent on correlation length l_c. [4] and [65] each calculated wide ranges in RES-derived roughness across Antarctica. Roughness in these studies was measured with $l_c > 1km$. Our method for building simulated ice and bed surfaces directly incorporates RES observations of topography with resolution $l_f = 5m$ (see *THW2/ UBH0c/ X243a Simulation Methodology*). Therefore, any relationship between scattering and large scale roughness, as defined in these previous studies, is captured explicitly in our simulations.

Smaller scale sub-glacial roughness ($l_c <$ a few wavelengths) is more challenging to measure directly, therefore actual values are poorly constrained. Our hypothetical case simulations demonstrate bed roughness over $l_c = 15m$ may alter radar echoes without a change in dielectric properties. This is consistent with [65], who calculated theoretical scattering loss due to roughness could exceed $20\,dB$ when $l_c << 1^{st}$ Fresnel zone. A comprehensive examination of basal roughness, incorporating a broad range of both l_c and

σ_{bed} is possible with our simulation method. Such an investigation is an active area of interest for future work. Our limited current examination of roughness demonstrates that RES detection of sub-glacial water must be nuanced. Large changes in R_{rel} may constitute a liquid water signature, but could also indicate spatial heterogeneity in roughness or substrate material.

Given the limited reflectivity response from Röthlisberger channels, more advanced analysis techniques may be required to detect and characterize them accurately. This could include examination of specularity content as described in [84]. Specularity content quantifies the diffuse or specular quality of radar reflections by comparing returned power over two different SAR apertures. [83] argued that specularity content from Röthlisberger channels will be orientation dependent; high values are expected if the radar path is aligned along the channel, and lower values if the path is transverse to it. By contrast, flat interfaces such as canals and lakes should exhibit high and isotropic specularity content. Although our simulation methodology produces a focused product, it requires a simulation radius R greater than the SAR aperture L_a. Current computational constraints limit our choice of R to well below the aperture length of $2km$ recommended in [84]. Therefore, although simulating specularity content would be a valuable advance, we have left it to a future study.

Our THW2/ UBH0c/ X243a simulations from Thwaites Glacier demonstrate the reflectivity magnitude may be consistent with a wide, flat water feature surrounded by bedrock. Although we did not simulate specularity content, we observe a prominent peak in actual specularity content from THW2/ UBH0c/ X243a (Fig. 2.12). This observation could support the hypothesis that the reflector at $2300 - 2900m$ is a series of flat canals or a lake, since THW2/ UBH0c/ X243a is transverse to the channelized flow hypothesized in [31] (Fig. 2.6). An orthogonally oriented radar transect could enable a more definitive diagnosis of the hydrological feature.

Further, while our flat canal or lake configurations appear likely, we cannot preclude all

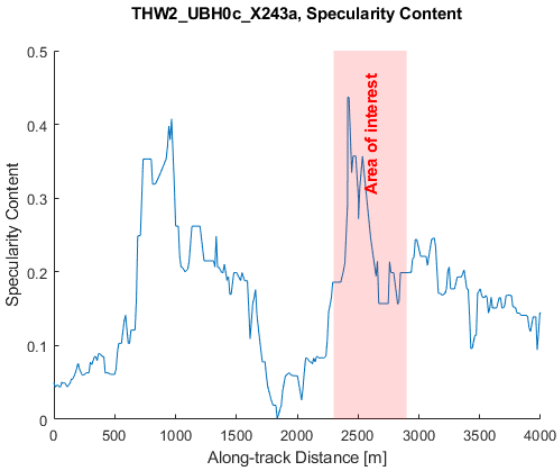


Figure 2.12: Actual specularity content from THW2/ UBH0c/ X243a.

competing hypotheses without exploring many additional scenarios beyond the scope of this work. Other water geometries, such as Nye channels or water sheets [15], combined with a broader range of roughness length scales, could fit the original THW2/ UBH0c/ X243a reflectivity profile. Future work should identify computational or process efficiencies to allow comprehensive coverage of all possible simulation variables.

The material model in this study was also deliberately simple. Many possible bed materials exist, ranging from frozen bedrock to clays with real dielectric constants between $2.7-36$ (Fig. 2.13) [11, 65, 96]. As we demonstrated in the frozen bed simulation, the feature at $2300-2900m$ requires an apparent reflectivity gain of $22.8\,dB$ over the surrounding substrate. Roughness may contribute some of this difference, however the observation is most consistent with a significant material transition. Figure 2.13 shows dielectric contrast between sub-glacial water and most clays or hydrated tills is less than $10\,dB$, making them unlikely bed materials. Conversely, substrates with the lowest dielectric constants are generally frozen, and therefore inconsistent with the presence of liquid water. These constraints limit the likely substrates to a narrow range of materials with $\epsilon \sim 5$, including saturated bedrock or hydrated tills with low permittivity.

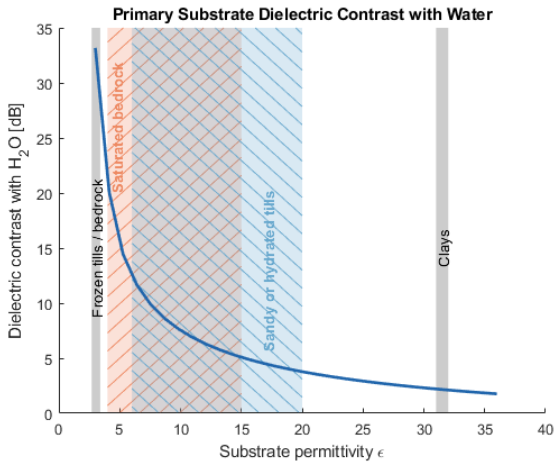


Figure 2.13: Dielectric contrast between liquid water ($\epsilon = 78$) and substrates with permittivity from $\epsilon = 2.7 - 36$. Example bed material permittivity ranges from [96] are provided as reference.

We also assumed constant radar attenuation in the ice. This assumption is reasonable given the short physical distances of our radar simulations. Simulations over greater distances may require introducing variation in the imaginary component of ϵ_{ice} to account for heterogeneous attenuation loss.

Several notable inconsistencies between our best simulations and the original THW2/ UBH0c/ X243a data remain. First, R_{rel} over the beginning and final $500m$ of all the simulations are about $\sim 5 - 8\,dB$ higher than the THW2/ UBH0c/ X243a RES data. This may indicate a change in σ_{bed} near the edges of the simulated region. The low-lying area in the region is a perfect topographical feature to accumulate sediments, which likely have low roughness. The steeper and elevated topography near the edges of the simulated region may be exposed bedrock, with greater roughness, which we have shown in our hypothetical case simulations can reduce R_{rel}. In future iterations of the simulator, we would enable heterogeneity in σ_{bed} in order to capture this type of variation explicitly.

R_{rel} near $2000m$ along track in all simulations was $\sim 10\,dB$ lower than actual reflectivity from THW2/ UBH0c/ X243a (Fig. 2.10). This is coincident with a steep topographical

feature in the THW2/ UBH0c/ X243a radargram. Steep slopes such as this likely represent a limitation of our simulation approach. The surface representation using $5m$ flat facets will inherently direct more reflected energy away from the antenna position than a real surface. Therefore, caution is imperative when interpreting results near steep topography.

There are several additional limitations of our simulation method for testing sub-glacial hypotheses. The simulation radius of $R = 300m$ explicitly limits the impact of range migration and clutter. A more complete simulation incorporating a larger R would be beneficial to simulations in thicker ice or focusing over longer apertures. Future work should combine additional computing power with simulated facet roughness [24] for additional realism and efficiency.

Our 3 dimensional model for topography was derived from a single along-track RES flight line, which enables high confidence and sufficient resolution for ice geometry at nadir. However, this has the obvious limitation of requiring a previous flight line to build our simulation. We lack similar observation density across-track, leaving low-resolution ($500m$) open-source DEMs (such as BedMachine V2 [56]) as our best option for approximating off-nadir features. This asymmetry is not problematic for replicating basic topography at nadir, but the lack of realistic off-nadir features reduces the sharpness of the focusing algorithm. We can see this effect by comparing the image quality in Fig. 2.8a to simulated results in Fig. 2.8b or Fig. 2.9a. This limitation also clearly reduces our ability to assess hypotheses involving any off-nadir targets.

It is also important to note that the simulation in Fig. 2.8d exhibits along-track R_{rel} variation $> 30\,dB$ without any change in dielectric properties at the bed. This demonstrates that significant changes in bed echo strength are possible due to topography alone. When inferring the presence of sub-glacial hydrological features from RES data, care must be taken to consider reflectivity within the context of bed topography, hydraulic potential, attenuation, and other factors which may influence the radar echo strength. This observation

also demonstrates the value of our simulation methodology for confirming the presence and extent of sub-glacial water.

Conclusions

In the exercise presented here, we optimized a radar simulation technique developed by [26] to study the theoretical RES response from sub-glacial systems. The simulator incorporates the Stratton-Chu integral and Linear Phase Approximation to efficiently estimate backscattered radar signal from simulated targets. Through a series of hypothetical simulation cases, we demonstrated the impact on relative reflectivity from rounded Röthlisberger channels or specular flat canals surrounded by bed materials of varying roughness. These simulations confirmed that reflectivity is highly dependent on both the size and cross-sectional shape of the sub-glacial water structure. Our results can be applied broadly to infer the presence, size, and structure of sub-glacial water bodies from RES surveys in a more robust and sophisticated way than previous methods.

In our example flight line THW2/ UBH0c/ X243a from Thwaites Glacier, we demonstrated the simulator's utility in testing relevant hypotheses in sub-glacial hydrology. A large water structure could produce the elevated reflectivity beneath Thwaites Glacier, in a region coinciding with a channel route proposed by [31]. Of the scenarios we tested, the radar signature was most consistent with canals averaging $> 30m$ and covering at least half the area for $600m$ along-track. Additional simulations including a broader range of hydrological structures and bed materials may be useful to conclusively characterize the feature. Further, although we do not see a Röthlisberger channel at this precise location, our findings do not preclude Röthlisberger channelization further upglacier. Simulations of new and existing RES survey data across the Thwaites catchment could characterize the extent of upglacier channelization.

The method we outline has broad applicability for studying the basal environment of

large glaciers. As we have shown, the simulation methodology can offer useful constraints when testing sub-glacial hypotheses. Scientific intuition, additional data inputs, and more computational power will improve the promise of this technique. Future work may include additional computational efficiency to enable more extensive simulations, as well as comprehensive investigations on the impact of substrate roughness, material properties, and additional water geometries.

RES data collection is logistically challenging and expensive. A forward model capable of predicting optimal locations for sub-glacial survey targets, instead of modeling existing flight lines, is an area of interest for future work. In such a forward model, computing resources must be optimized by strategically constraining parameter sets, and performing sensitivity tests for many of the variables considered here.

EXPLORING CANYONS BENEATH DEVON ICE CAP FOR SUB-GLACIAL DRAINAGE USING RADAR AND THERMODYNAMIC MODELING

Contribution of Authors and Co-Authors

Manuscript in following chapter

Author: Chris Pierce

Contributions: prepared the original draft, performed the design and execution of experiments and simulations, and participated in the field work to collect RES data from Devon Ice Cap.

Author: Mark Skidmore

Contributions: provided oversight and partial funding, as well as significant editorial contributions.

Author: Lucas Beem

Contributions: provided context for the project, made significant editorial contributions, and led the field team responsible for RES data collection over Devon Ice Cap.

Author: Don Blankenship

Contributions: provided leadership support, funding, and programmatic resources for the investigation and RES data collection over Devon Ice Cap.

Author: Ed Adams

Contributions: provided significant editorial support and contributed to experimental design.

Author: Christopher Gerekos

Contributions: contributed the original RES simulator software, and provided significant editorial support.

Manuscript Information

Chris Pierce, Mark Skidmore, Lucas Beem, Don Blankenship, Ed Adams, Christopher Gerekos

Journal of Glaciology

Status of Manuscript:
____ Prepared for submission to a peer-reviewed journal
____ Officially submitted to a peer-reviewed journal
_X_ Accepted by a peer-reviewed journal
____ Published in a peer-reviewed journal

Cambridge University Press
Submitted: January 2024
Accepted: June 2024

Abstract

Sub-glacial canyon features up to $580m$ deep between flat terraces were identified beneath Devon Ice Cap (DIC) during a 2023 radar echo sounding (RES) survey. The largest canyon connects a hypothesized brine network near the DIC summit with the marine-terminating Sverdrup outlet glacier. This canyon represents a probable drainage route for the hypothesized water system. Radar bed reflectivity is consistently $30\,dB$ lower along the canyon floor than on the terraces, contradicting the signature expected for sub-glacial water. We compare these data with backscattering simulations to demonstrate that the reflectivity pattern may be topographically induced. Our simulated results indicated a $10m$ wide canal-like water feature is unlikely along the canyon floor, but smaller features may be difficult to detect via RES. We calculated basal temperature profiles using a 2-D finite difference method and found the floor may be up to $18°C$ warmer than the terraces. However, temperatures remain below the pressure melting point, and there is limited evidence that the canyon floor supports a connected drainage system between the DIC summit and Sverdrup Glacier. The terrain beneath DIC demonstrates limitations for RES. Future studies should evaluate additional correction methods near complex terrain, such as RES simulation as we demonstrate here.

Introduction

The presence (or absence) of liquid water at the glacier bed is fundamental to a variety of sub-glacial processes. Distributed hydrological systems reduce basal friction, significantly altering ice internal stress and accelerating flow rates [2, 15, 39]. Sub-glacial channels can transport liquid water and thermal energy down glacier, enhancing grounding line retreat [17, 83, 107]. The sub-glacial water system can also sustain unique microbial communities, which may be responsible for enhanced biogeochemical erosion of the bedrock [70, 90]. Further,

these isolated habitats may provide rare terrestrial analogs for icy environments across the solar system with potential to support life [14, 70].

The ability to quickly image a large geographic area has made RES appealing for decades in the study of sub-glacial hydrology (e.g. [9, 30, 59, 80, 83, 89]). Observations of elevated basal relative reflectivity ($\geq 15\,dB$ over ambient) and high specularity content in RES data are commonly interpreted to indicate sub-glacial water [9, 83, 84, 107]. These metrics coupled with hydraulic potential modeling represent the conventional method for identifying sub-glacial hydrology with RES observations. Despite its broad appeal, spatial heterogeneity of ice properties and bed material creates significant uncertainties, complicating interpretation of bed reflectivity from RES data. Synthetic aperture processing of coherent radar helps focus the beam pattern, reducing off-nadir clutter and improving along-track resolution. In complex topography, however, significant ambiguity in locating the bed can persist [82]. Radar attenuation loss also varies with ice thickness, as well as temperature and impurity content of the ice. Common attenuation correction methods assume varying degrees of homogeneity in the ice and bed physical properties [53, 86], which are not always realistic. These ambiguities imply that while RES is a useful tool for characterizing sub-glacial hydrology, additional context such as geothermal heat flux, hydropotential modeling, and additional experimental methods (geophysical observations, direct access, and modelling) may strengthen or contradict RES interpretations (e.g. [44, 48, 58, 98]).

Until recently, basal temperatures beneath Devon Ice Cap (DIC), Devon Island in Nunavut, Canada supported the assumption of a frozen bed, largely devoid of an extensive hydrological system [78, 100]. A 2018 airborne radar echo sounding (RES) survey conducted by the University of Texas Institute for Geophysics (UTIG) identified several radar-bright, specular bed features within a hydraulically flat environment near the DIC summit. These features were interpreted as a system of sub-glacial lakes, and surrounding elevated radar reflectivity was interpreted as a distributed brine network (Fig. 3.1), which must be

hypersaline to exist at DIC basal temperatures of $-14°C$ or colder [78, 80].

The [78] sub-glacial lakes were inferred primarily from RES data. Subsequent transient electromagnetics (TEM) and sonar studies conducted in the area indicate that a present-day sub-glacial lake is unlikely [45], however no such counter-evidence exists for the brine network discussed in [80]. The original hypothesis envisioned a channelized network transporting brine from a distributed system near the DIC summit to the Sverdrup Glacier terminus. Similar transitions from distributed to channelized hydrology have been identified throughout the cryosphere in freshwater systems, although the mechanisms for their formation are poorly understood [21, 41, 83].

If confirmed, the brine network and associated channel network described in [78] and [80] represent a unique unexplored environment in the Earth's cryosphere. This opportunity motivated an additional airborne RES survey in Spring 2023, focused on the Sverdrup catchment (Fig. 3.1). In this article, we specifically consider the region between the DIC summit and two subaerial canyons confining the main tributaries of Sverdrup Glacier (Fig. 3.1). Hereafter, we will refer to this as the "transition zone", and the glacier flowing downstream from the transition zone as "Sverdrup Glacier". The transition zone is critical to establishing the existence of pathways between the hypothesized brine network and Sverdrup Glacier, and may help to further our understanding of how such hydrological transitions evolve.

A RES survey from the year 2000 and described in [18] mentions "steep-sided valleys" and "bedrock troughs" beneath the DIC. These features were qualitatively associated with accelerated ice flow, possibly due to thermodynamic conditions favoring basal melt [99]. Our RES survey conducted in Spring of 2023 details canyon features in the transition zone, consistent with the [18] description. We analyze one canyon reaching a depth of $580m$ as a possible drainage route for the hypothesized sub-glacial water system proposed by [80].

The investigation of any sub-glacial hydrology beneath the DIC transition zone

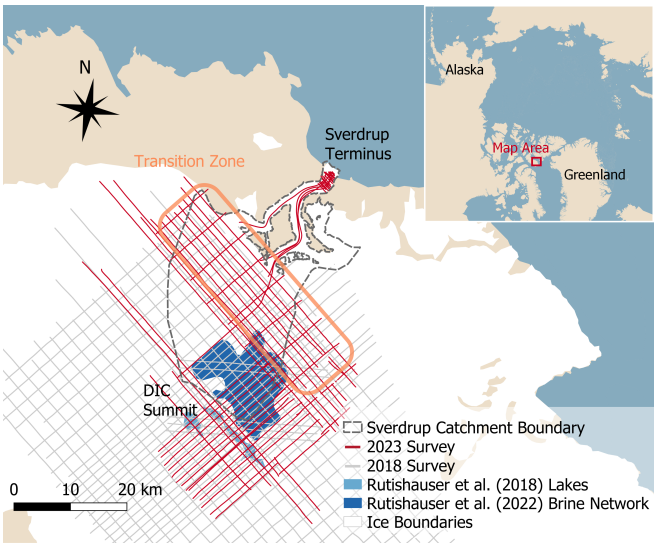


Figure 3.1: Map of airborne RES surveys using the UTIG MARFA instrument in 2018 (grey) and 2023 (red). Location of sub-glacial lakes (light blue) and brine network (dark blue) proposed by [78, 80] are near the summit of DIC.

must consider the influence of canyons on geothermal heat flux, which may affect basal temperatures and attenuate the radar signal. The potential for canyons to concentrate geothermal heat flux and drive local temperature anomalies has been discussed since the early 1900's [47]. [46] considered heat conduction near topographic features, such as canyons, concluding that heat flux can be amplified many times the regional average along canyon walls and floors. In the sub-glacial context, this process could create a region warm enough for liquid water to exist in an otherwise cold-bedded glacier. Lachenbruch's model was applied to canyons beneath Jakobshavn Isbræ in Greenland, where elevated geothermal flux was predicted to enhance basal melt rates [98]. More recently, [105] modeled 2-D englacial temperature profiles near deep valleys using a finite difference approximation of the heat equation. [105] used a spatially invariant heat flux boundary condition, and found a more muted topographic effect on basal temperatures than predicted by [46] or [98].

We cannot test the extant sub-glacial hydrology hypothesis beneath the DIC transition zone without considering the effects of canyon morphology on thermodynamics and radar

reflectivity. Here, models of both the englacial temperatures and radar reflectivity are applied to assist in the interpretation of radar data for identifying sub-glacial water. The results of the study show conditions are inconsistent with the existence of sub-glacial freshwater beneath the DIC transition zone. We cannot explicitly rule out hydraulic features less than 10m wide on the canyon floor, especially if they are saline as proposed in [78].

More generally, this work identifies improvements to thermodynamic model boundary conditions and inherent complications of interpreting radar reflectivity in steep sub-glacial terrain. The radar modeling results suggest that bed geometries can reduce basal returns by influencing attenuation and reflectivity interpretations. We suggest that regions with complicated terrain would benefit from explicitly including a bed terrain correction. These ambiguities, taken together, can confound the identification of sub-glacial water by RES observations.

Data and Methods

Radar Data and Methods

The 2023 DIC RES survey was conducted using UTIG's 60 MHz multifrequency airborne radar sounder with full-phase assessment (MARFA) instrument on an AS-350 B2 helicopter platform, as described in Lindzey et al. (2020). This platform enabled closer across-track spacing (tighter turning radius) and along-track resolution (15m, slower flight speed) near steep topography than the 2018 survey (22 m), which used a similar radar mounted on a DC-3 Basler airframe. Data were range compressed, corrected for geometric spreading loss and aircraft position, and focused in azimuth as described in [66].

Basal returns are identified in the radar data through manually determined brackets (one above and one below), encapsulating the identified basal reflector. The magnitude of the basal return P_r is taken as the sample with the maximum value between those bounds, at each vertical trace along-track.

We estimate local englacial attenuation using a regression model [40, 83, 86]. Bed returned power P_r in decibels (as denoted by $[\,]_{dB}$) is assumed to have a linear relationship with ice thickness d_{ice} after correcting for geometric spreading loss G (Eq. 3.1a). Geometric spreading is a function of aircraft height h, ice thickness d_{ice}, and ice refractive index η_{ice} (Eq. 3.1b) [32, 65]. Other parameters in Eq. 3.1a such as system gain S, birefringent losses B, and bed reflectivity R_{bed} are assumed to be relatively homogeneous within the subset of nearby radar observations. The resulting best-fit slope between ice thickness and geometrically corrected bed power is twice the mean one-way attenuation rate $\langle N_{ice} \rangle$ in $dB\,km^{-1}$.

$$[P_r]_{dB} + [G]_{dB} = [R_{bed}]_{dB} - 2\,d_{ice}\,\langle N_{ice} \rangle + [S]_{dB} + [B]_{dB} \tag{3.1a}$$

$$G = (4\pi)^{-3} \eta_{ice}^{-2}\,(h + d_{ice}/\eta_{ice})^{-4} \tag{3.1b}$$

If we consider the entire 2023 survey population using this model, we estimate $\langle N_{ice} \rangle = 17.5\,dB\,km^{-1}$ (Fig. 3.2). This attenuation rate is more than $4\,dB\,km^{-1}$ lower than the previous estimate from [80], which applied the same linear regression method to the 2018 UTIG RES survey data. Our value also aligns well with the mean attenuation rate of $17\,dB\,km^{-1}$ derived in [45] using the alternative Arrhenius method. However, the root-mean-squared error (RMSE) between corrected bed power ($[P_r]_{dB} + [G]_{dB}$) and the regression fit is $9.2\,dB$, indicating high uncertainty in the attenuation loss.

A geographically constrained footprint may minimize heterogeneity in bed and ice properties, improving the fit between Eq. 3.1a and the RES data [86]. For this study, we also re-calculated the attenuation regression model using only a subset of the data within $3km$ of the canyons identified in the transition zone (see Fig. 3.6). For this data subset, which we refer to as "near-canyon", our estimate of $\langle N_{ice} \rangle = 33.6\,dB\,km^{-1}$, with a RMSE of $10.7\,dB$ (Fig. 3.2). This alternative calculation is much higher than previous attenuation estimates

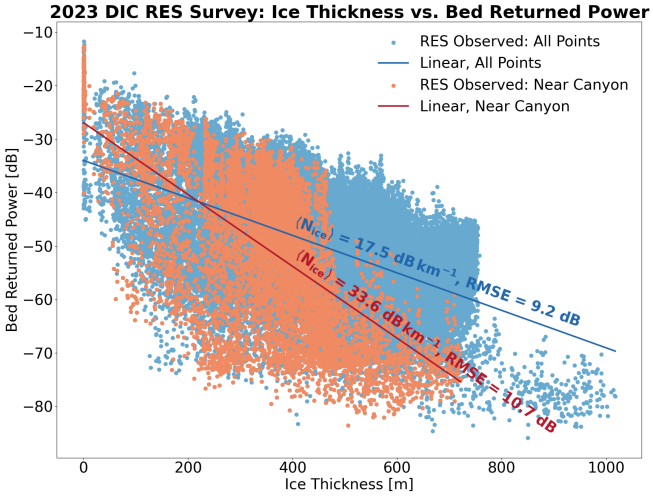


Figure 3.2: Attenuation rate determined by linear regression fit of ice thickness vs. bed returned power (corrected for geometric spreading). The full RES survey is shown in blue, while the "Near Canyon" data (orange/red) is the subset of points located within $3km$ of Canyons A and B from Figs. 3.6a and b.

and does not reduce uncertainty. Therefore, we use the original estimate of $17.5\,dB\,km^{-1}$ in all subsequent calculations unless otherwise noted.

RES Simulation Method

We used the RES simulator from [26], to create modeled radargrams with topography similar to canyons identified beneath the DIC. This method, applied to study sub-glacial hydrology as described in [67], enables us to quantify the theoretical RES response to changes in assumed bed conditions. The simulator ingests a digital elevation model (DEM) with resolution $l_f = 5m$, derived from the radar observations of bed and surface elevation along a flight line (Fig. 3.3a). Each facet within the bed and surface DEM are assigned dielectric constants ϵ for ice, rock, or water based on the location and hydrological feature we wish to model (Table 3.1).

The simulator estimates the returned power profile P_r for along-track location y_i by superimposing the returned power from many individual rays directed at the ice surface

Table 3.1: Summary of parameters as described in [67] used in RES simulations of *DEV3_PER0a_Y86a*.

Parameter	**MARFA Value**
Aircraft height (h)	$500\,m$
Aircraft velocity (v_a)	$30\ m/s$
Facet length (l_f)	$5\ m$
Simulation Radius (R)	$300\,m$
Correlation length (l_c)	$15\,m$
Surface roughness (σ_{ice})	$0.2\,m$
Basal roughness (σ_{bed})	$0.2, 1\,m$
Channel width (c_w)	$0, 10\,m$
Center frequency (f_c)	60 MHz
Bandwidth (B_w)	15 MHz
PRF[a]	6400 Hz *(30 Hz)*
Sampling frequency (f_s)	50 MHz
Pulse length (Υ)	$1\ \mu s$
Receiving window (T_r)	$50\ \mu s$
Ice Permittivity (ϵ_{ice}) [b]	$3.18\,(1 + .0018i)$
Bed Permittivity (ϵ_{rock}) [c]	5
Water Permittivity (ϵ_{H_2O}) [d]	78

[a] Native PRF for MARFA radar is $6400Hz$. Simulations are run at $30Hz$ to replicate effective PRF after coherent summation during data processing.

[b] [22, 65, 95]

[c] We chose a value near the low end of the range reported for saturated bedrock [95] to maximize contrast between rock and ice.

[d] A value between seawater and freshwater, as reported in [65] was used.

within a simulation radius R. The energy's path and field strength are traced through the ice surface, then reflected from the bed (Fig. 3.3b). By compiling the data for each discrete location y_i along a flight path, we build a simulated radargram to approximate returned power from the topographic and material model applied. Comparable to the actual radar data, simulation outputs are range compressed and focused [67].

Attenuation loss rate is controlled in the model through the complex ice dielectric constant, $\epsilon_{ice} = \epsilon'_{ice}(1 + i \tan\delta)$. The loss tangent ($\tan\delta$) is related to attenuation rate via Eq. 3.2, where $\lambda = 5m$ is the radar center wavelength, and $\eta_{ice} = \sqrt{\epsilon'_{ice}}$ is the ice refractive index. We chose $\epsilon_{ice} = 3.18(1 + .0018i)$, where $\tan\delta$ was selected to emulate the calculated 1-way attenuation rate $\langle N_{ice}\rangle - 17.5\, dB\, km^{-1}$, and ϵ'_{ice} is well documented in the literature [22, 65]. As with the real RES data, we can convert between raw power P_r and R_{bed} using Eq. 3.1a. Unlike the real RES data, $\langle N_{ice}\rangle$ was explicitly defined through the loss tangent, meaning there is no uncertainty in modeled attenuation loss.

$$\langle N_{ice}\rangle = \frac{20\pi\eta_{ice}\log_{10} e}{\lambda}\tan\delta \tag{3.2}$$

We modeled two scenarios near the intersection of Canyon B and *DEV3_PER0a_Y86a*, as outlined below.

1. **Frozen bed**: all bed DEM facets have dielectric constant ϵ_{rock}.
2. **10m canal**: a strip of facets $10m$ wide has dielectric constant ϵ_{H_2O}. All other facets have dielectric constant ϵ_{rock}, as in the *frozen bed* simulation.

There are a wide range of alternative possible water structures at the Canyon B floor, including Röthlisberger channels, Nye channels, or saturated tills. We have chosen a continuous, flat canal because its geometric profile and dielectric contrast with the surrounding bed material will produce the greatest reflectivity response. We speculate that

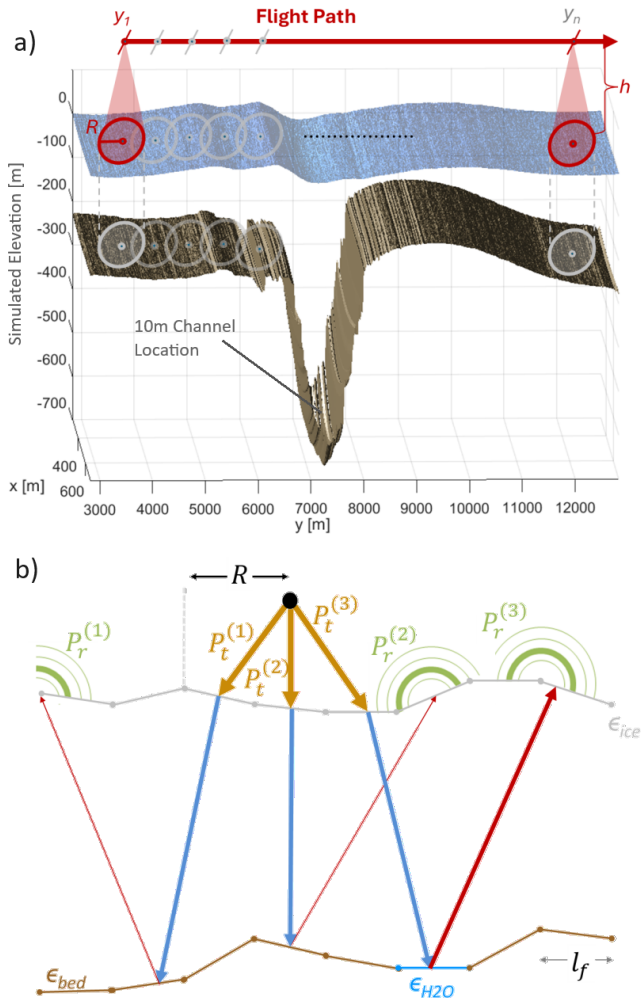


Figure 3.3: a) 3-D view of RES simulation DEM and flight path over canyon topography at *DEV3_PER0a_Y86a* (label "B" in Figs. 3.6a, b). Note that simulation increments y_i along the flight path are not drawn to scale. Actual simulated increments in y are $v_a/PRF = 1m$ (Table 3.1) b) Cartoon of ray tracing in a 2-D cross-section of a simulation. Given our simulation radius $R = 300m$ and $l_f = 5m$, returned power is estimated by tracing over 10^4 rays at each position increment y_i.

any continuous channels through the transition zone are likely to have a footprint smaller than $10m$, due to the limited hypothesized source of liquid water draining from the DIC summit, and minimal basal melt from the generally frozen bed. [67] also demonstrated that the reflectivity response curve for a simulated flat canal is asymptotic above $10 - 20m$. Therefore, our simulation scenarios represent end-members on the continuum of possible hydrologic structures. Simulation results will diagnose the radar's overall sensitivity to water within this topographic environment, but may not conclusively determine the precise water structure without further modeling.

In both simulations, we superimpose random isotropic Gaussian roughness on the bed DEM, with $\sigma_{bed} = 0.2m$ or $0.35m$ over a correlation length of $15m$. In part, this is added to reduce the potential for simulation artifacts such as Bragg resonance [25]. This is also done to provide an approximation of divergent radar energy scattering due to basal roughness. A more detailed discussion of basal roughness, including rationale for the choices of σ_{bed} and l_c are found in *Appendix C*.

Because the modeled attenuation is known, variation in R_{bed} must result from changes in topography or bed material. Therefore, comparing simulated results to actual RES data helps to constrain the possible sub-glacial environmental conditions that may produce a given along-track reflectivity profile. It represents an alternative, and perhaps more selective approach to simply equating sub-glacial water with high values of R_{bed}.

All other relevant parameters used in the RES simulation setup are tabulated in Table 3.1. These values were chosen to mimic the geometry and radiometric properties of a helicopter-based UTIG MARFA radar experiment.

2-D Thermodynamic Modeling Method

We take a 2-D modeling approach similar to [105] in order to estimate thermodynamic conditions at the bottom of the canyon features beneath the transition zone. However, our

approach explores two alternative basal heat flux boundary conditions near the $580m$ canyon beneath DIC. The model constrains the likely basal thermal regime, which we consider in conjunction with the RES evidence to evaluate the possibility of a present-day drainage network in the Sverdrup transition zone.

We assume the englacial temperature (T) is described by the steady-state heat equation with advection as presented in [63] (Eq. 3.3a). The form of Eq. 3.3a assumes the ice has constant thermal diffusivity k, defined as the ratio between thermal conductivity K and the product of specific heat capacity c_p and density ρ (3.3b). Thermal advection occurs due to ice motion with ice velocity vector $\bar{\mathbf{w}}$.

$$k\nabla^2 T - \bar{\mathbf{w}} \cdot \nabla T = 0 \tag{3.3a}$$

$$k = \frac{K}{\rho\, c_p} \tag{3.3b}$$

As in [105], we create a simplified 2-D model representing the topographic cross-section desired. The ice surface and bed geometry are approximated with a series of plane slopes, as shown in Fig. 3.4 for a canyon feature identified in survey flight *DEV3_PER0a_Y86a*. The simplified canyon has depth d, bottom width c_b, nominal terrace ice thickness h, and canyon walls sloped at angle θ. Figure 3.4 superimposes bed and surface elevation profiles derived from radar transect *DEV3_PER0a_Y86a* to demonstrate the similarity between actual canyon topography and a modeled geometry with $d = 530m$, $h = 170m$, $\theta = 45°$, and $c_b = 380m$.

The idealized surface and bed geometry is discretized into a 2-D matrix with resolution $\Delta x = \Delta z = 10m$. Equation 3.4a is the central finite difference approximation for Eq. 3.3a, where i and j are indices in the horizontal (x) and vertical (z) directions. Each pixel above the canyon is assigned ice thermal diffusivity k from Table 3.2. Vertical velocity is

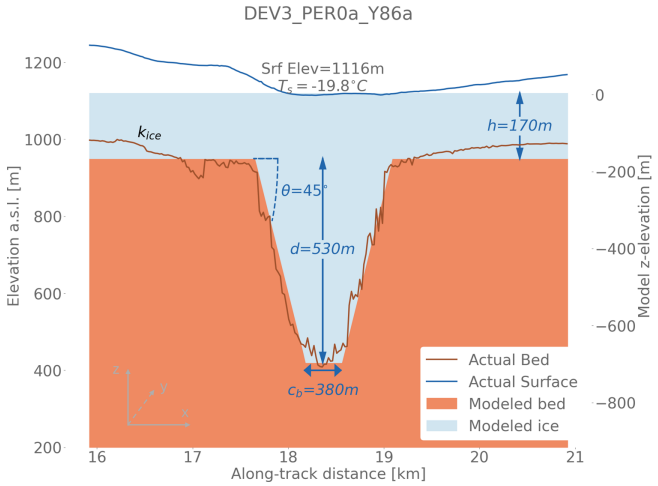


Figure 3.4: Representative model geometry is superimposed over actual canyon cross-section derived from radar bed and surface picks for *DEV3_PER0a_Y86a* (label "*B*" in Figs. 3.6a, b). Similar figures demonstrating modeled and actual canyon topography at all modeled radar transects are found in *Appendix B.*

described by 3.4b above the ice/rock boundary. The annual ice accumulation rate, $\beta = 0.17 \pm 0.05 m\, yr^{-1}$ was based on the 1963-2000 mass balance performed in [50] across four shallow core sites within the upper Sverdrup catchment. In order to confine the model domain to two dimensions, we assume advection only in the z direction and neglect ice motion in x and y [63].

$$T_{i,j} = \frac{1}{4}\left[T_{i-1,j} + T_{i+1,j} + T_{i,j-1}\left(1 + \frac{w_z \Delta x}{2k}\right) + T_{i,j+1}\left(1 - \frac{w_z \Delta x}{2k}\right)\right] \tag{3.4a}$$

$$w_z = -\beta z_{i,j}/h \tag{3.4b}$$

The 2-D thermodynamic model iteratively solves Eq. 3.4a. The model converges at

iteration m, when the criterion in Eq. 3.5 is met.

$$\sum_i \sum_j \left(T_{i,j}^m - T_{i,j}^{m-1}\right)^2 \leq 0.001 \tag{3.5}$$

The boundary conditions for the model domain are:

1. Constant ice surface temperature T_s. We assume $T_s = -23°C$ at the DIC summit ($1900m$), and increases $4.4°C$ per km of elevation loss [23, 78].

2. No horizontal heat flux at the left and right side of the domain ($dT/dx = 0$).

3. One of the following basal heat flux boundary conditions:

   (a) **Constant:** Vertical heat flux applied the ice/bedrock interface is spatially constant and equal to the regional average geothermal heat flux, $Q_z(x) = 65\,mW\,m^{-1}\,K^{-1}$ [78].

   (b) **Lachenbruch:** $Q_z(x) = q_{an}(x) \cdot 65\,mW\,m^{-1}\,K^{-1}$ varies along the the x direction at the ice/bedrock interface as defined in [46]. The solution for $q_{an}(x)$ is tabulated in [46] for $\theta = 15 - 90°$.

Fig. 3.5 compares the basal heat flux boundary conditions *3a* and *3b* for the simulated geometry in Fig. 3.4. The Lachenbruch boundary condition predicts large variations in heat flux between the canyon walls, and is most applicable if the thermal diffusivity contrast at the interface is high. As thermal diffusivity contrast between bedrock and ice approaches zero, basal heat flux will approach the Constant boundary condition. Therefore, although we cannot know the precise variation in basal heat flux $Q_z(x)$ along the canyon, comparing temperature profiles using both boundary condition *3a* and *3b* provides a useful constraint on temperature uncertainty due to the topography beneath DIC.

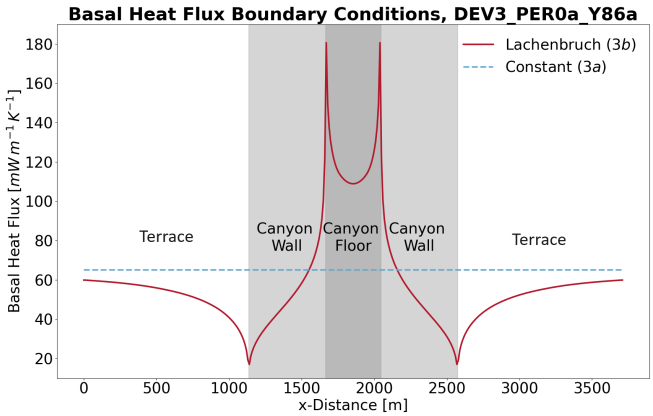


Figure 3.5: Geothermal heat flux boundary conditions for *DEV3_PER0a_Y86a*. The Lachenbruch boundary condition exhibits large variations in heat flux along the x direction, which is dependent upon the canyon geometry.

For all simulations, we did not incorporate latent heat into the thermodynamic model. Therefore, similar to [105], any resulting temperatures in excess of the ice pressure melting point represent melt potential, and a likely presence of liquid water. We also neglect any frictional heating in this model. We expect basal drag to be negligible across most of the DIC transition zone, with the possible exception of the location nearest Sverdrup Glacier at *DEV3_PER0a_Y87a* [100].

Results

RES Results

The 2023 survey included 10 transects running approximately perpendicular to ice flow across the transition zone (Fig. 3.6a and b). The flight closest to Sverdrup Glacier (*DEV_PER0a_Y88a*) was characterized by locations of thin ice ($< 100m$) with significant clutter from nearby canyon walls, and consequently is excluded from our analysis. The remaining 9 flights each demonstrate broad areas of elevated bed reflectivity between narrow regions with dim R_{bed} (Fig. 3.6a). The pattern in specularity content (Fig. 3.6b) co-varies

Table 3.2: Summary of parameters used in 2-D heat transfer model.

Parameter	**Value**	**Description**
k	$1.1\,mm^2\,s^{-1}$	Ice thermal diffusivity [a]
Δx	$10\ m$	x resolution
Δz	$10\ m$	z resolution
β	$0.17 \pm .05\,m\,yr^{-1}$	Ice accumulation rate [b]
Q	$65\ mW\,m^{-1}\,K^{-1}$	Geothermal heat flux [c]

[a][63]
[b][50]
[c][78]

with relative bed reflectivity.

The 1-D focused radargram for one of these flights, *DEV3_PER0a_Y86a*, shows the existence of at least two narrow canyons lying between broad, flat terraces under the DIC (Fig. 3.6c). The canyons are labeled A and B in Fig. 3.6, and have estimated depths of $370m$ and $530m$ along the *DEV3_PER0a_Y86a* flight path, respectively. A and B are located directly up-glacier from Sverdrup's main tributaries (Fig. 3.6a and b).

The *DEV3_PER0a_Y86a* topographic lows at A and B are strongly correlated with minima in both R_{bed} and specularity content (Fig. 3.6c and d). The contrast in R_{bed} between the terraces and the canyon floor is $30 - 35\,dB$. Each of the parallel survey flights across the transition zone exhibit a similar relationship between topography, reflectivity, and specularity content (see *Appendix A*). Figures 3.6a and b plot the adjacent topographic lows for each flight line, and Canyon B's path can be traced from the [80] hypothesized brine network location to Sverdrup Glacier. Near the proposed brine network, Canyon B has a depth of $\sim 100m$, while ice $410m$ thick covers the terraces. As you follow Canyon B toward the Sverdrup Glacier, radar shows the ice thinning to around $100m$, while the canyon deepens

to $580m$ (Table 3.3).

If any sub-glacial water exists, it would follow the hydraulic potential gradient from the brine network to Sverdrup Glacier [80]. Sub-glacial hydraulic potential (ψ) is defined in Eq. 3.6 as a function of surface elevation z_s and ice thickness d_{ice}, where ρ_{ice} and ρ_{H_2O} are density of ice and water, respectively. In the transition zone the surface topography is relatively smooth, sloping toward Sverdrup Glacier. By contrast, the steep canyon topography results in large ice thickness changes. Therefore the canyons exert strong control on the local hydraulic potential, which will drive any water toward the canyon floor. The hydropotential analysis in [80] corroborates a likely drainage pathway from the hypothesized brine network to Sverdrup Glacier corresponding to Canyon B's location.

$$\psi = d_{ice}\left(\frac{\rho_{ice}}{\rho_{H_2O}} - 1\right) + z_s \tag{3.6}$$

Elevated bed reflectivity ($\geq 15\,dB$ above surroundings) and/or specularity content in RES data is frequently correlated with sub-glacial water [65, 83, 84, 107]. However, the area beneath the DIC transition zone demonstrates the opposite radiometric signature. If there was subglacial water flowing out of the hypothesized brine-network, the canyons are the most likely locations for subglacial water, yet, they exhibit the lowest reflectivity and specularity content.

Specularity content attempts to quantify the diffuse or specular quality of radar reflections from a target by comparing returned power over two different apertures [84]. A surface oriented normal to the radar signal's travel path with low roughness compared to the radar wavelength will exhibit high specularity content. The surface of a sub-glacial lake often meets this description. However, in the DIC transition zone topography, the terrace features are broad and relatively flat over our processing aperture lengths ($700m$ and $2km$). By contrast, the width of Canyon B from brink to brink is less than $2km$, with large

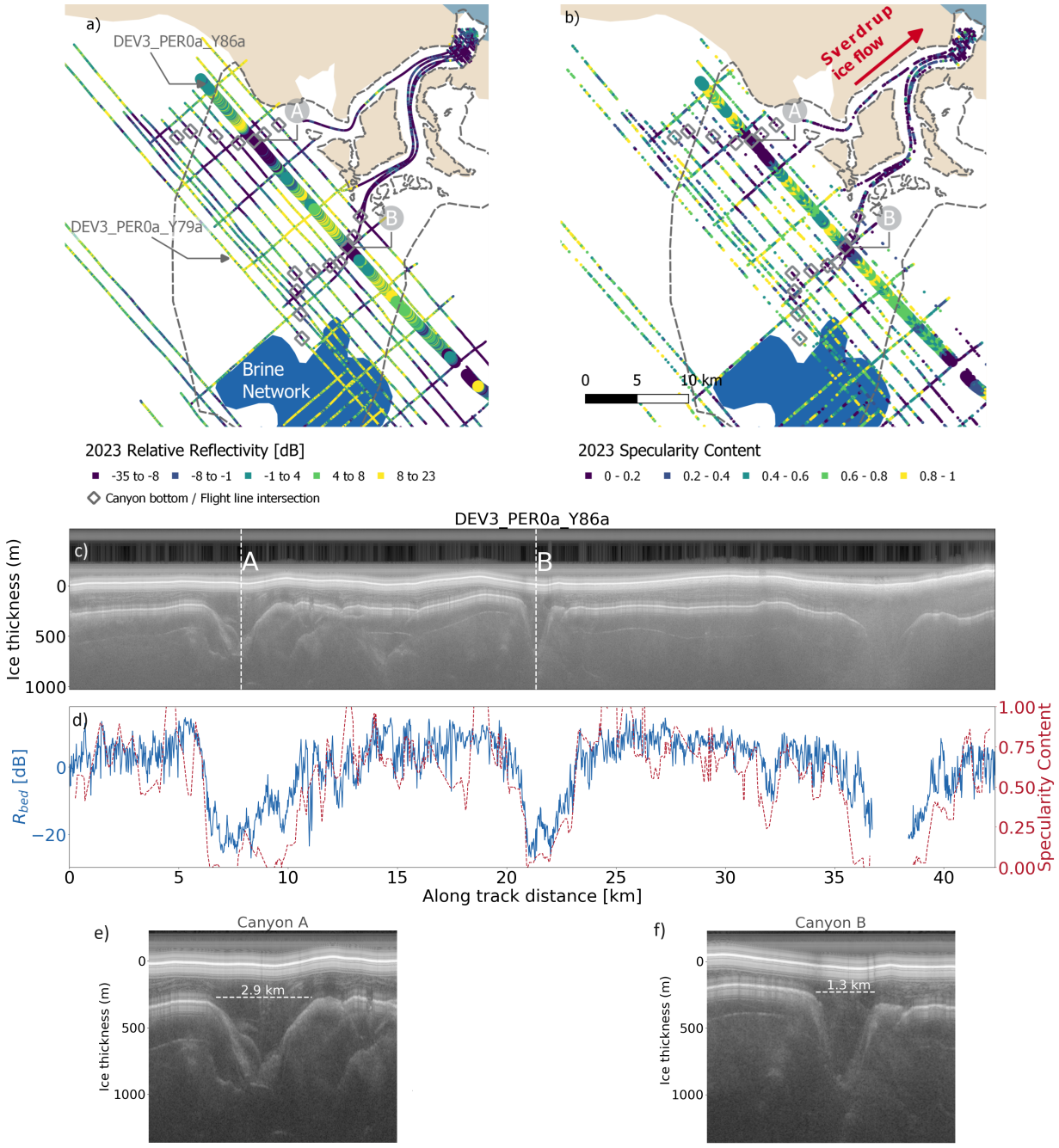


Figure 3.6: a) Relative reflectivity and b) specularity content from the 2023 RES survey in the transition zone between the DIC summit and Sverdrup Glacier. The locations of *A* and *B* on *DEV3_PER0a_Y86a* are shown. The grey diamonds trace Canyon *A*'s location from the hypothesized brine network to Sverdrup Glacier. c) 1-D focused radargram for *DEV3_PER0a_Y86a*. Points *A* and *B* are the canyon features mapped on panels *a* and *b* above. d) Relative reflectivity and specularity content for *DEV3_PER0a_Y86a*. e) and f) zoomed in images of Canyons *A* and *B* from the radargram in c).

topographic variation in between. Therefore, we expect higher specularity content on the terraces than in the canyons, even if sub-glacial water is present.

The strong positive connection between bed reflectivity and topography has implications to the interpretation of sub-glacial water within the transition zone topography. Conventional RES analysis might altogether exclude the Canyon B floor from consideration as having existing hydrology. However, we observe a $10\,dB$ local reflectivity peak coincident with the Canyon B floor (Fig. 3.6d). This could be a reasonable increase for a canal-like structure in the canyon. Within the context of a $> 30\,dB$ reduction in bed reflectivity across Canyon B such a radiometric signature will appear dim. Therefore, we consider the RES simulation results for interpreting the along-track R_{bed} profile and assessing the potential sensitivity of radiometrics to liquid water in this sub-glacial environment.

RES Simulations of Canyon B Topography

The simulated data in Fig. 3.7 indicate bed reflectivity reductions up to $30\,dB$ from the terraces to Canyon B's floor in each scenario, irrespective of the roughness value σ_{bed}. The pattern mimics the trend in the actual RES data for *DEV3_PER0a_Y86a* in the vicinity of Canyon B. Both simulations exhibit a small local peak in R_{bed} at the Canyon B floor. In the frozen bed scenario, this peak is $10\,dB$ above the minimum R_{bed} value (Fig. 3.7d). The results are virtually indistinguishable when σ_{bed} increases from $0.2m$ to $0.35m$.

The presence of a $10m$ canal increases the magnitude of this small peak at the Canyon B floor to $16.2\,dB$ when $\sigma_{bed} = 0.2m$ (Fig. 3.7c). The peak increases to $20.5\,dB$ when roughness increases to $\sigma_{bed} = 0.35m$. This indicates a $6.2 - 10.5\,dB$ response resulting from the canal vs. the frozen bed. Similar simulations from [67] of a $10m$ canal in flat topography resulted in a $14 - 20\,dB$ response, suggesting that the canyon topography attenuates the reflectivity response. The power returned from the canal also remains at least $10 - 15\,dB$ below bed reflectivity along the terraces. This result implies sub-glacial water in the canyon,

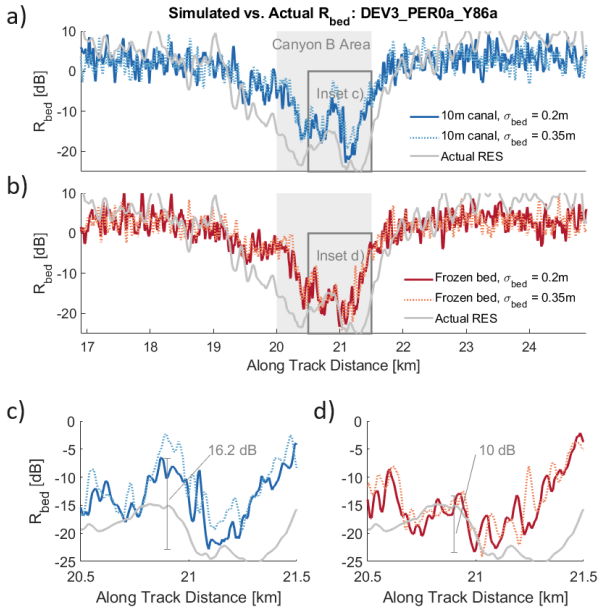


Figure 3.7: Simulated relative bed reflectivity results along an $8km$ segment of *DEV3_PER0a_Y86a*, centered on Canyon B, a) with a $10m$ flat canal at the floor and b) with a frozen bed and no canal. c) and d) zoomed view of R_{bed} response near the bottom of Canyon B.

even a specular canal of appreciable size, would appear dim on a radargram. Thus, the radar signature of such a canal could be easily overlooked in RES interpretation.

The magnitude of the reflectivity peak at the bottom of Canyon B closely matches the frozen bed simulation (Fig. 3.7d). Our simulations also demonstrate that RES has low sensitivity to liquid water in this environment. The simulation scenarios represent the end members for a spectrum of possible hydrological structures in this location. RES is unlikely to determine the presence of alternative structures with lower reflectivity signatures such as Röthlisberger channels, Nye channels, or hydrated tills [67]. Therefore, the simulation results imply the RES data is inconclusive regarding the presence of liquid water. We move on to consider local thermodynamic conditions at the Canyon B floor, to assess the potential for the presence of water, and thus the potential for such alternative water bodies.

2-D Thermodynamic Model Results

Fig. 3.8 shows modeled bed temperatures along the $14km$ path of Canyon B, using the parameters in Table 3.3. The Canyon B floor temperature increases from $-10.0 \pm 1.0°C$ near the brine network to $-3.0 \pm 1.0°C$ closest to Sverdrup Glacier, assuming constant basal heat flux. Canyon B floor temperatures are $1.3 - 4.5°C$ higher when the Lachenbruch heat flux boundary condition is applied, reaching a maximum of $1.4 \pm 1.1°C$ near Sverdrup Glacier. Along the terraces, ice thins over the same path, corresponding to a decrease in bed temperatures from $-12.6°C$ to $-16.9°C$ Bed temperatures along the terrace are in strong agreement for both heat flux boundary conditions.

We have not included latent heat into our model, therefore any temperatures above the ice pressure melting point indicate freshwater melt potential (Fig. 3.8b). Saline hydrology could exist at lower temperatures, with freezing point depression dependent on salt concentration [1, 80].

Discussion

Existence of Liquid Hydrology

Our 2-D thermodynamic model results indicate a continuous, saline drainage network is thermodynamically possible in the Sverdrup transition zone. Temperatures between $-7.7°C$ and $-11.3°C$ closest to the hypothesized brine network would sustain liquid at salinity lower than previously proposed in [80]. However, the findings from [45] indicate a nearby present-day sub-glacial lake [78] is unlikely. By extension, it is not unreasonable to question the existence of the brine network proposed in [80]. Combined with the radar evidence presented in this paper, brine drainage channels of sufficient size for RES detection are improbable in the DIC transition zone.

The temperature modeling does demonstrate significant temperature deviations of $2 -$

Table 3.3: Model parameters used for each intersection between survey flight line and Canyon *B*.

Survey line	**dist(m)**[a]	**Elev.(m)**[b]	$\mathbf{T_s}(^\circ\mathbf{C})$	**d(m)**	**h(m)**	$\mathbf{c_b}$**(m)**	$\theta(^\circ)$
DEV3_PER0a_Y79a	1.4	1153	-21.8	100	410	100	30
DEV3_PER0a_Y80a	3.7	1483	-21.5	150	390	100	30
DEV3_PER0a_Y81a	5.4	1407	-21.1	220	360	150	30
DEV3_PER0a_Y82a	7.6	1360	-20.9	185	390	850	15
DEV3_PER0a_Y83a	9.4	1313	-20.7	295	340	300	45
DEV3_PER0a_Y84a	11.0	1246	-20.4	425	280	250	45
DEV3_PER0a_Y85a	12.2	1198	-20.2	415	280	150	45
DEV3_PER0a_Y86a[c]	13.8	1116	-19.8	530	170	380	45
DEV3_PER0a_Y87a	15.1	1038	-19.5	580	100	280	45

[a]distance measured from nearest edge of proposed brine network depicted in Fig. 3.6 along Canyon *B* path
[b]Ice surface elevation at location where survey line intersects Canyon *B*.
[c]Example survey line referenced in all figures

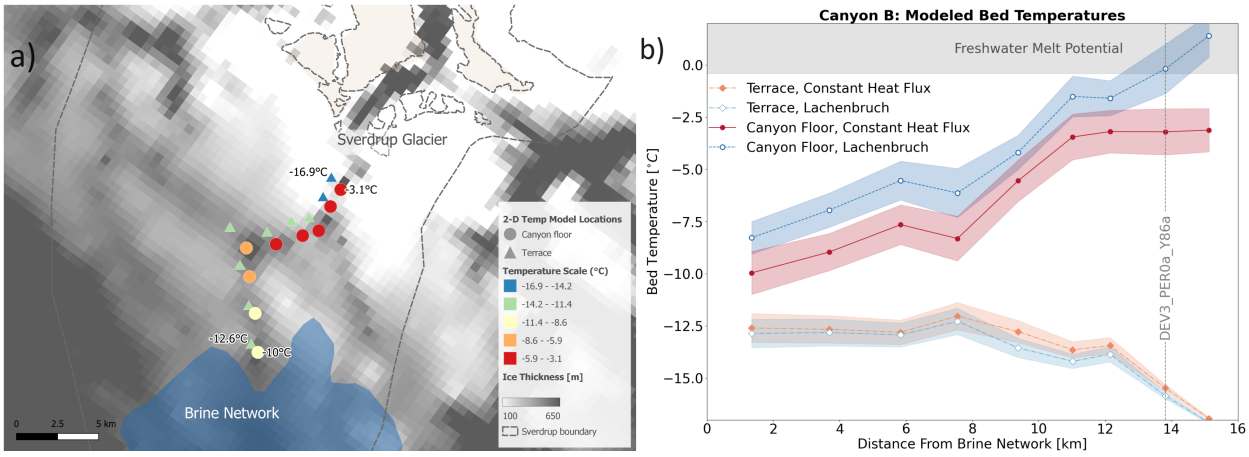


Figure 3.8: a) Modeled 2-D bed temperature profile locations in the Sverdrup transition zone. Colors indicate temperature of the Canyon B floor and terraces (constant boundary condition). The grayscale indicates ice thickness, derived from ArcticDEM [69] and bed elevation data provided in [78]. Location of [80] hypothesized brine network is shown in blue. b) Comparison of modeled bed temperatures for the Constant and Lachenbruch boundary conditions along Canyon B. The points represent the positions where the flight lines intersect Canyon B and bed temperatures were modeled. Shaded areas represent the modeled temperature range due to uncertainty in accumulation rate β.

$18°C$ between the floor and terraces along Canyon B. Although modeled basal temperatures are elevated throughout the canyon, temperatures do not exceed the ice pressure melting point along most of the path, precluding a freshwater network. At approximately $14km$ from the proposed brine network, near *DEV3_PER0a_Y86a*, the pressure melting point could be reached if the Lachenbruch boundary condition is assumed, but remain $3°C$ below freezing if the heat flux is constant.

The temperature models are generally consistent with the RES data and simulation results. The bed reflectivity patterns observed in the survey flights we examined imply either a frozen Canyon B floor, or one that contains small, disconnected liquid water features. We have also demonstrated through both simulated and real RES data that returned energy is reduced by up to $30\,dB$ in the canyons. This low returned energy in the canyon appears to reduce the radar's sensitivity to liquid water in our simulations, making small-scale

hydrological features challenging to interpret. It is important to note, however, that we simulated a $10m$ channel in a simulation environment with a $5m$ resolution. There is some risk a feature spanning only two facets in the backscattering model will be less prominent than in reality.

Thermodynamic Modelling and Sub-Glacial Hydrology

Both boundary conditions in our 2-D thermodynamic model produced generally congruent results for bed temperatures along the Canyon B terraces and floor. The difference in mean terrace temperature between the two boundary conditions was less than $0.5°C$ along the entire canyon length. At the canyon floor, both boundary conditions demonstrate a similar trend, although the Lachenbruch boundary condition predicts warmer temperatures due to the large variation in heat flux along the topography (Fig. 3.5).

In previous work, the [46] heat flux anomaly has been used as evidence for elevated bed temperatures within sub-glacial canyon features [98]. Lachenbruch provides a solution for heat flux along a simplified 2-D topographic surface, assuming the domain is bounded in the z direction at that surface. The derivation does not consider thermal contact with another material above the topographic surface, such as ice, which may insulate or enhance energy conduction. The Lachenbruch boundary condition may be a reasonable approximation when thermal diffusivity contrast at the interface is large and positive. This is true in the case of sub-aerial topography ($k_{air} \gtrapprox 10\, k_{rock}$). However, the bedrock underlying the transition zone is likely comprised of layered gneiss, sandstone, and limestone [62]. These materials have a mean thermal diffusivity of $1.1 mm^2\, s^{-1}$ [87, 93, 103], matching the value for ice in Table 3.2. Although no other study has thoroughly evaluated sub-glacial heat flux near topography, we expect the Lachenbruch boundary condition overestimates heat flux because it ignores the overlying ice. Therefore, we contend the constant heat flux case represents basal temperatures more accurately along Canyon B.

Our 2-D thermodynamic model also ignores advective heat transfer in both the x (left to right) and y (into the page) directions (see Fig. 3.4). This allowed us to simplify Eq. 3.3a for a 2-D use case which considers only the topographic cross-section. Ignoring advection in the x direction is almost certainly reasonable. The coordinate system is approximately oriented with ice flow along the y-axis, indicating ice velocity and temperature gradients in the x direction are much lower than in y or z.

Ignoring advection in the y direction may be less straightforward. Assumed surface temperature gradients along Canyon B's length are two orders of magnitude lower than the largest vertical temperature gradients calculated in our 2-D thermodynamic models ($\sim 10^{-4}$ vs. $\sim 10^{-2}\,^{\circ}C\,m^{-1}$). Conversely, maximum local ice surface velocity of $20-40\,m\,yr^{-1}$ is two orders of magnitude higher than the accumulation rate used in our model [100]. Therefore, the advection term from Eq. 3.3a ($\bar{\mathbf{w}} \cdot \nabla T$) in a 3-dimensional model could be of similar magnitude along the y and z axes. For our scenario along Canyon B, this implies our 2-D solution likely predicts marginally higher temperatures than an equivalent 3-D model. This reinforces our primary conclusion that connected drainage is unlikely beneath Canyon B unless it is saline. More broadly, attempts to replicate the thermodynamic modeling in this paper should carefully consider the validity of a 2-D vs. 3-D model, especially in regions of fast-flowing ice where frictional heating and lateral advection may be relevant.

Impact of Topography on RES Interpretation

The canyons beneath DIC's relatively thin ice demonstrate significant potential limitations for conventional RES analysis techniques. First and foremost, we have demonstrated that topography can produce significant variations in along-track relative bed reflectivity. Elevated basal reflectivity $> 15\,dB$ is a common criterion used to infer sub-glacial water from RES results [65, 78, 107]. Our interpretation of the 2023 DIC RES survey data demonstrates that more nuance is necessary. Conventional RES analysis would exclude

the canyons altogether due to their dim reflections, while the terraces might be considered as potential locations for sub-glacial water due to their elevated R_{bed} of $30\,dB$ or more. However, the terraces are the least likely location for sub-glacial water in this environment due to local hydropotential gradients. RES simulations may be a useful tool in combination with conventional techniques for resolving the likely structure, extent, and shape of sub-glacial water. This is especially true near topographic features where high variation in apparent basal reflectivity is expected.

We estimated the attenuation rate of $17.5\,dB\,km^{-1}$ using a linear regression fit of ice thickness vs. geometrically corrected bed returned power ($[P_r]_{dB} + [G]_{dB}$ from Eq. 3.1a). Figure 3.2 shows this regression model in blue. Our attenuation estimate is $4.3\,dB\,km^{-1}$ lower than the rate of $21.8\,dB\,km^{-1}$ in [80]. [45] indicated that the high attenuation rate in [78], which was derived using the same linear regression technique, may have contributed to mis-identifying sub-glacial lakes near the DIC summit. They suggest the Arrhenius method [53] may be more reliable for evaluating englacial attenuation rates, and estimated average attenuation over DIC $\sim 17\,dB\,km^{-1}$ [45].

Although our attenuation estimate is similar to the average value in [45], our depth-averaged temperatures along the terraces from our 2-D models ranged between $-17°C$ to $-18°C$. This is colder than the ice near DIC's summit, and would translate to an expected attenuation rate for pure ice around $\sim 14dB\,km^{-1}$ using an Arrhenius method [53]. Therefore, it is possible we have still overestimated attenuation rate in this study. Further, attenuation uncertainty exceeded $9\,dB$ across the 2023 survey.

In Fig. 3.2 we also re-calculate a "near-canyon" regression using a subset of the data within $3km$ of the Canyon A and B locations shown in Figs. 3.6a and b. In this data subset, the apparent 1-way attenuation rate nearly doubles to $33.6\,dB\,km^{-1}$. Both the full RES survey and near-canyon subset exhibit similar mean bed returned power where ice thickness is less than $450m$. However, mean returned bed power in the near-canyon data is $12\,dB$

less than the full RES survey for ice $> 450m$. In the near-canyon data, ice exceeding $450m$ is only found between the canyon walls, while thinner ice ($< 450m$) is generally on the adjacent terraces. This is a significant contrast with the full RES data set, which includes locations near the DIC summit where thicker ice covers topography with smaller magnitude slopes. This bias toward low returned power near the canyons inherently affects attenuation rates when derived via linear regression. The resulting regression fit may overestimate the survey-wide attenuation rate and increase uncertainty. This can result in overestimated bed reflectivity and misinterpretation of RES data [45].

The linear regression method in Equation 3.1a assumes relative homogeneity in ice material properties and bed reflectivity (Eq. 3.1a) to estimate attenuation. Ice material properties, including attenuation rate, are known to increase with temperature [53]. As we have shown through modeling, the canyon ice is likely much warmer compared to other locations beneath DIC. However, our RES simulations demonstrated a similar reduction in bed returned power despite bed reflectivity and attenuation rate values that were known and constant. This leads us to the conclusion that heterogeneity in ice temperature and the bed environment were not the primary mechanism for the reduced bed returns in the canyons.

We therefore speculate that the canyon geometry itself is the cause of the reduced echo power, and the effect manifests itself as attenuation uncertainty. The linear regression model assumes that geometric spreading of the radar signal $[G]_{dB}$ is known explicitly as a function of ice thickness, surface elevation, and radar positioning (Eq. 3.1b). The derivation of Eq. 3.1a assumes minimal variation in geometric spreading over the radar's pulse-limited footprint [33, 65]. For thick ice covering a gently sloping bed, this is often reasonable. However, we speculate that near the steep, narrow canyon walls in the DIC transition zone, d_{ice} variation within the pulse-limited footprint exceeds a threshold value for this assumption to remain valid. Further research should assess the need for topographic corrections at appropriate slope angle and ice thickness thresholds. Additionally, alternative attenuation correction

methods which account for topographic heterogeneity may benefit radar data processing.

Conclusions

A 2023 RES survey of the DIC enabled detailed analysis of canyons connecting the summit area with Sverdrup Glacier. The canyons reach depths of nearly $600m$, and represent the most likely route for draining any sub-glacial brines as hypothesized in [80]. However, specularity content and bed reflectivity values are low in the canyons, contradicting the pattern expected in the presence of hydrological features. Through the use of RES simulations, we demonstrated that radar returns from sub-glacial water within the observed topography may appear dim compared to the surrounding bed, making RES a challenging tool for sub-glacial water diagnosis in this environment. Our simulated results indicated a large, specular canal ($10m$ wide) beneath the canyon is unlikely, however we cannot preclude the existence of smaller, less continuous water bodies based solely on RES reflectivity and specularity content.

We estimated basal temperatures beneath the deepest canyon identified using a finite difference approximation of the heat equation in two dimensions. The results indicate that temperatures in the canyons may be elevated up to $18°C$ above basal temperatures on the terraces. These thermodynamic conditions may enable a saline hydrological system to exist, as discussed in [80]. Conditions exceeding the pressure melting point are unlikely along most of the canyon's floor, implying sub-glacial freshwater cannot exist.

Our work also considers some limitations of conventional RES analysis applied to sub-glacial hydrology in complex terrain. Traditional interpretation of radar data equates high reflectivity and specularity content with bodies of water. We have demonstrated that this is overly simplistic in complex terrain. Comparing actual RES bed reflectivity to simulated returns, as in [67], may offer a complimentary method for identifying and characterizing sub-glacial water with greater specificity. Further, common methods for estimating englacial

attenuation with regression analysis may be flawed where the bed environment exhibits significant heterogeneity. Resulting attenuation estimates may exhibit abnormally high uncertainty, provoking flawed interpretations of basal conditions. Future radar analysis may consider corrections for basal topography, placing greater emphasis on returned power instead of relative bed reflectivity, or alternative attenuation estimation techniques [53].

Acknowledgements

We thank the Nunavut Research Institute and the communities of Grise Fiord and Resolute Bay for granting us permission to conduct research on Devon Island. This research was supported by the National Aeronautics and Space Administration (Award: 80NSSC20K1134), the G Unger Vetlesen Foundation, and Montana State University Office for Research and Economic Development. Computational efforts were performed on the Tempest High Performance Computing System, operated and supported by University Information Technology Research Cyberinfrastructure at Montana State University. Canadian Helicopters Limited (CHL) and Natural Resource Canada's Polar Continental Shelf Program (PCSP) provided logistics, equipment, and personnel supporting RES data collection over the Devon Ice Cap. We would like to acknowledge individual contributions from Dillon Buhl, Corey Skender, Clint Baumgartner, and Joshua Brett. Their expertise and dedication to the project ensured a safe and successful 2023 field survey of the DIC. Finally, we would like to thank the two reviewers for their constructive feedback, which resulted in significant improvements to the final paper.

Appendix

Appendix A - Selected Radargrams, Reflectivity, and Specularity Content

1-D focused radargrams, aligned with bed reflectivity and specularity content, for all survey lines running approximately perpendicular to Sverdrup Glacier ice flow. Canyon *A* and *B* are shown as appropriate. Flight paths for the radargrams are mapped in Fig. 3.6a. Flight *DEV3_PER0a_Y79a* is the flight closest to the hypothesized brine network, and each transect is numbered in increasing order approaching Sverdrup Glacier.

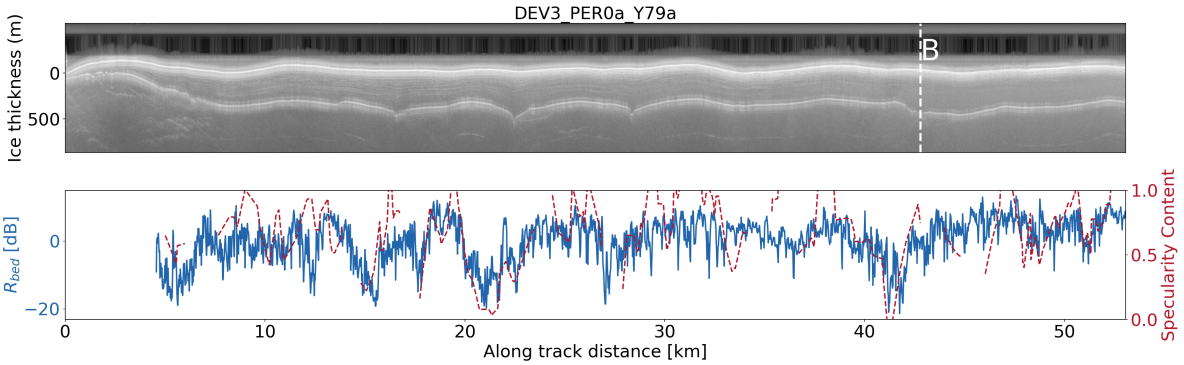


Figure A1: Radargram, reflectivity, and specularity content for *DEV3_PER0a_Y79a*

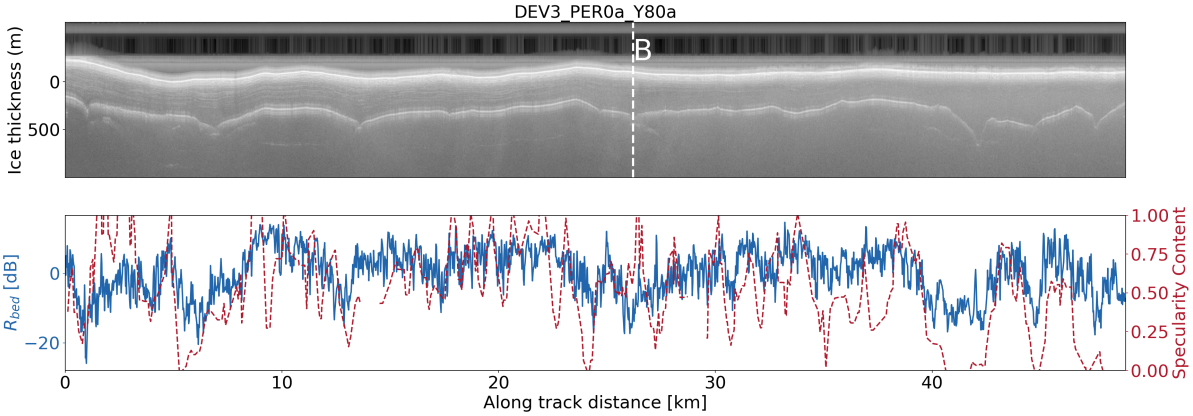


Figure A2: Radargram, reflectivity, and specularity content for *DEV3_PER0a_Y80a*

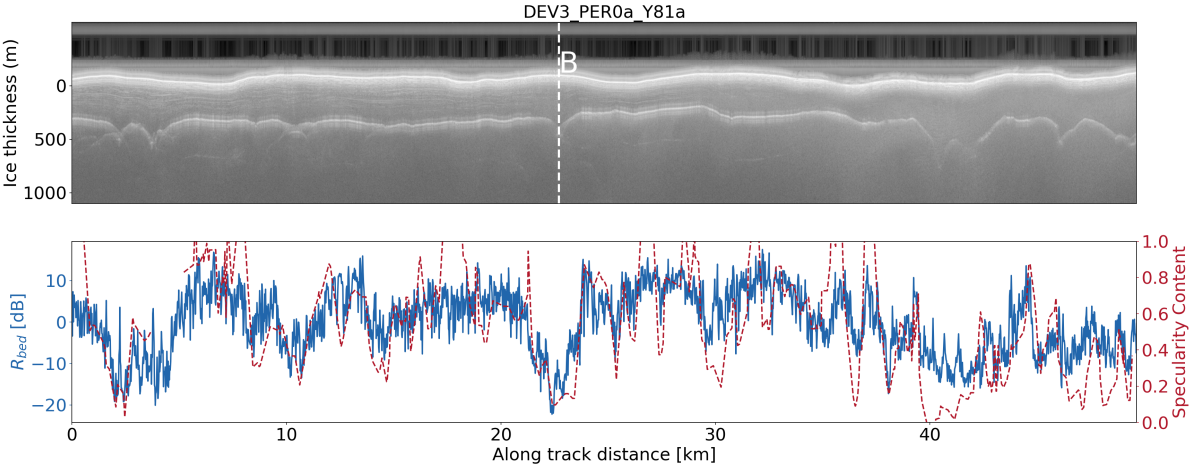


Figure A3: Radargram, reflectivity, and specularity content for *DEV3_PER0a_Y81a*

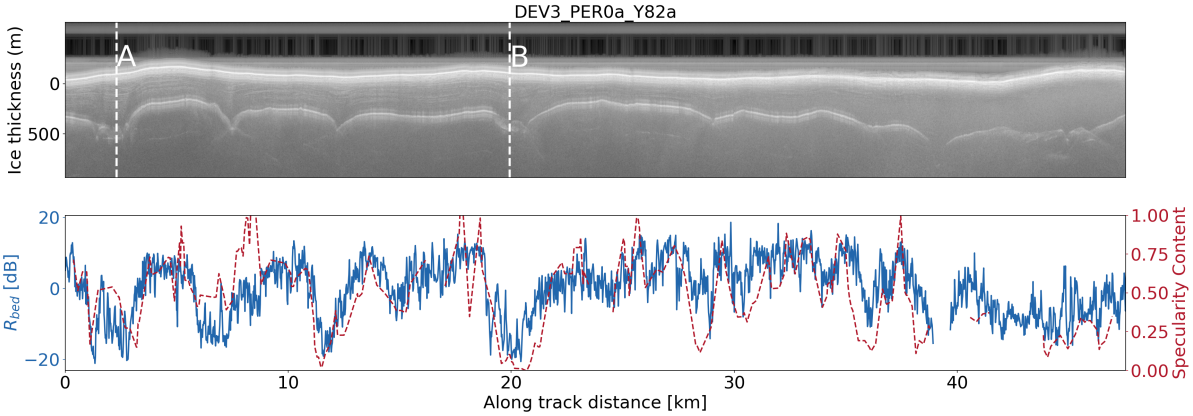


Figure A4: Radargram, reflectivity, and specularity content for *DEV3_PER0a_Y82a*

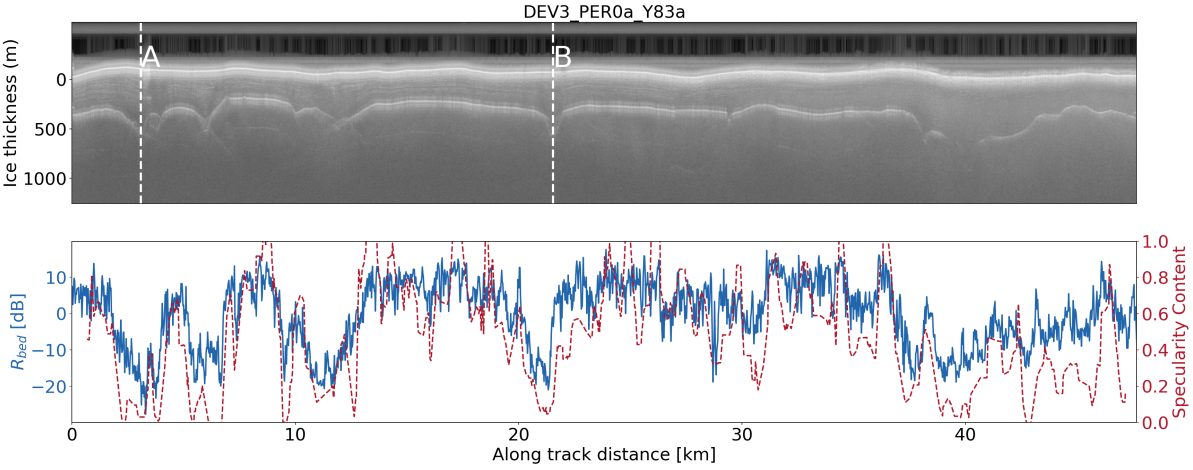


Figure A5: Radargram, reflectivity, and specularity content for *DEV3_PER0a_Y83a*

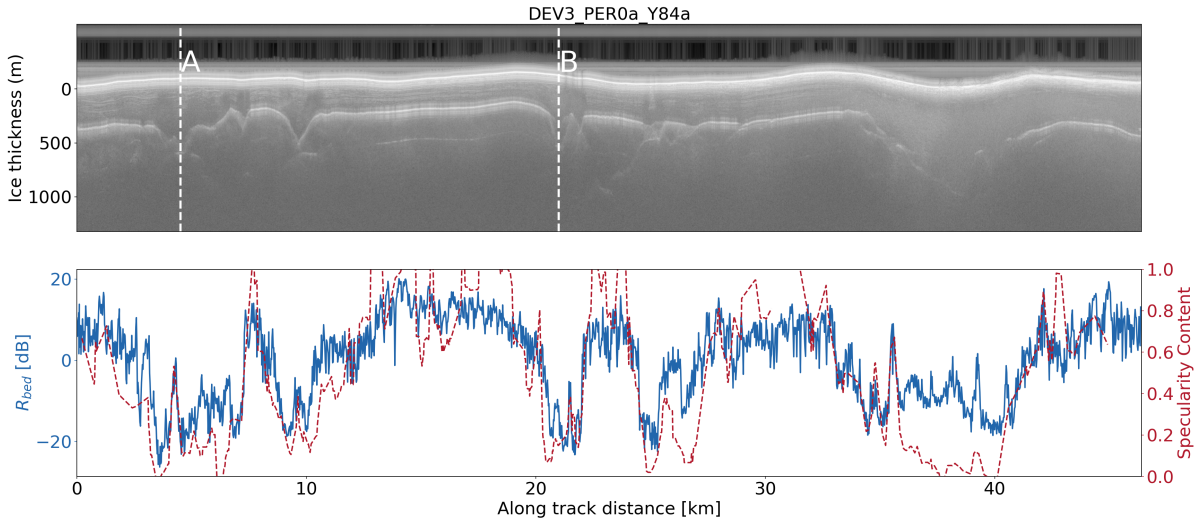


Figure A6: Radargram, reflectivity, and specularity content for *DEV3_PER0a_Y84a*

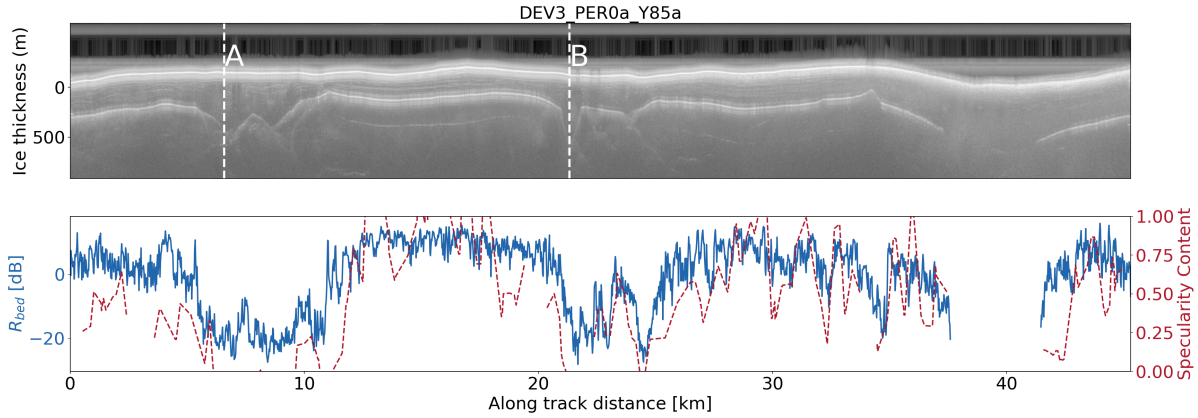


Figure A7: Radargram, reflectivity, and specularity content for *DEV3_PER0a_Y85a*

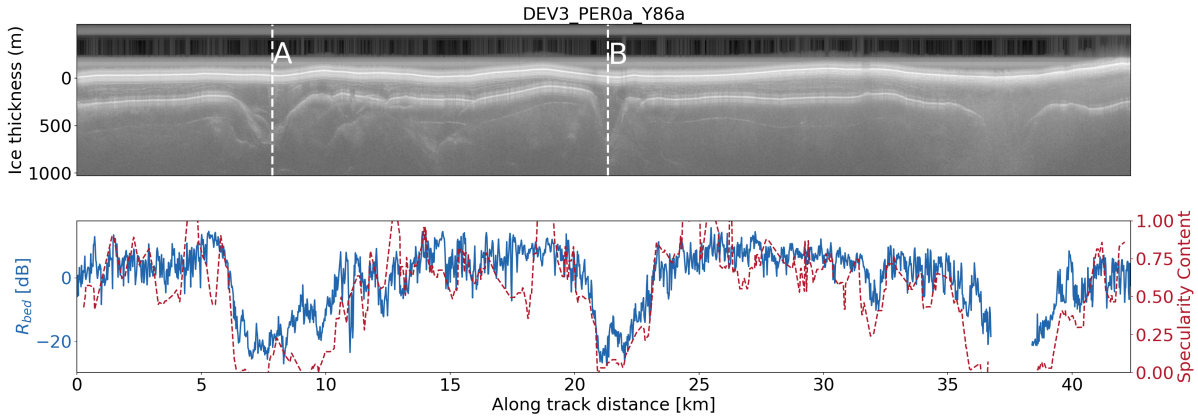


Figure A8: Radargram, reflectivity, and specularity content for *DEV3_PER0a_Y86a*

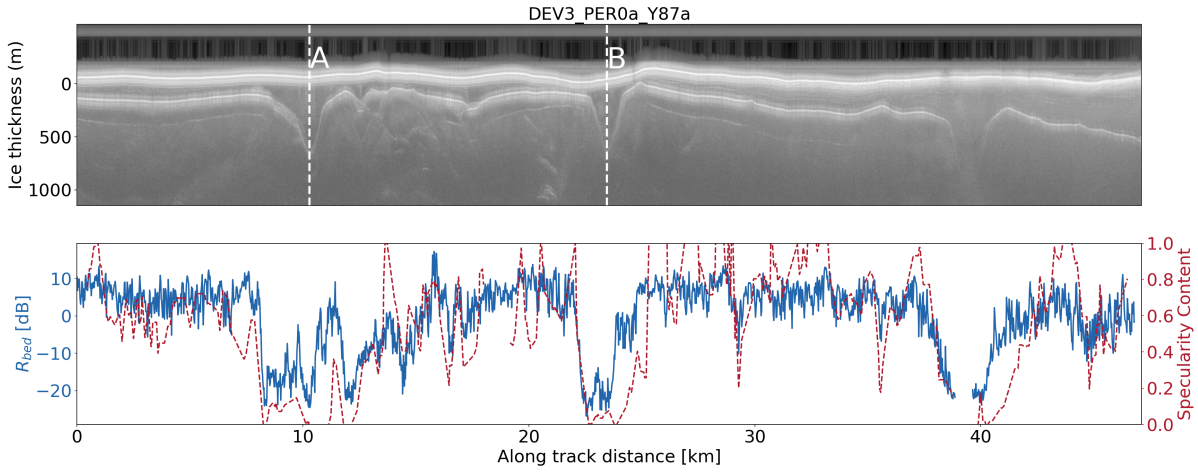


Figure A9: Radargram, reflectivity, and specularity content for *DEV3_PER0a_Y87a*

Appendix B - Modeled Canyon Geometry

Modeled Canyon B geometry for each flow-perpendicular survey line. The actual canyon cross-section from the radar data is superimposed to demonstrate fit. The locations for each canyon cross-section are mapped in Fig. 3.6a. Flight *DEV3_PER0a_Y79a* is the flight closest to the hypothesized brine network, and each transect is numbered in increasing order approaching Sverdrup Glacier.

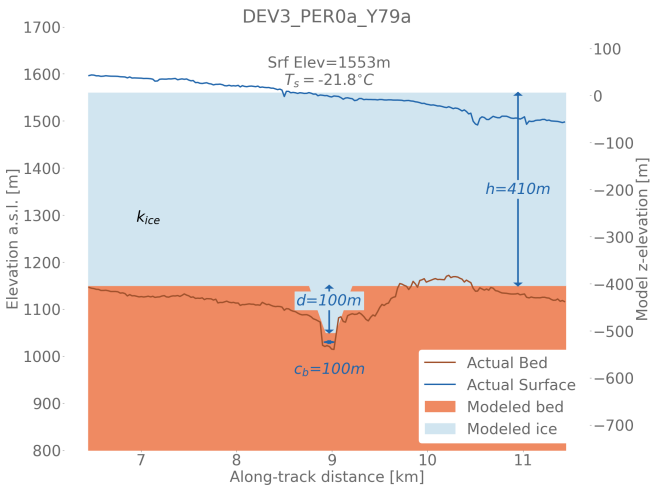


Figure B1: Canyon B model geometry for *DEV3_PER0a_Y79a*

Appendix C - Basal Roughness Approximation

Basal roughness is commonly discussed in the literature over longer length scales (hundreds of meters to km) which are easily captured by RES [4, 35]. When creating the bed DEM for our simulations, we incorporate roughness over distances significantly longer than the radar's along-track resolution of $\sim 15m$ explicitly, because this surface is created from the RES bed picks. However, roughness over distances near the radar wavelength, which contributes to divergent scattering of the radar signal, is not easily captured through RES. In order to approximate roughness over these shorter distances, we use a correlation length $l_c = 15m$ several times our DEM resolution ($l_f = 5m$) as an approximation of small-scale

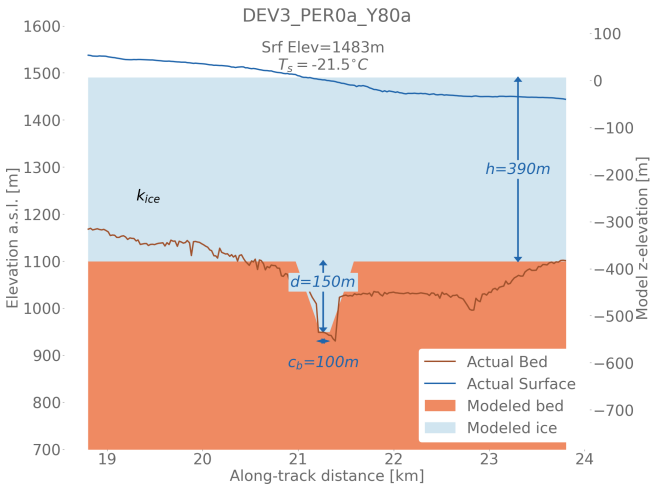


Figure B2: Canyon B model geometry for *DEV3_PER0a_Y80a*

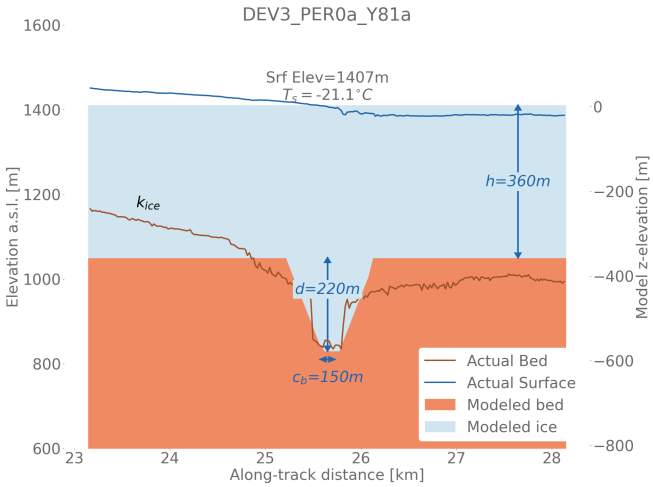


Figure B3: Canyon B model geometry for *DEV3_PER0a_Y81a*

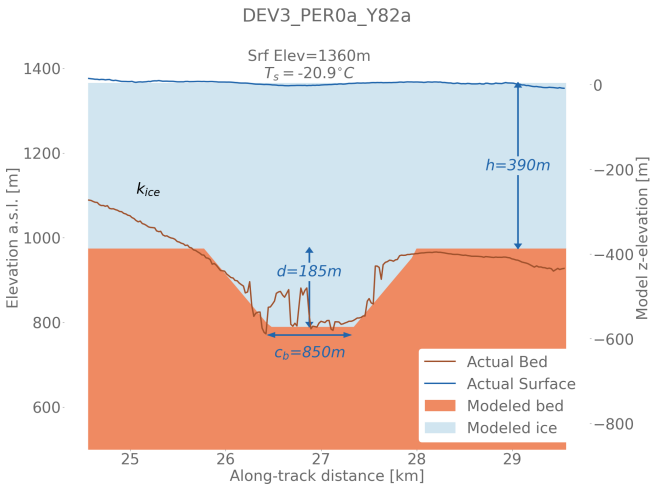


Figure B4: Canyon B model geometry for *DEV3_PER0a_Y82a*

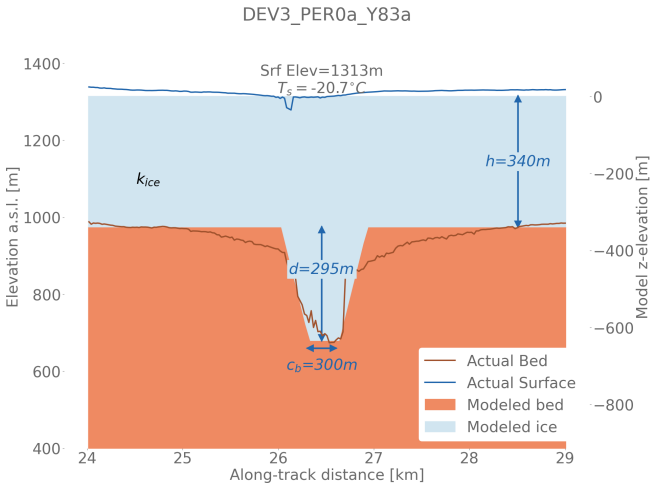


Figure B5: Canyon B model geometry for *DEV3_PER0a_Y83a*

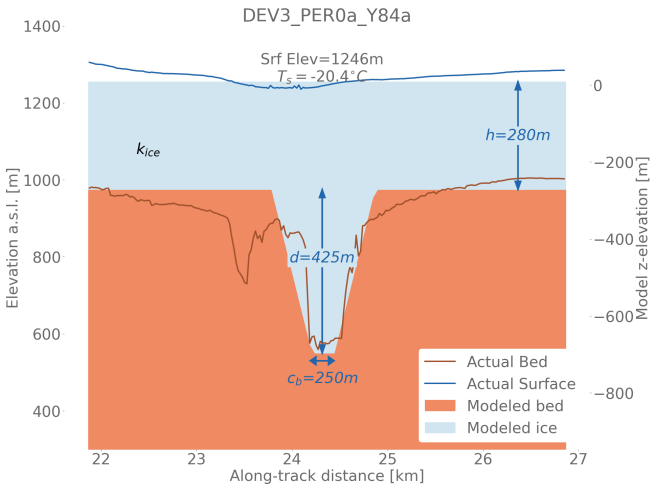


Figure B6: Canyon B model geometry for *DEV3_PER0a_Y84a*

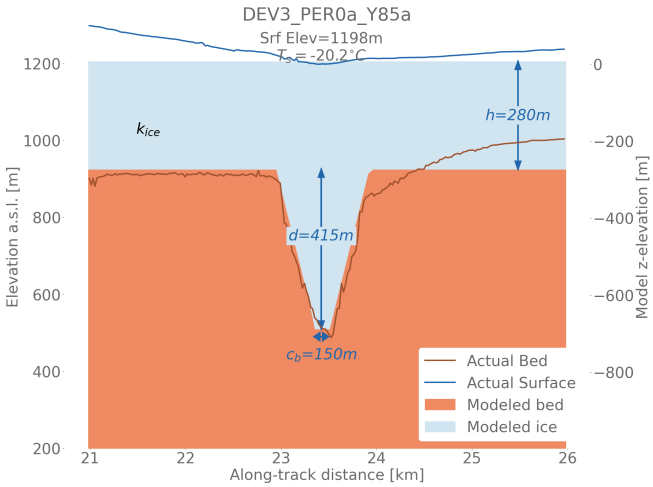


Figure B7: Canyon B model geometry for *DEV3_PER0a_Y85a*

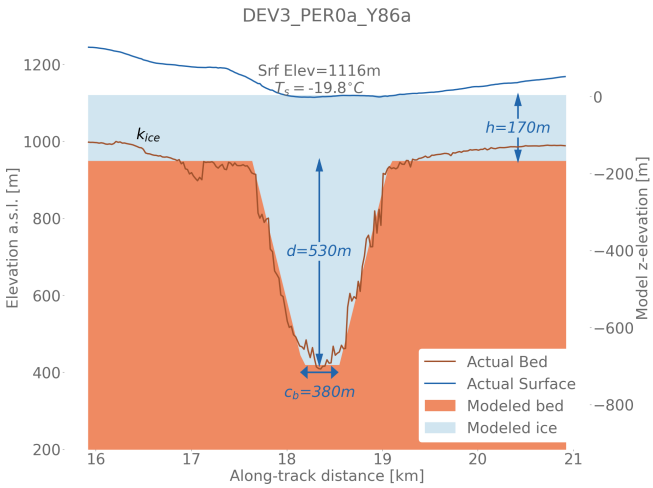


Figure B8: Canyon B model geometry for *DEV3_PER0a_Y86a*

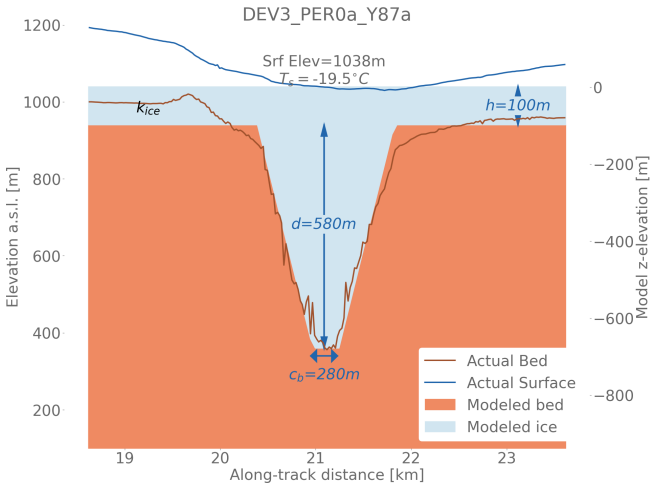


Figure B9: Canyon B model geometry for *DEV3_PER0a_Y87a*

roughness.

To identify the appropriate roughness magnitude, we downloaded ATLAS/ICESat-2 geolocated photons which transect a small area of exposed canyon and terrace features immediately west of DIC [60]. We assume this adjacent sub-aerial topography is representative of the sub-glacial topography in the transition zone.

We filter the data for observations with a minimum of "medium" signal confidence as described in the user documentation [60], resulting in mean along-track resolution of $9-16cm$. We sampled the top of three terrace features similar to the terrain near Canyon B, over a distance of $500 - 700m$. A Savitzky-Golay filter with window length $15m$ was applied to each sample data set to approximate a "smooth" surface at our chosen l_c ($S_{SG}(x)$). We then define surface roughness as the standard deviation of the difference between measured photon height $S(x)$ and $S_{SG}(x)$ in Eq. 3.7, where N is the number of photons in the data set.

$$\sigma = \sqrt{\frac{\sum_i^N \left(S_{SG}(x_i) - S(x_i)\right)^2}{N-1}} \tag{3.7}$$

Measured σ for our three sampled locations ranged from $0.22m$ to $0.35m$. We assume the average value of our basal roughness beneath DIC in the transition zone falls within this range. Simulations with the Canyon B bed topography were run with $\sigma_{bed} = 0.2m$ and $0.35m$.

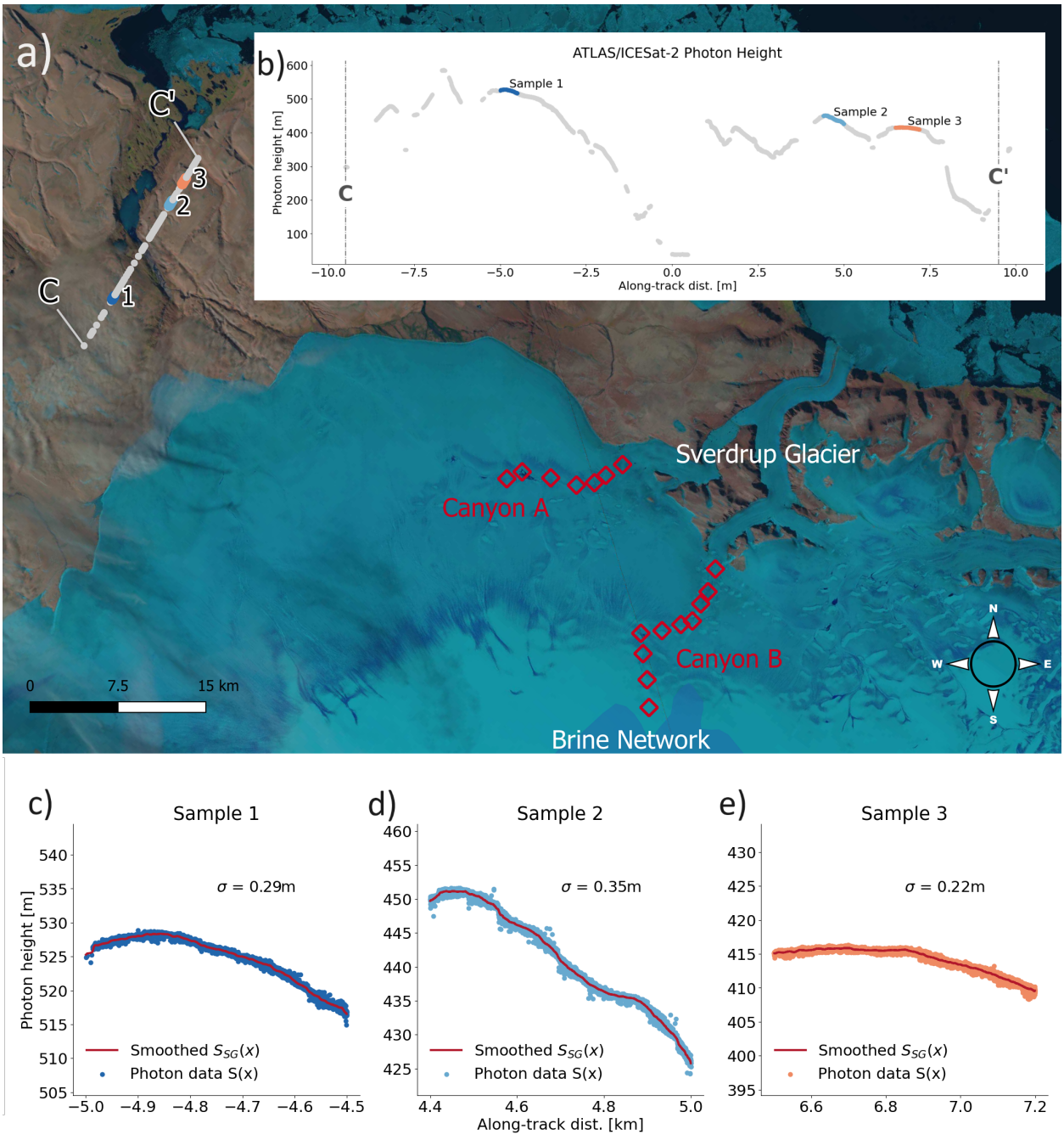


Figure C1: a) Location of ATLAS/ICESat-2 photons (C-C') with Landsat-09 imagery from July 31,2023 as background [97]. Canyons, brine network, and Sverdrup Glacier are labeled for reference. b) Photon height and location of three sampled terraces. c) - e) show photon height $S(x)$ and smoothed height $S_{SG}(x)$ for each sample, with resulting calculated roughness σ.

CHARACTERIZING THE SUB-GLACIAL ENVIRONMENT OF LOWER THWAITES GLACIER USING RADAR MODELING

Contribution of Authors and Co-Authors

Manuscript in following chapter

Author: Chris Pierce

Contributions: prepared the original draft, led the design and execution of experiments, performed data analysis, and participated in the field work to collect RES data from Thwaites Glacier.

Author: Mark Skidmore

Contributions: provided oversight and partial funding, as well as significant editorial contributions.

Author: Lucas Beem

Contributions: provided important context for the project conceptualization, made significant editorial contributions, and led the field team responsible for RES data collection over Thwaites Glacier.

Author: Don Blankenship

Contributions: provided leadership support, funding, and programmatic resources for the investigation and RES data collection over Thwaites.

Author: Ed Adams

Contributions: provided significant editorial support and contributed to experimental design.

Author: Christopher Gerekos

Contributions: contributed the original simulator software, assisted in experimental design, model validation, and provided significant editorial support.

Author: Won Sang Lee

Contributions: provided funding and logistics support for the Thwaites RES data collection, as well as editorial contributions. EA provided significant editorial review and advisory support.

Author: Choon-Ki Lee

Contributions: made a significant contribution to planning and execution of the Thwaites Glacier RES survey, provided input on the simulation experimental design, and provided editoral support.

Manuscript Information

Chris Pierce, Mark Skidmore, Lucas Beem, Don Blankenship, Ed Adams, Christopher Gerekos, Won Sang Lee, and Choon-Ki Lee

Journal of Glaciology

Status of Manuscript:
_X_Prepared for submission to a peer-reviewed journal
____ Officially submitted to a peer-reviewed journal
____ Accepted by a peer-reviewed journal
____ Published in a peer-reviewed journal

Cambridge University Press

Abstract

We employed a radar backscattering simulator to model basal returns for over $400km$ of radar echo sounding (RES) data from Thwaites Glacier in West Antarctica, initially assuming a homogeneous basal substrate. The modeled variations in bed returned power exhibited strong correlation with actual RES data in 30% of our simulated flight segments, which we consider evidence for a relatively homogeneous glacier bed in these locations. Other sites (37%) demonstrated improved fit quality when hydrology or substrate transitions were introduced in the bed material model. The remaining simulated segments (33%), were diagnosed as having more complex heterogeneity in the bed substrate. The spatial distribution of complex heterogeneity appears to coincide with asymmetric patterns in the RES specularity content, which has been interpreted in previous studies as a signature for channelized hydrology. Conversely, the homogeneous substrate locations coincide with areas of fast-moving ice in western Thwaites. Our simulation method may be broadly useful in diagnosing sub-glacial conditions from RES data. The method distinguishes between reflectivity variations induced by material heterogeneity vs. topography, which can be challenging to interpret with existing analysis methods.

Introduction

Thwaites Glacier, the largest glacier of the the Amundsen Sea Embayment in West Antarctica, contains enough ice to raise global sea levels by approximately $60cm$ [37, 55, 81, 108]. Thwaites has exhibited rapidly accelerating ice loss over the past several decades, losing $634Gt$ of ice and contributing $1.8mm$ of sea level rise between 1979-2017 [57, 74]. Its retrograde bed geometry is recognized as inherently unstable, and recent evidence suggests irreversible collapse is already underway [42, 72, 88]. Significant retreat of the Thwaites grounding line could initiate a widespread collapse of the West Antarctic Ice Sheet (WAIS),

triggering rapid sea level rise on the order of several meters [81].

The sub-glacial environmental characteristics near the current grounding line will exert direct control on the progression of changes to Thwaites Glacier, and by extension the entire WAIS. Spatial heterogeneity of bed roughness and substrate materials such as sediments, clays, till, and bedrock all impact basal friction, which provides resistance to ice acceleration [75]. The geographic location of distributed sub-glacial hydrological structures such as lakes, canals, or hydrated tills will reduce basal shear stress [7, 28, 36]. Conversely, concentrated structures such as Röthlisberger or Nye channels can efficiently transport basal water from upglacier, enhancing grounding line retreat [83, 106, 107].

The characterization of subglacial environments by airborne radar echo sounding (RES) is a well established research approach that informs many glaciological investigations, including ice dynamics, hydrology, and ice core site selection [13, 65, 83, 101]. In hydrologic investigations, the high dielectric contrast between glacier ice, liquid water, and other substrate materials (e.g. bedrock, clay, frozen tills) is exploited. Observations of elevated RES reflectivity are commonly interpreted as information about the sub-glacial hydrological network [9, 13, 78].

The Thwaites sub-glacial hydrological system has been the subject of several studies. In 2004-2005, the University of Texas Institute for Geophysics (UTIG) conducted the Airborne Geophysical Survey of the Amundsen Embayment (AGASEA), which provided extensive RES observations across the entire Thwaites catchment. From these data, [83] identified a pattern of elevated reflectivity and specularity content upstream from a bedrock ridge feature $45 - 70km$ from the grounding line. Downstream of this ridge, radar returns exhibited more asymmetric specularity content. [83] hypothesized that the radiometric change indicated a hydrological transition beneath Thwaites Glacier, with distributed water structures dominating the upstream hydrology, and largely channelized features below the bedrock ridge. Additionally, a series of connected, active sub-glacial lakes approximately

$70 - 170km$ from the grounding line were interpreted from satellite-based radar altimetry data [51, 91]. [31] also modeled the most likely persistent channelized drainage routes through the lower Thwaites region, consistent with the network first proposed in [83].

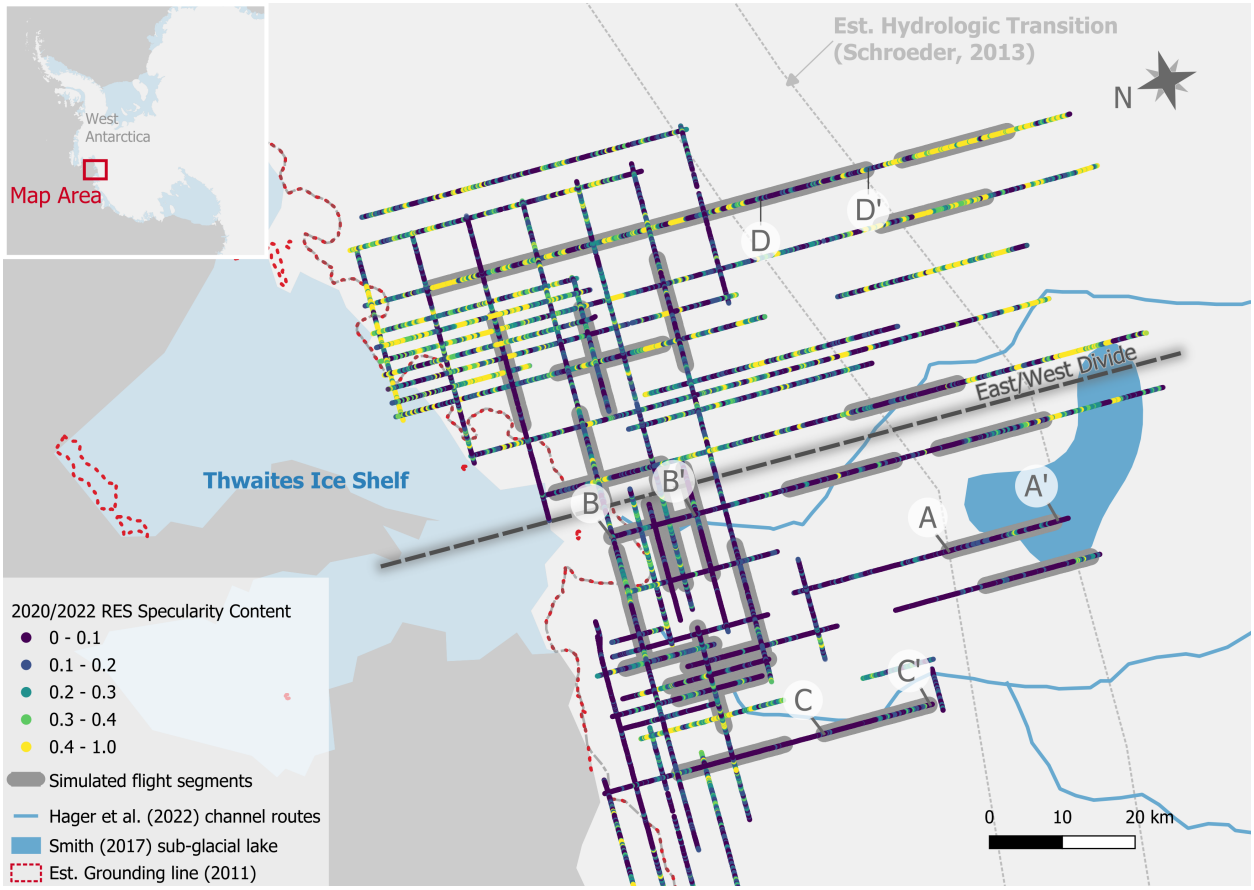


Figure C1: The downstream region of Thwaites Glacier, with locations and specularity content of all UTIG survey lines from 2020 and 2022. The 30 simulated flight segments in this study are outlined in grey. Segments A-A', B-B', C-C' and D-D' are described in greater detail in the results section. The hypothesized channel routes from [31], subglacial lake locations from [91], and hydrological transition from [83] are also shown. The estimated grounding line location from [3] is shown for reference. The dividing line at 106.5° longitude is proposed in the results as the boundary between eastern and western Thwaites.

In 2020 and 2022, UTIG revisited the Thwaites Glacier grounding zone with their helicopter-based 60MHz Multifrequency Airborne Radar Sounder with Full-phase Assessment (MARFA) instrument. The resulting RES survey provided dense coverage of the

downstream Thwaites region, including locations coincident with the proposed sub-glacial water structures in [91] and [31] (Fig. C1).

Criticisms of existing RES reflectivity analysis techniques point out ambiguities in propagation through the rough ice surface [85], dielectric properties [96], and englacial attenuation [45, 85] can all obfuscate basal reflectivity. [85] demonstrated that losses due to ice surface roughness are often negligible compared to uncertainty in attenuation or basal conditions. Consequently, improving RES validation and interpretation techniques will benefit most from distinguishing between heterogeneities in englacial attenuation vs. the basal environment.

The most conclusive method for verification of the sub-glacial hydrologic features interpreted via RES remains direct access. Successful Antarctic borehole campaigns to constrain the basal environment date back several decades [12, 20, 43, 71, 94]. However, due to the complex and expensive logistics, a relatively small number of water bodies identified via RES have been verified directly (e.g. Lake Vostok, Lake Whillans, Lake Mercer) [12, 43, 71]. RES simulators, therefore, could be a tractable test of sub-glacial environment interpretations from RES.

In this paper we extend the work of [67], which demonstrated functionality of a modeling approach to evaluate existing methods of RES interpretation. We simulated more than $400km$ of survey transects, and compared those outputs with actual reflectivity from the 2020 and 2022 UTIG surveys. Using this tool, we can assess the relative homogeneity of the glacier bed, and identify possible locations for widespread sub-glacial water within the Thwaites downstream environment. We analyze our findings geospatially within the context of previous Thwaites hydrological studies and additional evidence in the 2020 and 2022 RES data.

Methodology

RES Data Collection and Processing

The 2020 and 2022 Thwaites RES surveys were conducted using UTIG's 60 MHz MARFA instrument on an AS-350 B2 helicopter platform [48]. The airframe and instrumentation were transported to the Thwaites region on the South Korean icebreaking research vessel, RV Araon, where survey flights were launched from the ship's deck or a field camp on the Thwaites ice shelf. The helicopter was flown at a nominal height of $500m$ above ground level with a target velocity of $30m/s$. A Renishaw laser altimeter tracked aircraft height above ground level, while a Trimble Net-R9 dual frequency Global Navigation Satellite System (GNSS) and Novatel SPAN IGM-1A recorded precise aircraft positioning and orientation, as described in [48].

Data were range compressed, corrected for geometric spreading loss and aircraft position, and focused in azimuth [66]. We estimated englacial attenuation separately for the 2020 and 2022 survey data, using a linear regression model as described in [40, 83, 86]. In this method, a linear fit between geometrically corrected bed returned power $\left[P_r^G\right]_{dB}$ and ice thickness d_{ice} is identified, with the resulting slope equal to the one-way attenuation rate $\langle N_{ice} \rangle$ in $dB\,km^{-1}$ (Eq. 4.1). Bed reflectivity $[R_{bed}]_{dB}$ and system gain $[S]_{dB}$ are assumed homogeneous in this method. All quantities denoted by $[]_{dB}$ are expressed on the decibel scale, and $\langle\rangle$ indicates a depth-averaged quantity.

$$\left[P_r^G\right]_{dB} = [R_{bed}]_{dB} - 2\,d_{ice}\,\langle N_{ice}\rangle + [S]_{dB} \tag{4.1}$$

The resulting one-way attenuation rates were $14.5\,dB\,km^{-1}$ and $14.1\,dB\,km^{-1}$ for the 2020 and 2022 survey data, respectively. The 2020 root-mean-squared error (RMSE) between corrected bed power $\left[P_r^G\right]_{dB}$ and the regression fit is $9.7\,dB$, while for the 2022 survey RMSE

was $6.1\,dB$. These values are in line with [86], which identified localized attenuation rates between $10 - 16\,dB\,km^{-1}$ within $100km$ of the grounding line.

Basal returns are identified in the radar data through manually determined brackets (one above and one below), encapsulating the identified basal reflector. The magnitude of the basal return is taken as the sample with the maximum returned power between those bounds, at each vertical trace along-track. This value is modified as described above, through geometric and attenuation corrections, to determine the corrected bed reflectivity R_{bed} [5].

We also consider the specularity content of the basal reflection, as described in [84]. Specularity content measures the diffuse or specular nature of radar reflections by comparing the ratio of returned bed power over two different focusing apertures (nominally $700m$ and $2km$, [84]). Specularity content close to 0 implies that reflected energy is scattered diffusely, as may be expected with a rough bed surface. By contrast, specularity content closer to 1 implies a "flat" surface relative to the radar wavelength λ, consistent with a range of distributed sub-glacial water structures.

RES Simulations

The radar simulation method described in [67] estimates variations in returned power vs. fast time (τ) at a given location (y_i) by tracing the path and field strength of many individual rays transmitted through the ice surface then reflected from the bed. These data are compiled for a series of discrete locations y_i along a flight path to construct a simulated radargram. A conceptual model for the simulation process is depicted in Fig. C2.

The simulator requires Digital Elevation Models (DEM) for both the ice surface and glacier bed. These are derived from the actual RES surface and bed elevation data from the survey transect to be modeled. Across-track topography is estimated with data from BedMachine V2 [56], creating a 3-dimensional environment for the simulation. Both DEMs are divided into facets with characteristic length l_f, and each facet is assigned a material

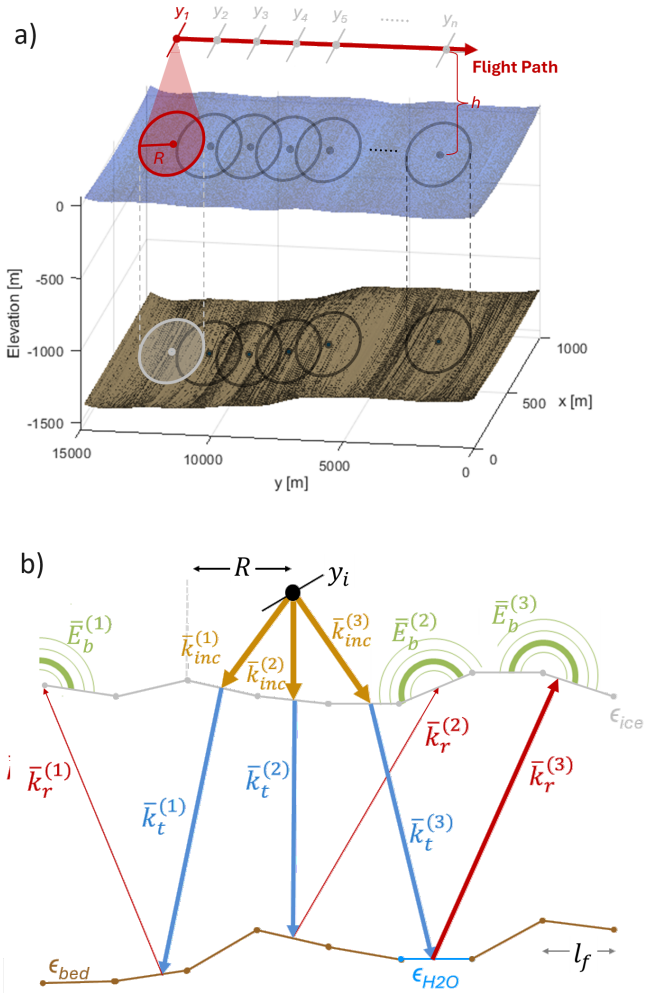


Figure C2: Conceptual model of an RES simulation is depicted. a) Antenna position at height h is incremented in the y direction along a flight path above an ice and bed surface. b) A 2-D cross-section of the simulation is shown at a single position of the radar antenna in time and space, with location y_i. The radar directs an incident electromagnetic ray $\bar{k_{inc}}$ at each facet (length=l_f) within a footprint of radius R. The ray's direction and magnitude are traced through the ice and back to the surface, where the backscattered electric field $\bar{E}_b$ is estimated at the antenna.

dielectric constant ϵ. At the ice surface all facets are assigned ϵ_{ice}, while at the bed facets can be assigned a range of permittivity values based on location, presumed substrate materials, and hydrological structures being modeled. In order to maintain a relatively simple material model, we use $\epsilon_{H2O} = 78$ when modeling water structures, and $\epsilon_{sub} = 5 - 25$ for materials which could include hydrated bedrock, clays, or tills [65, 96]. By default, we assume $\epsilon_{sub} = 5$ to represent bedrock in our material model unless otherwise noted.

Simulated radar attenuation in ice is controlled through the imaginary component of ϵ_{ice}. This value, otherwise known as the loss tangent ($\tan\delta$), is related to attenuation rate via Eq. 4.2, where λ is the radar wavelength and η_{ice} is the square root of the real component of ice permittivity [65].

$$\langle N_{ice} \rangle = \frac{20\pi\eta_{ice}\log_{10} e}{\lambda} \tan\delta \tag{4.2}$$

A flight path is defined at a height above the ice surface h. Like real RES data, simulated radargrams are range compressed and focused, although focusing apertures are shorter due to computational constraints. We choose a simulation radius R, which bounds the simulation scope at each position along the simulated flight path for efficiency. R for all simulations was between $300-350m$, chosen primarily to facilitate sufficient range migration during Synthetic Aperture Radar (SAR) focusing as described in [67]. All other relevant simulation parameters listed in Table 4.1 are intended to emulate a helicopter-based MARFA experiment.

The individual simulated observations of returned power vs. fast time (τ) are compiled along the y axis. This forms a simulated raw radargram, which estimates the returned power from the topographic and material model. Further radargram processing is consistent with real RES processing. The radargram is range compressed and focused in azimuth [67], although the focusing aperture length is shorter due to computational constraints. Simulated bed reflectivity $R_{bed,S}$ is then defined at the sample with maximum returned power between

Table 4.1: Summary of parameters used in RES simulations of Thwaites Glacier.

Parameter	**MARFA Value**
Aircraft height (h)	$500\,m$
Aircraft velocity (v_a)	$30\ m/s$
Facet length (l_f)	$5\ m$
Simulation Radius (R)	$300 - 350\,m$
Correlation length (l_c)	$15\,m$
Surface roughness (σ_{ice})	$0.2\,m$
Basal roughness (σ_{bed})	$0.2 - 1\,m$
Center frequency (f_c)	60 MHz
Bandwidth (B_w)	15 MHz
PRF[a]	6400 Hz *(30 Hz)*
Sampling frequency (f_s)	50 MHz
Pulse length (Υ)	$1\ \mu s$
Receiving window (T_r)	$50\ \mu s$
Ice Permittivity (ϵ_{ice})	$3.18\,(1 + .0015i)$[b]
Substrate Permittivity (ϵ_{sub})	$5 - 25$
Water Permittivity (ϵ_{H_2O})	78

[a] Native PRF for MARFA radar is $6400Hz$. Simulations are run at $30Hz$ to replicate effective PRF after coherent summation during data processing.

[b] Ice $\tan\delta = 0.0015$ was chosen to simulate the average estimated attenuation from the RES surveys, $\langle N_{ice}\rangle = 14.35dB\,km^{-1}$

user defined bounds in the radargram.

Homogeneous Simulations

We modeled 30 segments of RES transects from the 2020 and 2022 Thwaites surveys (Fig. C1). Each simulated segment was between $10-15km$, totalling $408km$. Many segments were chosen for their proximity to hypothesized hydrological features [31, 91], while providing sampling across the entire survey footprint. This effort encompasses over 20% of the total RES data collected over grounded ice, and is a 100-fold increase in the geographic extent simulated in [67].

For each flight segment, we first compared the actual variation in along-track reflectivity to a simulation with bed roughness $\sigma_{bed} = 0.2m$, substrate permittivity $\epsilon_{sub} = 5$, and no liquid water. This scenario, henceforth referred to as the "homogeneous" case, serves as the experimental control. This null hypothesis helps to diagnose whether variations in bed returned power can be induced by the bed topography alone, without other material or geometric variations in the sub-glacial environment.

We can deviate from the homogeneous case by manipulating two primary independent variables. Introducing spatial heterogeneity in substrate permittivity and/or small scale roughness will influence the resulting along-track simulated reflectivity:

- **Substrate permittivity** - Reflected power from the bed surface depends on the dielectric contrast between ice ($\epsilon_{ice} = 3.18$) and the substrate [65, 96]. Therefore, changing material properties along the flight line will invoke a response to the reflected power. The relationship between substrate permittivity change and the reflectivity is highly non-linear because the quantities are measured in dB. In this study, we often model transitions between bedrock ($\epsilon_{sub} = 5$) and liquid water ($\epsilon_{H_2O} = 78$), which has a large permittivity contrast of $15\,dB$. Many alternative material permittivity transitions could exist in the sub-glacial environment, although material changes with

reflectivity contrast greater than $\sim 5\,dB$ typically involve a substantial change in liquid water content.

- **Small scale roughness** - we impose a random Gaussian roughness σ_{bed} over correlation length $l_c = 15m$. Diffuse radar scattering due to roughness is highest over correlation lengths near the radar wavelength ($\lambda = 5m$) [24, 33], therefore $l_c = 15m$ was chosen as the minimum distance over which we could introduce roughness for a DEM with $5m$ resolution. Realistic estimates for σ_{bed} over this length scale are somewhat speculative. Many studies have attempted to capture basal roughness magnitude beneath Antarctic Ice Sheets [4, 35], but current methods limit analysis to km-scale correlation lengths. As in [67], we chose roughness magnitude $\sigma_{bed} = 0.2m$ for most sub-glacial DEMs. In locations where we seek to model a rougher bed, σ_{bed} was increased to $1m$. Further analysis of these constraints will be offered in the *Discussion* section.

In all of our models, we avoid tuning more than one variable from the homogeneous case at a time. It would be entirely possible to simulate multiple independent fits to the original RES data if both parameters were varied simultaneously. However, we are unlikely to have direct evidence to validate the parameter choices required to achieve such a fit. The objective of the exercise presented here is not to achieve total congruence between our simulations and the RES data, but to present a series of intuitive physical models that could explain the observed RES reflectivity. Where the simple models fit the data well, we hope to infer something about the sub-glacial environment. We also can constrain hypothetical basal conditions from locations where the simple simulations are inconsistent with the real RES data.

Evaluating Simulation Fit Quality

Simulations were performed in $10 - 15km$ segments along the flight paths depicted in Fig. C1. This simulation length was largely chosen based on computational processing

constraints. We compared the simulated relative variation in bed reflectivity to actual data from the 2020 and 2022 Thwaites RES surveys. We assess the fit between the real and simulated data sets using three different metrics:

- **Pearson correlation coefficient** (Φ_{RS}) is defined in Eq. 4.3, where σ_R and σ_S are the standard deviations for the RES and simulated reflectivity data (in dB). The covariance between the real and simulated data sets ($cov_{R,S}$) is calculated after smoothing each with a Savitzky-Golay filter to reduce high frequency noise. Φ_{RS} ranges between -1 and 1. Positive values indicate positive correlation, with higher magnitudes implying the correlation strength.

$$\Phi_{RS} = \frac{cov_{R,S}}{\sigma_R \, \sigma_S} \tag{4.3}$$

- **Standard deviation ratio** (σ_{RS}) is the ratio in standard deviation of along-track reflectivity between the real and simulated data. Values near one indicating a strong match between the magnitude of fluctuations in along-track reflectivity.

$$\sigma_{RS} = \sigma_S / \sigma_R \tag{4.4}$$

- **Range ratio** (χ_{RS}) is the ratio of the total range in reflectivity (in dB) between the real and simulated data. A value near one indicates that sharp peaks in the data are of similar magnitude.

$$\chi_{RS} = \frac{\max\left[R_{bed}\right]_{dB} - \min\left[R_{bed}\right]_{dB}}{\max\left[R_{bed,S}\right]_{dB} - \min\left[R_{bed,S}\right]_{dB}} \tag{4.5}$$

Results

RES Specularity Content

The 2020 and 2022 RES surveys included nearly $1800km$ of radar transects over Thwaites' grounded ice. Nearly all of these data were located downglacier from the bedrock ridge identified in [83]. The data exhibit some patterns in basal reflectivity and specularity content similar to the 2004-2005 UTIG RES survey. We are primarily interested in the subglacial hydrological system, and therefore RES observations over the Thwaites Ice Shelf are excluded from our analysis (Fig. C1). Further, we divide the data along $-106.5°$ longitude when comparing observations between Eastern and Western Thwaites.

Observations of asymmetry in the specularity content are noteworthy for this downstream region of Thwaites Glacier, as this formed the basis for the channelized drainage hypothesis outlined in [83]. Table 4.2 summarizes key findings in the specularity content data from the 2020/2022 Thwaites survey. Mean specularity content across all included data from the 2020 and 2022 surveys was 0.18 ± 0.19. Similar to observations from [83] in the 2004-2005 AGASEA survey, radar transects oriented North/South have higher mean specularity than transects oriented East/West. The two-tailed p-value for this orientation dependence is $<< 0.01$, indicating $> 99\%$ confidence that this observed orientation dependence is statistically significant [6].

If we divide the data along the East / West dividing line, geographic patterns in the specularity content emerge. East of the dividing line, mean specularity content was more than double the value for Western Thwaites (0.23 vs. 0.11, Table 4.2). A p-value $<< 0.01$ indicates $> 99\%$ probability that this observed difference from East to West is significant.

Table 4.2 also demonstrates asymmetry in the specularity content changes across the dividing line. East of the divide we observe significant asymmetry, with higher mean specularity content in North/South oriented transects than those running East/West

Table 4.2: Specularity content for various subsets of the 2020/2022 Thwaites Survey data.

Data Subset	**Mean SC**[a]	**Std. Dev**	**# of Pts**
Entire Survey	0.18	0.19	97519
N/S transects	0.20	0.20	71916
E/W transects	0.14	0.15	25603
East of Divide	0.23	0.20	57382
N/S transects	0.25	0.21	47110
E/W transects	0.16	0.16	10272
West of Divide	0.11	0.14	40137
N/S transects	0.10	0.13	24806
E/W transects	0.12	0.14	15331

[a]SC=Specularity Content

(0.25 ± 0.21 vs. 0.16 ± 0.16). West of the dividing line, we observe lower asymmetry, with specularity content of 0.10 ± 0.13 for North/South oriented transects and 0.12 ± 0.14 for East/West transects. P-values for both comparisons are many orders of magnitude below 0.01, indicating high confidence in the statistical significance of these results.

Comparing RES and Simulated Reflectivity

The simulation method assumes constant englacial attenuation, and power losses at the ice surface are governed by the DEM which mimics the real ice surface. Eliminating these common uncertainties ensures that variations in simulated bed reflectivity are the result of basal topography and substrate materials. Comparisons between simulations and actual RES reflectivity are, therefore, helpful in diagnosing sub-glacial environmental conditions.

We introduce a simple framework for characterizing the fit quality of our simulations to the actual RES along-track reflectivity:

1. **Homogeneous fit:** 9 out of our 30 simulated flight segments (30%) exhibited similarity to the real RES data across all three fit quality metrics, with positive correlation $\Phi_{RS} > 0.2$, standard deviation ratio $\sigma_{RS} > 0.6$, and range ratio $\chi_{RS} > 0.6$. We interpret these locations as having relatively homogeneous bed material and sub-glacial roughness along-track.

2. **Hydrology fit:** for 6 of the remaining segments (23%), the fit could be significantly improved by introducing a water feature over an area at least $500m$ along-track and extending across the simulated bed DEM. In these scenarios, parameters for the remainder of the bed DEM remain unchanged from the homogeneous simulation.

3. **Substrate transition:** for 4 segments (10%), fit quality improvement was achieved by introducing a coupled change in both σ_{bed} and ϵ_{sub} over an area $> 500m$ along-track and extending across the DEM. Such a coupled change could represent a material transition from a deformable substrate such as clay or till to bedrock.

4. **Heterogeneous:** for the remaining 11 segments (37%), the homogeneous simulation demonstrated a poor fit to the RES data. Improving the fit quality would require complex manipulations of the bed DEM variables in multiple locations along the segment.

We will evaluate representative case studies from each category to build intuition for the above framework. This should establish an understanding of the simulation method's potential and limitations.

Homogeneous Fits Figure C3a shows the focused radargram for a $14km$ segment between A and A' in Figs. C1 and C8. Between $500m$ and $3000m$ along-track we observe a $20\,dB$ reflectivity peak. This bright reflection is coincident with the location of a hypothesized active sub-glacial lake from [91]. From the RES surface elevation (z_s) and

ice thickness (d_{ice}) measurements, we can estimate the hydraulic potential along-track (Eq. 4.6), assuming zero effective pressure at the bed [8]. In Eq. 4.6, ρ_{ice} is ice density, and ρ_{H_2O} is the density of water. Water will flow along hydraulic potential gradients, and pool in locations that are hydraulically flat. Hydraulic potential for the same flight segment is plotted in Fig. C3b, with color corresponding to variation in R_{bed}. This shows the bright reflector may be contained within a catchment. The reflector also coincides with a distinct increase in specularity content (Fig. C3b)

$$\psi = d_{ice}\left(\frac{\rho_{ice}}{\rho_{H_2O}} - 1\right) + z_s \tag{4.6}$$

All of this evidence might warrant classifying this reflector as a "definite" or "dim" lake in the schema suggested by [9]. However, this interpretation comes with inherent uncertainty. The system of active lakes connected to this region demonstrated two discharge cycles between 2013 and 2018 [51, 91]. In the later drainage event, the location between A and A' did not demonstrate a significant change in ice surface elevation. This indicates the hypothesized sub-glacial water feature may have been misinterpreted, or ephemeral. Further, we expect higher reflectivity and/or specularity from a distributed body, such as a lake, than from channelized water features [67, 83]. However, the reflectivity peak ($\sim 2000 - 2500m$ along-track) appears to occur on a hydraulic slope, which is inconsistent with a lake interpretation.

Eq. 4.6 assumes zero effective bed pressure, which may be reasonable for large distributed water features (such as a lake), but unlikely if water is flowing in channels [8, 15, 31]. Spatial variation in effective bed pressure is likely to contribute significantly to the hydraulic potential, adding uncertainty to this type of analysis. Therefore, despite elevated R_{bed} of $20\,dB$ and a corresponding increase in specularity content, interpreting this location as sub-glacial water could be premature without additional analysis.

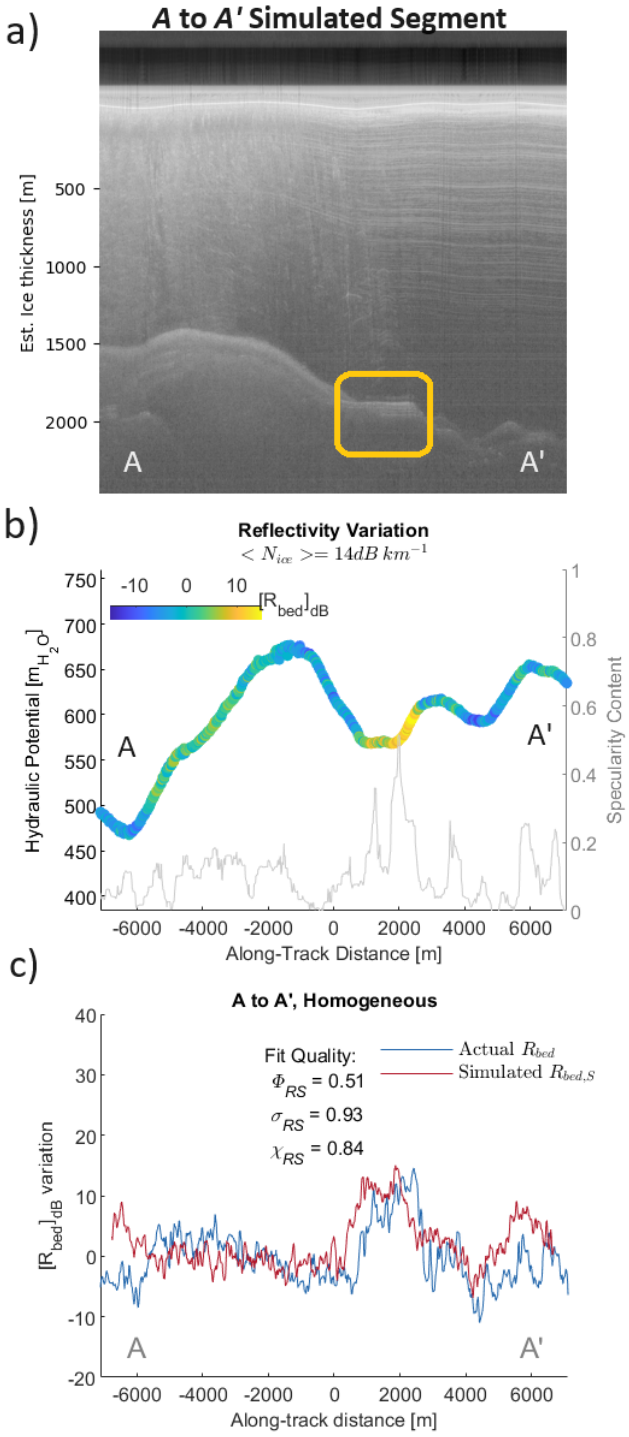


Figure C3: a) Focused radargram for the simulated segment between A and A'. The bright reflector is boxed. b) Graph of hydraulic potential, R_{bed} variation, and specularity content for the same simulated segment. c) Along-track reflectivity variation R_{bed} and simulated homogeneous $R_{bed,S}$. Locations A and A' correspond to the locations in Figs. C1 and C8. The hypothesized lake boundaries from [91] intersect this segment from $\sim 1500m$ to $7000m$ along-track.

Table 4.3: Fit quality metrics for homogeneous simulation segments. Locations correspond to numbered locations in Fig. C8.

Location	$\mathbf{\Phi_{RS}}$	$\sigma_{\mathbf{RS}}$	$\chi_{\mathbf{RS}}$
(1)	0.40	0.61	0.71
(2)	0.26	0.85	0.77
(3)	0.38	0.96	0.94
(4)	0.28	1.09	1.08
(5)	0.44	0.67	0.61
(6)	0.24	0.72	0.82
(7)[a]	*0.51*	*0.93*	*0.84*
(8)	0.29	0.66	0.79
(9)	0.42	0.69	0.70

[a] *A* to *A'*, Figs. C1 and C8

Figure C3c compares the along-track variation in R_{bed} vs. $R_{bed,S}$ for the homogeneous simulation of the same $14km$ segment. We can visually confirm the correlation of peaks and valleys between the two data sets, resulting in $\Phi_{RS} = 0.51$. Both data sets exhibit similar standard deviations and peak heights, as indicated by $\sigma_{RS} = 0.93$ and $\chi_{RS} = 0.84$, respectively. The strong fit with the homogeneous simulation indicates the $20\,dB$ increase in along-track R_{bed} may result entirely from topography. A material change with a large dielectric contrast (such as a transition from rock to water) is not required to induce the reflectivity increase between $500m$ and $3000m$.

Table 4.3 summarizes the fit quality metrics for all simulated segments identified as homogeneous.

Hydrologic Fits Twenty one of our 30 simulated flights do not exhibit a strong homogeneous fit as described above. Of these simulated segments, the fit quality for six can be improved by changing the permittivity over part of the bed DEM from the default value $\epsilon_{sub} = 5$ to $\epsilon_{H2O} = 78$. We impose this change over an area at least $500m$ along-track and extending across the simulated bed DEM, which could represent an extensive area of distributed water (e.g. a sub-glacial lake or seawater intrusion). Our modeling choice is justified by the geographic location or alternative evidence in the radar data, such as increased specularity content.

Figure C4a shows the radargram for an $11km$ segment located from B to B' in Figs. C1 and C8. An abrupt reflectivity transition of nearly $20\,dB$ occurs around $-1.8km$ along-track. Fig. C4b compares the along-track variation in R_{bed} to the homogeneous simulation case. Fit quality metrics $\Phi_{RS} = 0.21$, $\sigma_{RS} = 0.43$ and $\chi_{RS} = 0.55$ imply the bed has lower homogeneity than the previous example from A to A'.

The $20\,dB$ change in reflectivity is approximately coincident with the grounding line, and therefore we consider this change in reflectivity could mark the transition between grounded and floating ice. In Fig. C4c, we simulate the same segment with a substrate permittivity change from $\epsilon_{rock} = 5$ to $\epsilon_{H_2O} = 78$ at $-1.8km$ along-track. The material transition induces a strong reflectivity response, and fit quality improves to $\Phi_{RS} = 0.90$, $\sigma_{RS} = 1.18$ and $\chi_{RS} = 1.22$. We therefore interpret this bed material model as a plausible interpretation of the RES data.

This pattern is repeatable for three additional flight segments near the Thwaites grounding zone (locations 10, 11, and 13 in Figs. C6 and C8). Two others occur further inland (locations 14 and 15, Figs. C6 and C8), where the modeled water feature is consistent with a peak in specularity content. For each of these simulated segments, fit improvements are outlined in Fig. C6. Along-track comparisons of R_{bed} vs. $R_{bed,S}$ can be found in the *Appendix*.

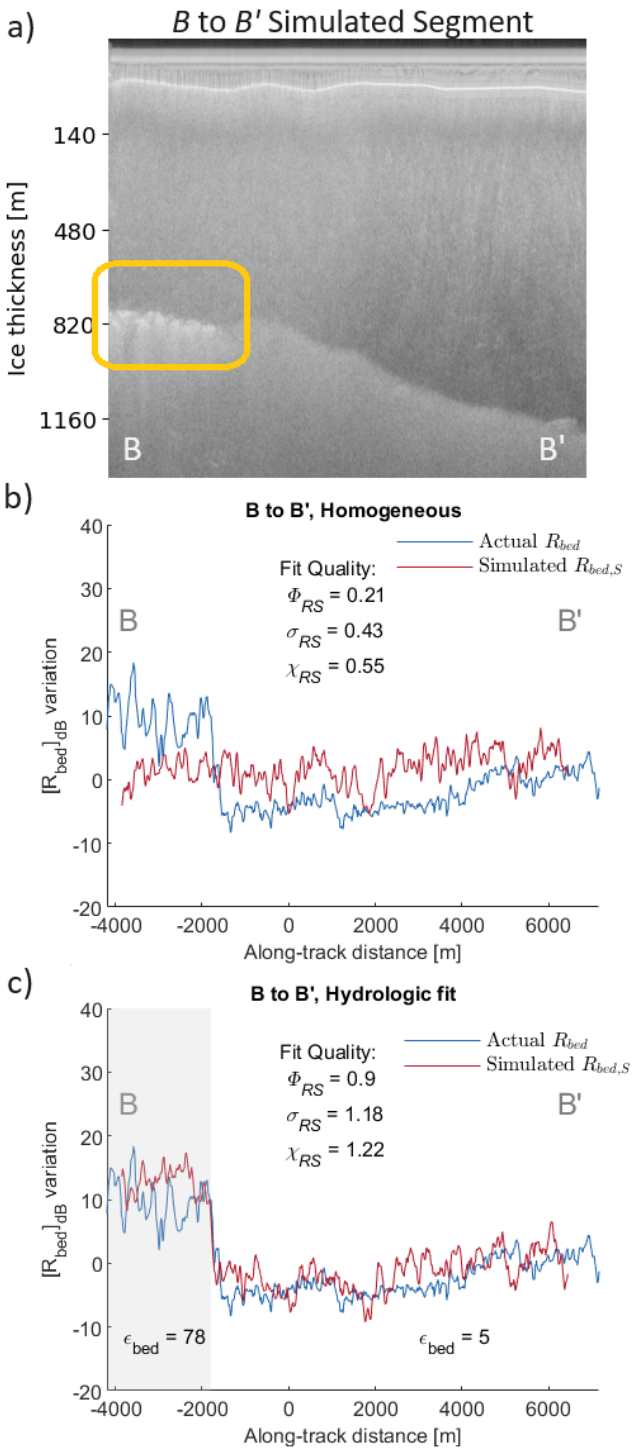


Figure C4: a) 1-D focused radargram for the $11km$ simulated segment from B to B' (see Figs. C1 and C8) The bright basal reflector is highlighted. b) Comparison of R_{bed} and $R_{bed,S}$ for the homogeneous simulation. c) Hydrologic simulation comparision of R_{bed} vs. $R_{bed,S}$, where the basal material is changed to liquid water ($\epsilon = 78$) from $-4.1km$ to $-1.8km$ along-track.

Substrate Transitions Four additional simulated segment locations from the 2020 and 2022 RES survey exhibit R_{bed} patterns consistent with a simple substrate transition over a single area $> 500m$ along-track. A $14km$ segment from *C* to *C'* (Figs. C1 and C8), on the western edge of the lower Thwaites catchment, demonstrates this type of heterogeneity. There are no obvious bright reflectors in the radargram (Fig. C5a), though R_{bed} spans a range of $28\,dB$ over the segment. The homogeneous simulation (Fig. C5b) has fit metrics $\Phi_{RS} = 0.09$, $\sigma_{RS} = 0.40$ and $\chi_{RS} = 0.46$, indicating the homogeneous model does not fit the RES data well. However, the fit is binary. The section from $-5.7km$ to $-1.2km$ demonstrates poor coherence with the actual variation in R_{bed}, while the rest of the homogeneous simulation appears to correlate.

This shift in fit quality is paired with an apparent reduction in specularity content to near zero (Fig. C5c). Low specularity indicates that incident radar energy is scattered more diffusely, and therefore may imply a change in basal roughness [84]. When the basal roughness σ_{bed} is increased to $1m$ over the segment from -5.7 to $-1.2km$ along-track (Fig. C5d), we see improved correlation ($\Phi_{RS} = 0.74$), but the magnitude of bed reflectivity variation only shows marginal improvement ($\sigma_{RS} = 0.46$ and $\chi_{RS} = 0.54$).

The results from Fig. C5d indicate a change in roughness alone may not explain the along-track variation in R_{bed} from *C* to *C'*. We could reasonably speculate that the change in roughness indicates a material transition, with a corresponding change in the bed permittivity. Figure C5e shows results from such a coupled scenario, where the lower roughness value $\sigma_{bed} = 0.2m$ is paired with $\epsilon_{bed} = 10$ (e.g. clay bearing or sandy till), and higher roughness $\sigma_{bed} = 1.0m$ is associated with $\epsilon_{bed} = 5$ (e.g. rough bedrock) [96]. Fit quality metrics $\Phi_{RS} = 0.81$, $\sigma_{RS} = 0.9$ and $\chi_{RS} = 0.73$ all imply this is a possible interpretation of the sub-glacial environment consistent with the RES data at this location.

Three additional simulations exhibit improvement in fit quality if we assume either a simple change in roughness (segment *16* in Fig. C8) or similar coupling of bed material and

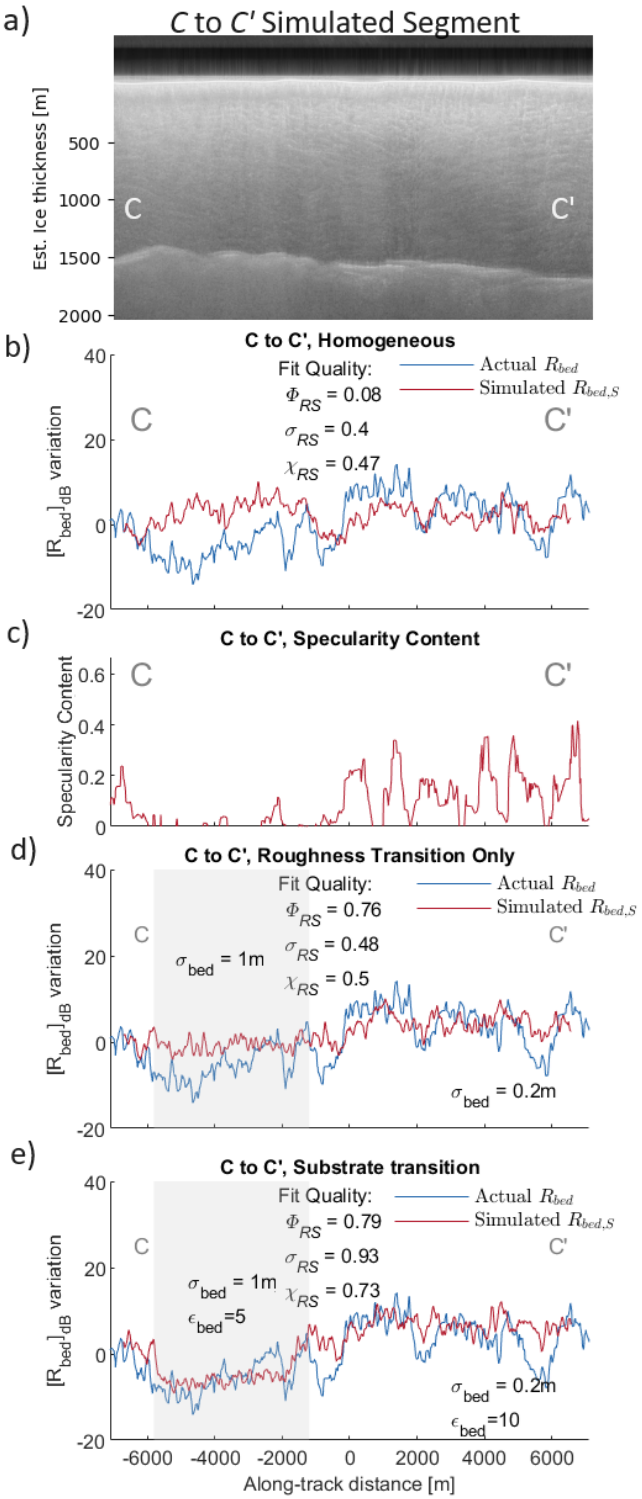


Figure C5: a)1-D focused radargram for the $14km$ simulated segment from C to C' (Figs. C1 and C8) b) Comparison of along-track R_{bed} and $R_{bed,S}$ for the homogeneous scenario c) Specularity content from the RES data for the simulated segment d) R_{bed} vs. $R_{bed,S}$ comparison for a roughness only transition (constant ϵ_{sub}) e) R_{bed} vs. $R_{bed,S}$ comparison for a substrate material transition (coupled ϵ_{sub} and roughness change).

roughness (segments *17* and *18* in Fig. C8). Fit improvements for these simulations are summarized in Fig. C6.

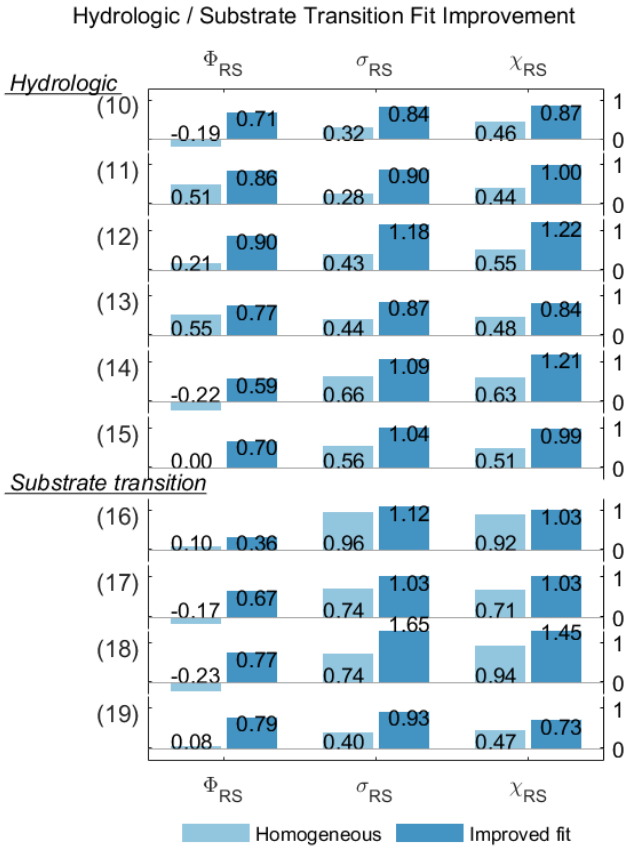


Figure C6: Improvement for all simulations with hydrologic and substrate transition fits. The numbers correspond to simulated segment locations in Fig. C8. Segments 12 and 19 correspond to *B* to *B'* and *C* to *C'* in Figs. C1 and C8.

Heterogeneous For the remaining 11 simulated segments (37%), the homogeneous simulation scenario exhibits poor fit quality to the RES data. Achieving improved fit requires manipulation of more than one simulation variable without logical coupling, or abrupt material changes in multiple locations along the bed DEM. Our methodology allows such adjustments within the simulation environment, and these complex manipulations may achieve a high quality fit to the RES reflectivity data. However, without consistent

corroborating evidence for multiple material changes at the bed (such as specularity content or geographic location near the grounding line), fitting these data would simply optimize our two primary model variables independently. The resulting solutions could be non-unique or physically unrealistic. Therefore, instead of attempting to diagnose specific spatial patterns in bed heterogeneity to explain the along-track R_{bed} variation, we assume that the bed in these locations has more complex heterogeneity than the other simulated flight segments.

The $14km$ segment from D to D' (Figs. C1 and C8) is an example of heterogeneity. Fig. C7 shows homogeneous fit quality metrics of $\Phi_{RS} = 0.07$, $\sigma_{RS} = 0.37$, and $\chi_{RS} = 0.46$, confirming a relatively poor fit between R_{bed} and $R_{bed,S}$. This segment exhibits a range of nearly $30\,dB$ in R_{bed} along-track, with at least two bright reflectors centered at $-4.4km$ and $4.5km$. Adjacent to each of these reflectors are areas of dim basal reflectivity, where R_{bed} is reduced by nearly $30\,dB$. In the center of the segment between -3.5 to $1.0km$ along-track, variation in both R_{bed} and $R_{bed,S}$ is of lower magnitude, but there is limited correlation in trends between the two series.

None of the large fluctuations in R_{bed} are present in the homogeneous simulation scenario for the D to D' segment. This result implies that the bright basal reflections more likely arise from basal heterogeneity than topographic variations. Improving the fit quality between R_{bed} and the simulated $R_{bed,S}$ could include the addition of water structures near the two bright reflectors, as well as adding roughness or reducing ϵ_{sub} in locations with dim R_{bed} in the RES data. All of these simultaneous changes over a short distance would be speculative. Instead of attempting to fit the RES data, we diagnose this location as having complexity in the basal environment which the homogeneous model does not capture.

Table 4.4 summarizes the fit quality metrics for all 11 simulated segments identified as heterogeneous. Figure C8 displays the location of all 30 simulated segments, with color coding indicating the bed diagnostic taxonomy described above.

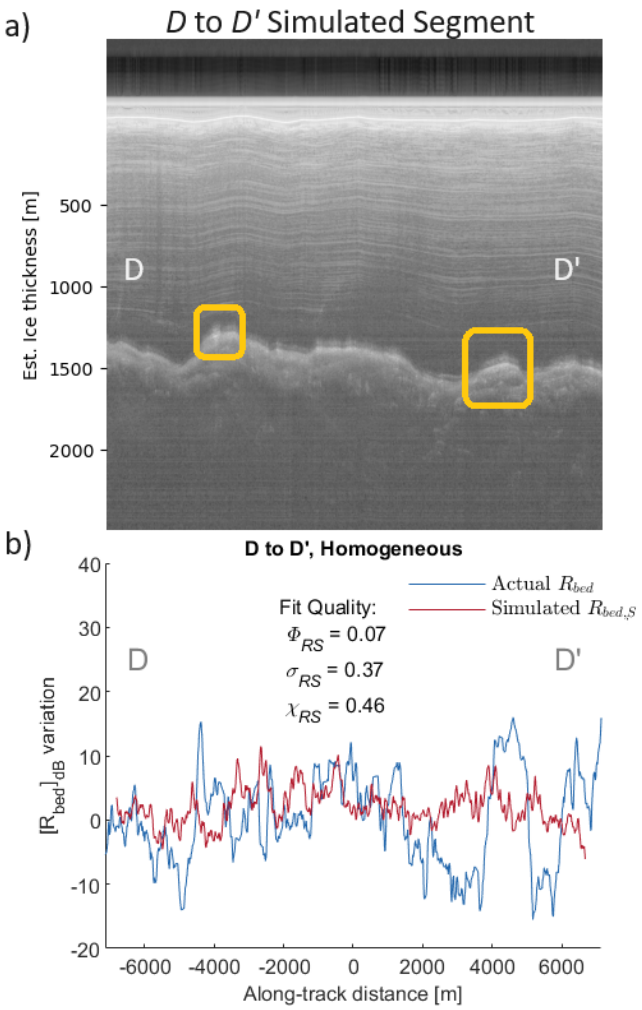


Figure C7: a)1-D focused radargram and b) plot of R_{bed} and $R_{bed,S}$ for the simulated segment between D and D' exhibiting complex heterogeneity. D and D' correspond to locations in Figs. C1 and C8.

Table 4.4: Fit quality metrics for heterogeneous simulation segments. Locations correspond to numbered locations in Fig. C8.

Location	$\mathbf{\Phi_{RS}}$	$\sigma_{\mathbf{RS}}$	$\chi_{\mathbf{RS}}$
(20)	0.19	0.41	0.40
(21)	0.30	0.75	0.50
(22)[a]	*0.07*	*0.37*	*0.46*
(23)	0.26	0.60	0.41
(24)	0.65	0.38	0.33
(25)	-0.04	0.35	0.32
(26)	0.33	0.40	0.48
(27)	-0.24	0.50	0.37
(28)	-0.34	0.33	0.35
(29)	0.23	0.48	0.44
(30)	-0.09	0.46	0.53

[a] *D* to *D'* segment (Figs. C1 and C8)

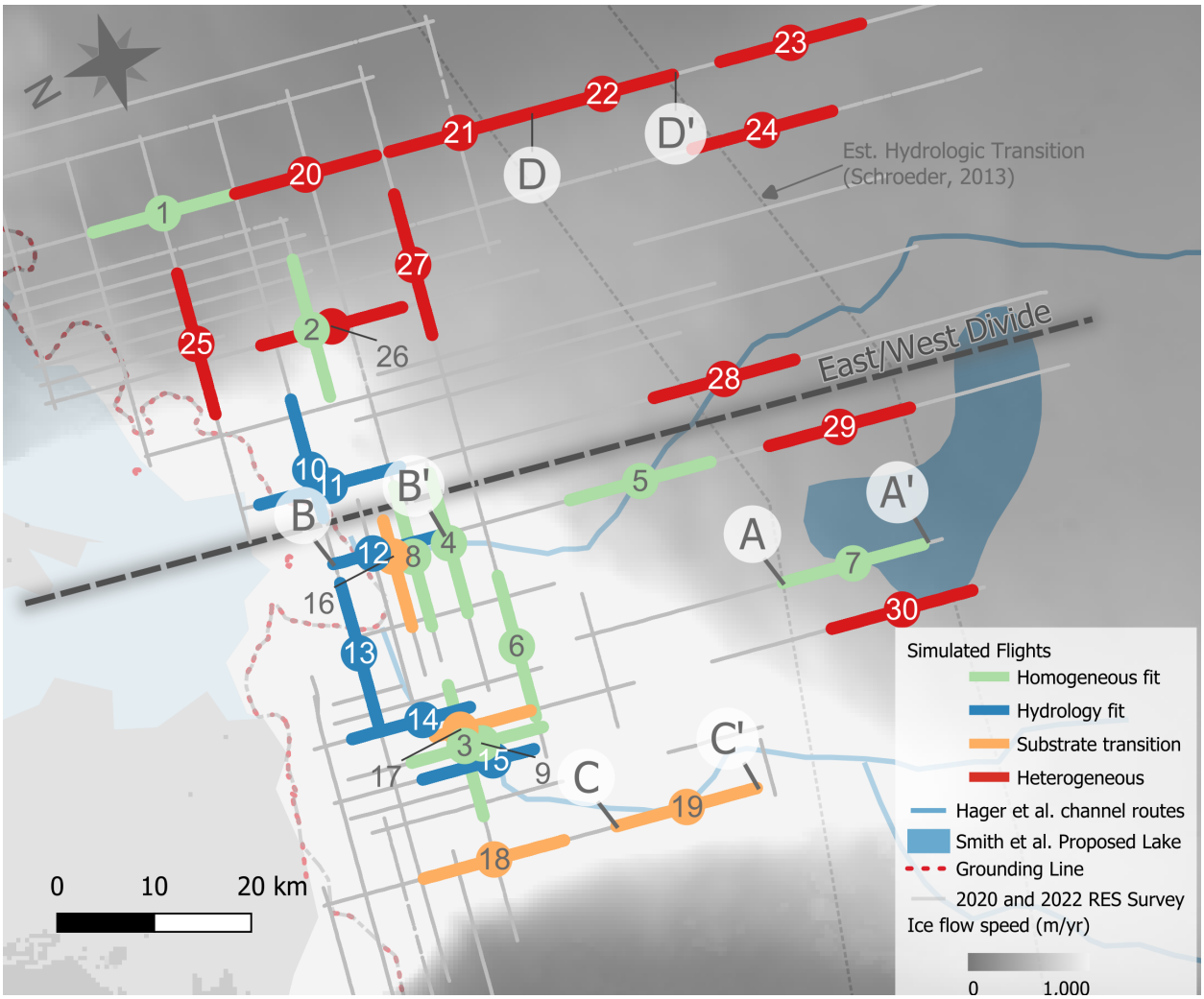


Figure C8: Map of all simulated flight segments, categorized by fit quality. Grayscale background indicates MEaSURES ice speed in $m\,yr^{-1}$ [52, 73].

Discussion

Geographic Interpretation of Bed Heterogeneity

The simulated segments were located across the lower catchment, with 13 east of the proposed East/West divide (43%) and 17 to the west (57%). Our interpretations of bed homogeneity or heterogeneity from the RES simulations appear to contrast across the proposed East/West divide at $-106.5°$. Of the nine segments identified as homogeneous fits, seven were west of the divide. Conversely, a similar fraction of the heterogeneous segments (9 of 11) were to the east (Fig. C8). This disparity across lower Thwaites could be indicative of an East/West transition in the substrate materials and hydrological system.

Many of the locations in western Thwaites identified as homogeneous, hydrologic, or material transition fits were beneath ice with velocity exceeding $1 km\, yr^{-1}$ (Fig. C8). Deformable substrate material and widespread, distributed hydrologic systems are likely for these segments [64]. [49] indicated that ice flow across western Thwaites may be controlled by topographic features, including prominent volcanoes along the western shear margin. Our findings are consistent with this interpretation, where variations in bed reflectivity align with topography and basic substrate transitions employed in our RES simulation methods.

The heterogeneity observed in eastern Thwaites could be explained by the opposite interpretation (Fig. C8). This region of Thwaites is believed to have fewer topographic features regulating ice flow [49]. [85] observed a sharp contrast in bed reflectivity near the eastern Thwaites shear margin, which was inferred to indicate changing basal conditions as a primary control. The heterogeneity inferred through our simulations supports this conclusion. The substrate materials across eastern Thwaites may vary considerably. Concentrated channels, which exhibit less pronounced but broader reflectivity peaks [67], may also contribute to R_{bed} variations that do not align with topography across the area.

Heterogeneity observed east of $-106.5°$ longitude correlates with asymmetry in the RES

specularity content data. We observe significantly higher mean specularity content in the east, as well as asymmetry between North/South and East/West oriented transects (Table 4.2 and Fig. C1). Similar asymmetry in an extensive 2004-2005 survey was the primary evidence for a hypothesized hydrological transition $45 - 70km$ upstream of the Thwaites grounding line [83].

Based on our simulation results and observed specularity content from the 2020 and 2022 surveys, we propose a revised interpretation of the Thwaites downstream hydrological system. In the east, the hydrological system is likely dominated by concentrated water structures, as proposed in [83]. However, west of $-106.5°$, our evidence points to broad areas of homogeneity, with distributed water bodies near the grounding zone. We speculate that fast-moving ice on the west side of the glacier significantly alters the local hydrological system through frictional heating and other dynamic processes at the bed surface.

In RES data, it is common to observe variations in R_{bed} exceeding $20\,dB$ over a few km along-track. Bright reflectors are commonly interpreted as water structures, especially if they are located in hydraulically flat topography [65, 78, 107]. We have demonstrated through our simulation technique that variations of this magnitude may result from sub-glacial water (as in B to B'), or topographic features (as in A to A'). This finding is consistent with [68], which demonstrated topographically induced R_{bed} variations beneath Devon Ice Cap of nearly $30\,dB$. Inferring the basis for specific R_{bed} fluctuations in RES data can be challenging with existing interpretation techniques. The simulation methodology described here may be a practical tool for this diagnosis.

Sensitivity of RES Simulations to Model Parameters

We performed most homogeneous simulations assuming bed permittivity $\epsilon_{sub} = 5$, roughness magnitude $\sigma_{bed} = 0.2m$, and $\epsilon_{ice} = 3.18$. This is a relatively smooth interface with low dielectric contrast, possibly representing saturated bedrock beneath glacier ice [96].

Such an interface is reasonable to envision beneath Thwaites Glacier, however a wide range of alternative values for ϵ_{sub} and σ_{bed} could exist [65, 96] with unknown spatial distribution. Homogeneity does not require specific material properties, only that those properties do not change appreciably over the flight segment. Therefore, we assess the sensitivity of the diagnostic method developed here to material parameters ϵ_{sub} and σ_{bed}.

Segments 1, 4 and 7 in Fig. C8 were diagnosed as homogeneous in our initial analysis. These locations were sampled from across the study area, and each demonstrated high Φ_{RS}, σ_{RS}, and χ_{RS} values for the original homogeneous scenario. For all three segments, we ran additional simulations in which ϵ_{sub} and σ_{bed} were increased over the entire bed DEM. Figure C9 compares the changes in fit quality metrics Φ_{RS}, σ_{RS}, and χ_{RS} for these simulations.

Figure C9a shows the change in fit quality metrics when ϵ_{sub} was varied from 5 to 25, while σ_{bed} remained constant at $0.2m$. On average, we observe minimal change, with no obvious trend, for all three metrics as ϵ_{sub} increases. From these data we demonstrate that the homogeneity diagnosis is relatively insensitive to the bed permittivity. Therefore, we propose it is possible to use a broad range of dielectric constants without impacting the diagnosis of homogeneity or heterogeneity.

In Fig. C9b, σ_{bed} varies from $0.2m$ to $1m$ while ϵ_{sub} is held at 5. In these simulations, we see a 32% increase in the correlation fit metric Φ_{RS}. However, the standard deviation σ_{RS} and range metrics χ_{RS} decrease from their original values by 43% and 38%, respectively. These results demonstrate that the magnitude of topographically induced $R_{beds,S}$ variation is reduced as bed roughness increases. This reduces fit quality to the real RES data and indicates that diagnosing homogeneity is sensitive to basal roughness.

Constraints on basal roughness over short distances are challenging to ascertain beneath Thwaites Glacier. Our homogeneous simulations impose a random Gaussian roughness $\sigma_{bed} = 0.2m$ over correlation length $l_c = 15m$ by default. As mentioned in the *Methodology* section, studies of basal roughness in Antarctica typically measure over much

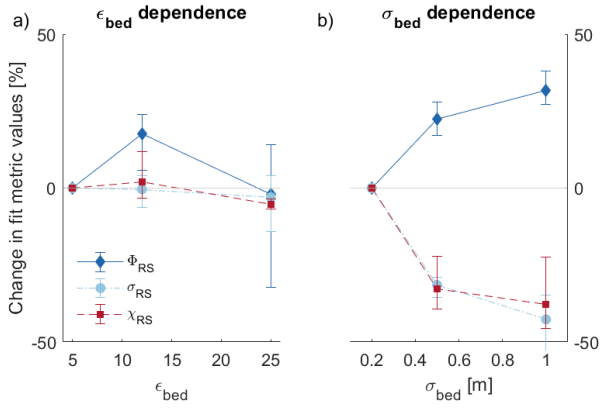


Figure C9: Fit quality metric dependence on a) ϵ_{sub} and b) σ_{bed} for homogeneous simulations of B to B'.

longer distances, leaving uncertainty on actual roughness values at length scales relevant to radiometrics.

The roughness magnitude chosen for most simulations, $\sigma_{bed} = 0.2m$, is relatively smooth for a real substrate. This magnitude is sufficient to reduce simulation artifacts such as Bragg resonance [27]. We also speculate that this value may approximate glacially eroded or soft substrates beneath fast moving ice, as is likely over large parts of our study area. As in [67], the upper bound on basal roughness magnitude ($\sigma_{bed} = 1m$) is derived from recently deglaciated Alpine topography measured at high resolution [38]. We used this value throughout the study to simulate isolated locations of bed roughness.

While we do not explicitly know basal roughness over short distances near l_c, we note that mean σ_{RS} over all simulations with homogeneous fits was 0.80. This indicates that the average magnitude of along-track $R_{bed,S}$ variation is similar to the actual R_{bed} variation. From this, we speculate that the choice for $\sigma_{bed} = 0.2m$ in this environment may be appropriate. We acknowledge that our treatment of basal roughness in this study is simplistic. The intent is to offer a plausible interpretations of the sub-glacial environment. Accurate diagnosis of basal roughness and its impact on RES over short length scales requires a more comprehensive

analysis, and represents a logical extension for this RES simulation methodology in future work.

RES Simulation Limitations

In this study, we simulated over $400km$ of RES flight segments collected in 2020 and 2022. We achieved relatively high fit quality between R_{bed} and $R_{bed,S}$ in 63% of the simulated segments, which we use as evidence for the level of relative heterogeneity in the bed properties at each location. However, we acknowledge that the simulations represent less than 25% of the 2020/2022 survey. The locations for many segments were explicitly chosen near the hypothesized features from [91] and [31], and the RES data itself is more concentrated near the grounding zone than further upglacier. While we made efforts to sample a variety of locations across lower Thwaites Glacier, these inherent inconsistencies in spatial coverage may bias our findings. The spatial patterns identified through our simulations appear compelling, however additional RES survey density with comprehensive simulation coverage would enable more definitive conclusions.

We note that the RES simulator outputs a focusable radargram similar to a real airborne RES experiment. However, computational constraints limit the SAR focusing aperture to $\sim 350m$, which is insufficient for simulating specularity content. In the future, we hope to address this constraint, as it will be helpful in reconciling hypotheses involving radiometric interpretation of sub-glacial hydrology. Finally, we also acknowledge that our thresholds for Φ_{RS}, σ_{RS}, and χ_{RS} were chosen to assess the relative fit quality between our 30 simulated segments. Interpreting homogeneity vs. heterogeneity in other locations or with other RES instruments may require different values to draw similar comparisons.

Conclusions

Our 30 simulated RES flight segments covered over $400km$ across lower Thwaites Glacier. We began with homogeneous simulations for each segment, where the basal material had uniform permittivity and roughness. After comparing these simulated outputs to real RES bed reflectivity variations, we identified 9 segments with a relatively homogeneous bed. An additional 10 simulations demonstrated a strong fit to the real along-track RES data if simple or coupled heterogeneity was introduced in the bed material over a large area of the modeled bed.

Most of the segments where a fit was achieved are on the western side of a proposed dividing line at $-106.5°$. The RES specularity content on this side of the glacier is generally low, with limited orientation dependence. Western Thwaites also has elevated ice velocity in excess of $1000m\,yr^{-1}$. The isotropic specularity signature could be indicative of this relatively homogenous basal environment, which we speculate results from the fast-moving ice.

Conversely, 11 of our simulated segments demonstrated poor fits between RES reflectivity variation and the homogenous model. These segments would require complex spatial variations along the bed DEM to achieve a fit. Hence, we diagnosed these locations as having complex heterogeneity. Complex heterogeneity was overwhelmingly observed on the eastern side of Thwaites Glacier, which is characterized by slower ice velocity, higher specularity content, and significant orientation dependence in the specularity data.

Our findings represent an evolution of the hypothesis advocated in [83], which cited asymmetry in RES specularity content as evidence of channelized hydrology across lower Thwaites. Our new RES data demonstrates this asymmetry is much stronger in eastern Thwaites than in the west, potentially implying a higher degree of channelized hydrology east of $-106.5°$ longitude. Our RES simulations appear to confirm differences in the basal

environment between eastern and western Thwaites, although further research is required to conclusively validate our results.

The RES simulation technique presented in this work was applied far more extensively than in previous efforts [67, 68]. The method demonstrates promise as a tool for diagnosing sub-glacial conditions. It may be especially helpful in identifying reflectivity variations caused by topography vs. material heterogeneity. The model will benefit from additional computational power and efficiency, enabling longer simulation segments with higher resolution DEMs. We also note more comprehensive research into small-scale roughness and substrate permittivity would enhance the realism of our simulations.

Appendix

Appendix A - Homogeneous Fits

This appendix contains along-track relative reflectivity comparisons (R_{bed} vs. $R_{bed,S}$) and fit quality metrics for all simulated segments identified as homogeneous fits in the text. Simulation segment numbers correspond to locations on Fig. C8.

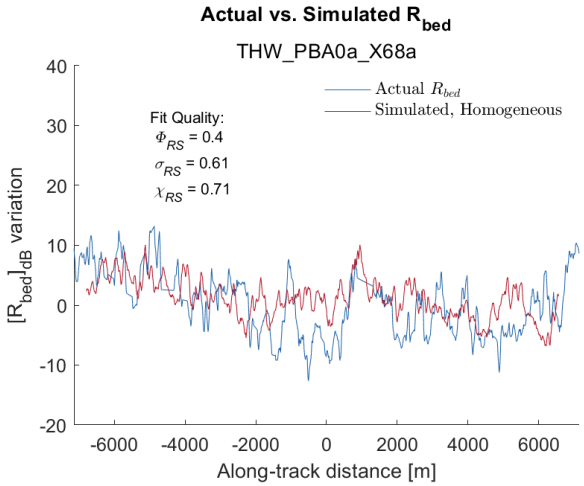


Figure C10: Simulated segment 1, R_{bed} vs. $R_{bed,S}$ comparison

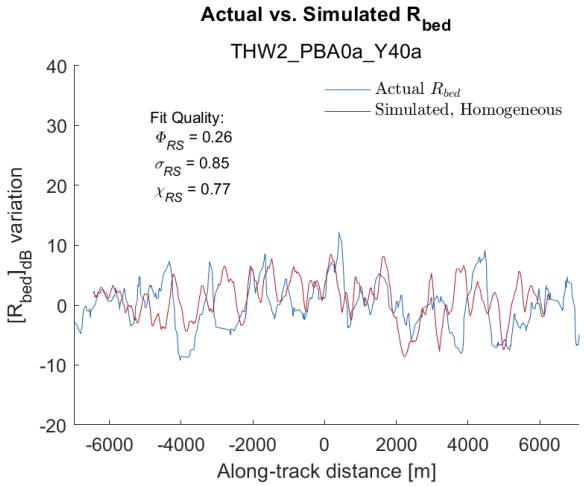


Figure C11: Simulated segment 2, R_{bed} vs. $R_{bed,S}$ comparison

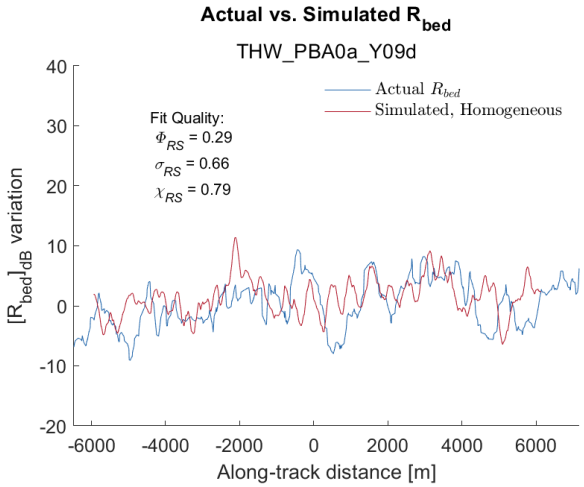


Figure C12: Simulated segment 3, R_{bed} vs. $R_{bed,S}$ comparison

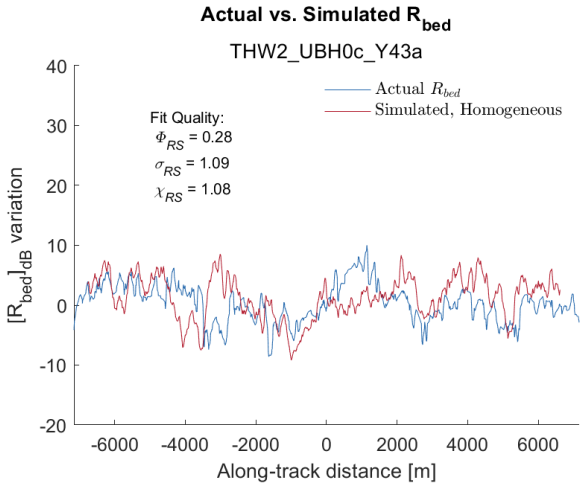


Figure C13: Simulated segment 4, R_{bed} vs. $R_{bed,S}$ comparison

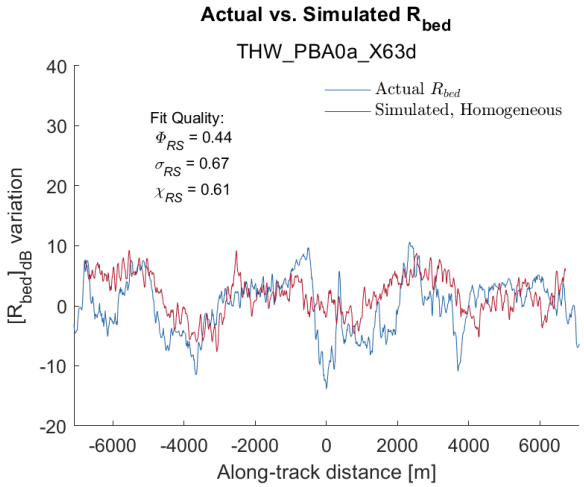


Figure C14: Simulated segment 5, R_{bed} vs. $R_{bed,S}$ comparison

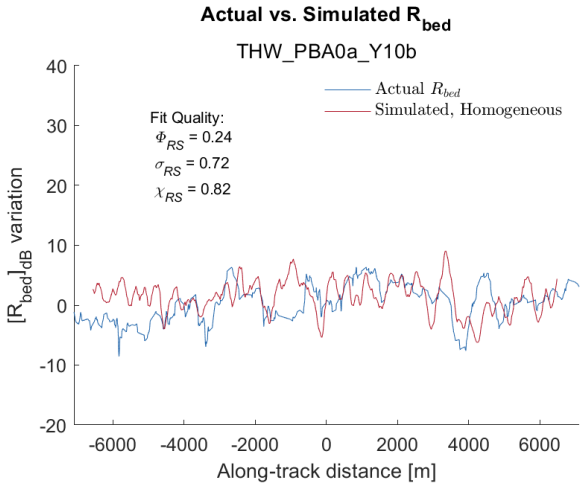


Figure C15: Simulated segment 6, R_{bed} vs. $R_{bed,S}$ comparison

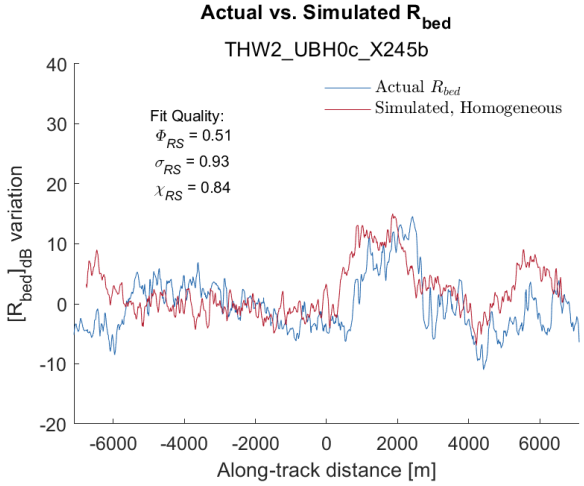


Figure C16: Simulated segment 7, R_{bed} vs. $R_{bed,S}$ comparison

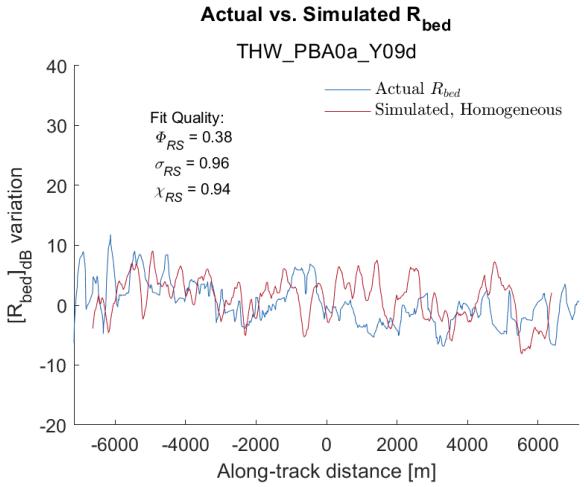


Figure C17: Simulated segment 8, R_{bed} vs. $R_{bed,S}$ comparison

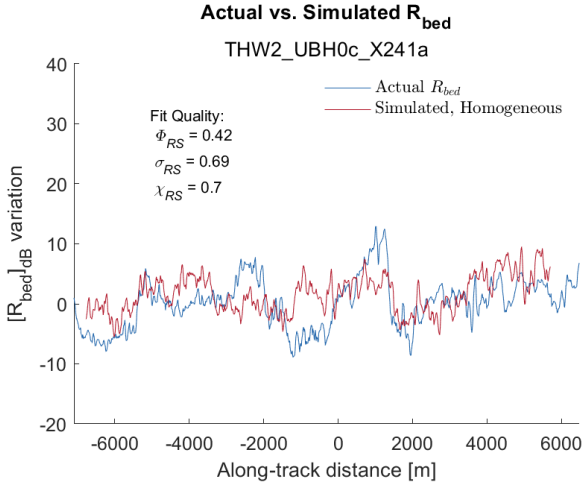


Figure C18: Simulated segment 9, R_{bed} vs. $R_{bed,S}$ comparison

Appendix B - Hydrologic Fits

This appendix contains along-track relative reflectivity comparisons (R_{bed} vs. $R_{bed,S}$) and fit quality metrics for all simulated segments identified as hydrologic fits in the text. Simulation segment numbers correspond to locations on Fig. C8.

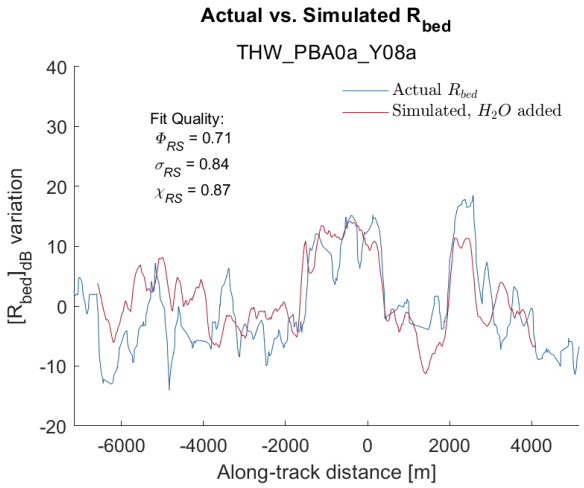


Figure C19: Simulated segment 10, R_{bed} vs. $R_{bed,S}$ comparison

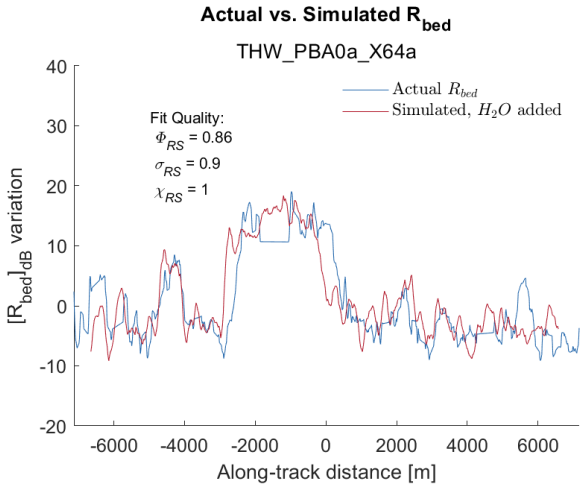


Figure C20: Simulated segment 11, R_{bed} vs. $R_{bed,S}$ comparison

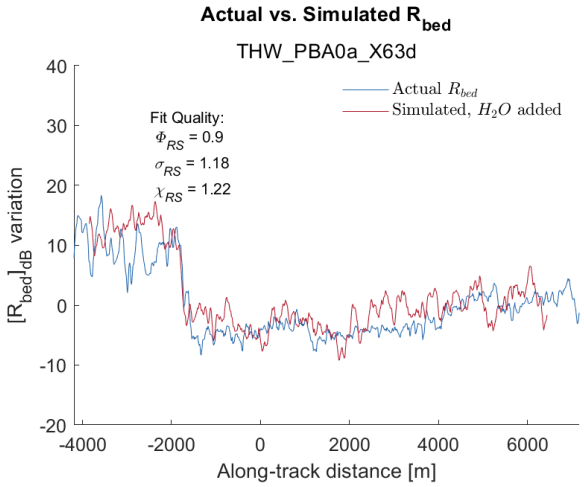


Figure C21: Simulated segment 12, R_{bed} vs. $R_{bed,S}$ comparison

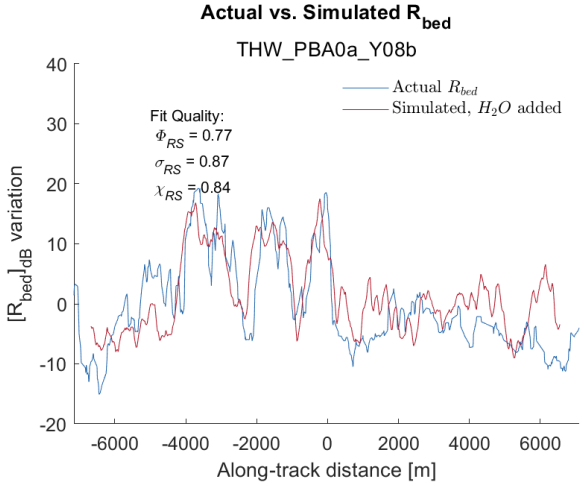


Figure C22: Simulated segment 13, R_{bed} vs. $R_{bed,S}$ comparison

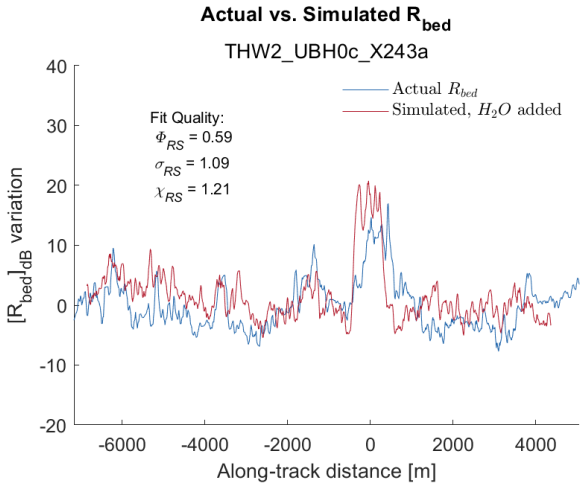


Figure C23: Simulated segment 14, R_{bed} vs. $R_{bed,S}$ comparison

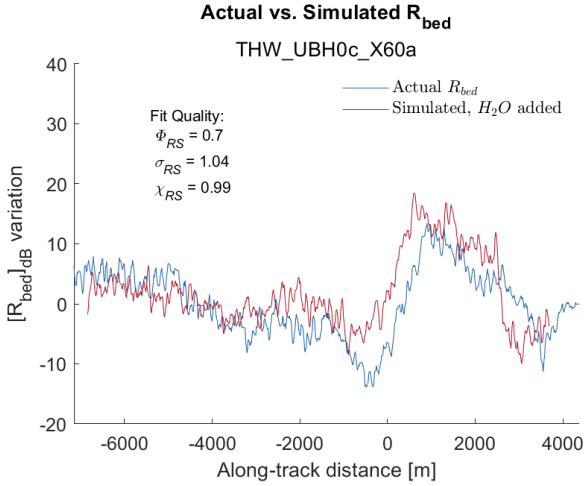


Figure C24: Simulated segment 15, R_{bed} vs. $R_{bed,S}$ comparison

Appendix C - Substrate Transition Fits

This appendix contains along-track relative reflectivity comparisons (R_{bed} vs. $R_{bed,S}$) and fit quality metrics for all simulated segments identified as substrate transitions in the text. Simulation segment numbers correspond to locations on Fig. C8.

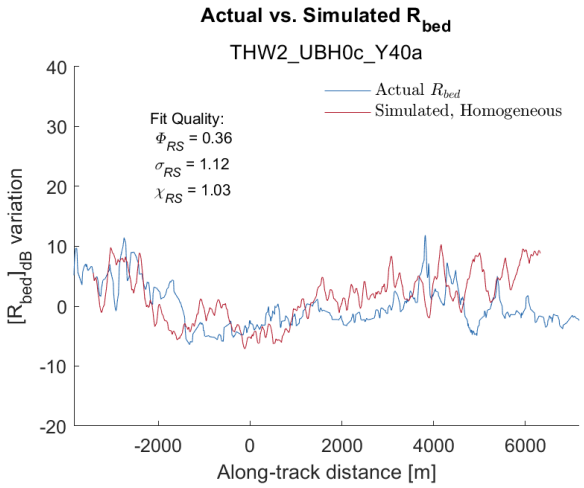


Figure C25: Simulated segment 16, R_{bed} vs. $R_{bed,S}$ comparison

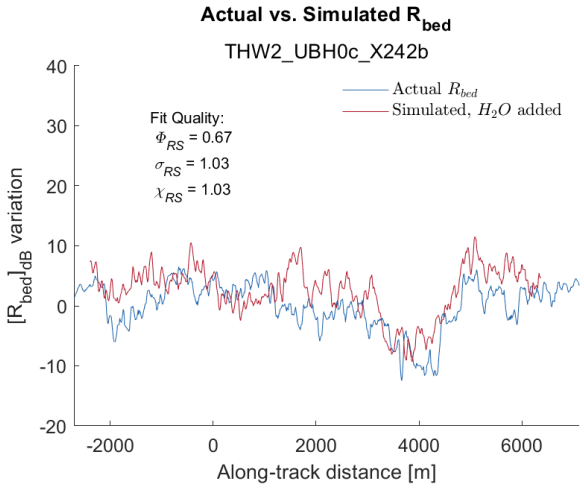


Figure C26: Simulated segment 17, R_{bed} vs. $R_{bed,S}$ comparison

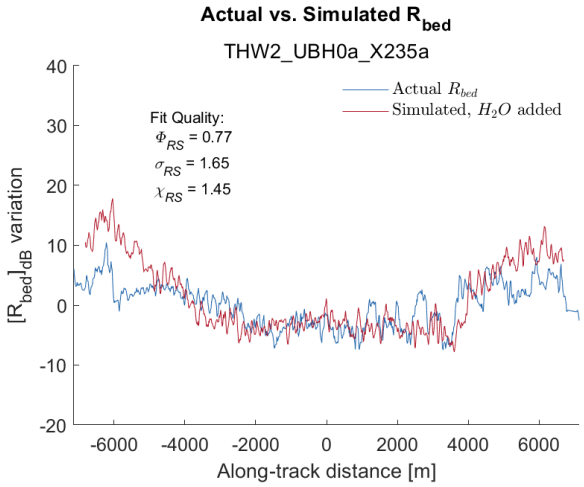


Figure C27: Simulated segment 18, R_{bed} vs. $R_{bed,S}$ comparison

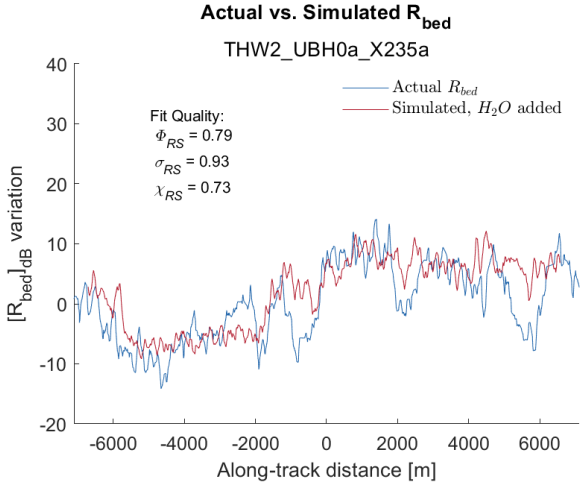


Figure C28: Simulated segment 19, R_{bed} vs. $R_{bed,S}$ comparison

Appendix D - Heterogeneous Fits

This appendix contains along-track relative reflectivity comparisons (R_{bed} vs. $R_{bed,S}$) and fit quality metrics for all simulated segments identified as heterogeneous in the text. Simulation segment numbers correspond to locations on Fig. C8.

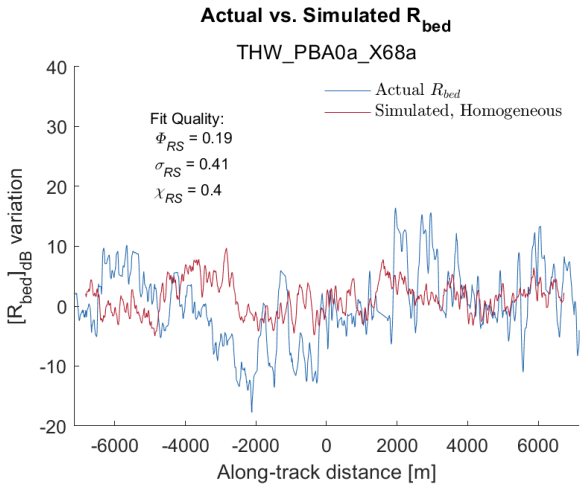


Figure C29: Simulated segment 20, R_{bed} vs. $R_{bed,S}$ comparison

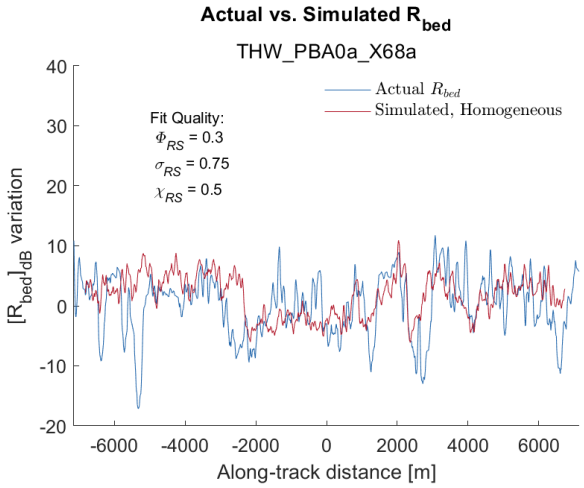


Figure C30: Simulated segment 21, R_{bed} vs. $R_{bed,S}$ comparison

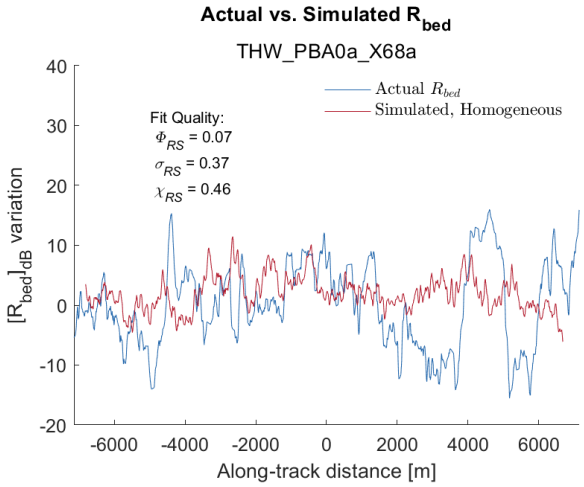


Figure C31: Simulated segment 22, R_{bed} vs. $R_{bed,S}$ comparison

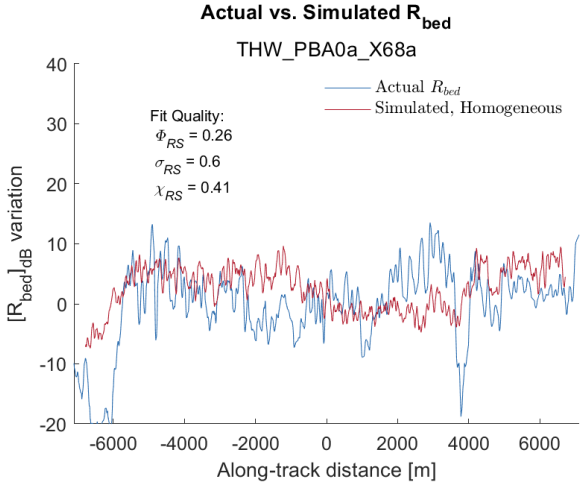


Figure C32: Simulated segment 23, R_{bed} vs. $R_{bed,S}$ comparison

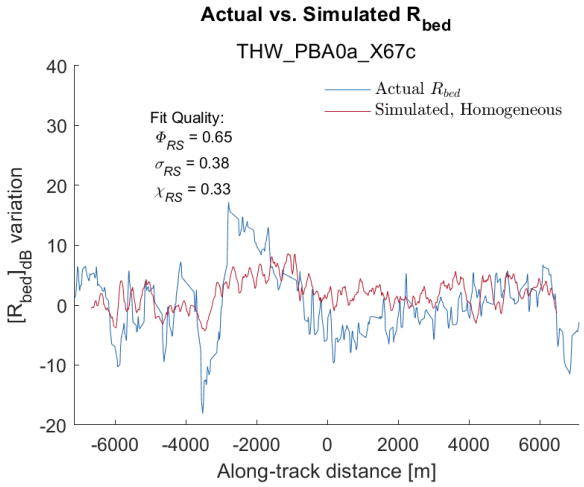


Figure C33: Simulated segment 24, R_{bed} vs. $R_{bed,S}$ comparison

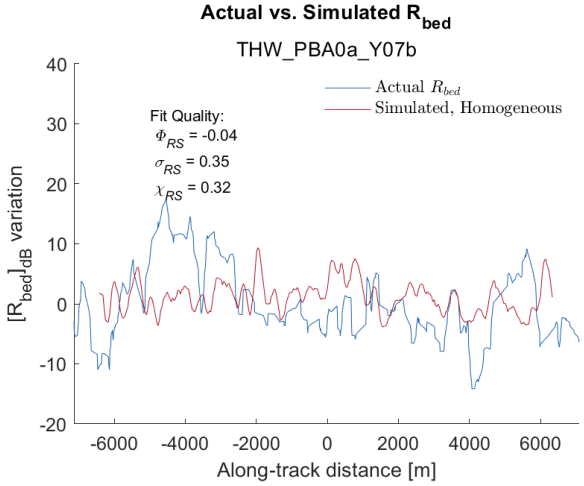


Figure C34: Simulated segment 25, R_{bed} vs. $R_{bed,S}$ comparison

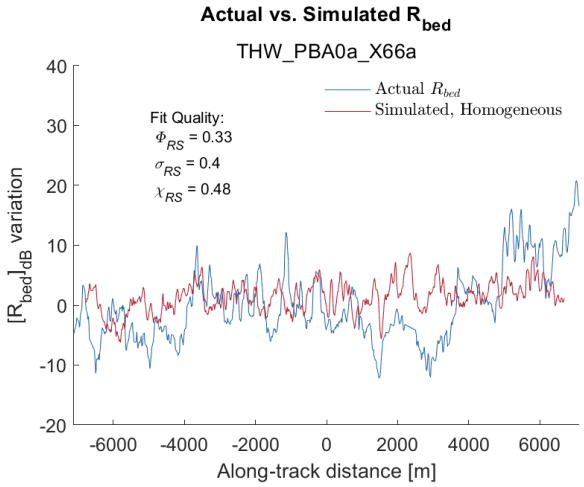


Figure C35: Simulated segment 26, R_{bed} vs. $R_{bed,S}$ comparison

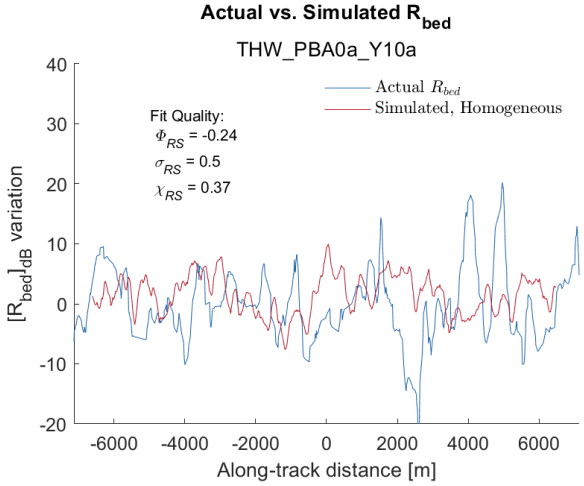


Figure C36: Simulated segment 27, R_{bed} vs. $R_{bed,S}$ comparison

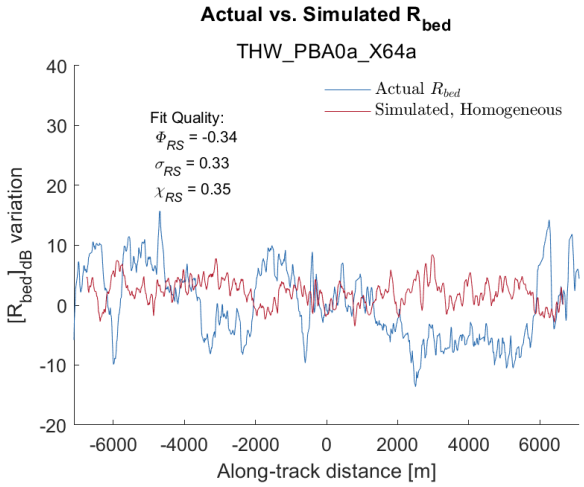


Figure C37: Simulated segment 28, R_{bed} vs. $R_{bed,S}$ comparison

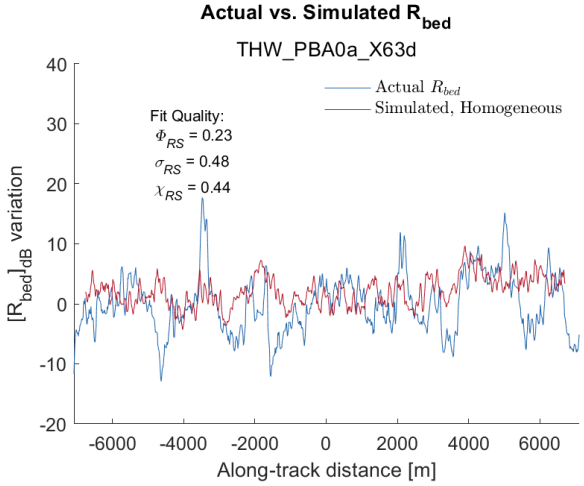


Figure C38: Simulated segment 29, R_{bed} vs. $R_{bed,S}$ comparison

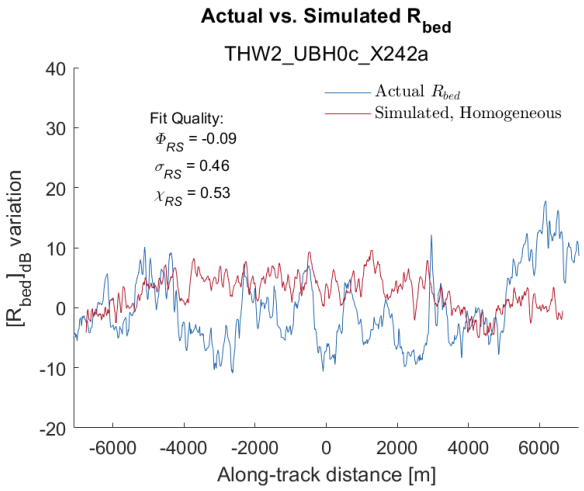


Figure C39: Simulated segment 30, R_{bed} vs. $R_{bed,S}$ comparison

CONCLUSION

This dissertation demonstrates the use of a radar backscattering simulator for interpreting sub-glacial conditions from airborne RES data. Hypothetical simulations confirmed that reflectivity is dependent on both the size and cross-sectional shape of a sub-glacial water structure. We began by evaluating just a single $4km$ segment of RES survey data, then scaled up to analyzing over $400km$. In the process, we provided constraints on the extent and geometry of individual hydrological features, and evaluated potentially contrasting bed conditions across a wide geographic footprint. Given the known ambiguities associated with identifying sub-glacial water using RES, these are promising advances with broad applicability.

The two field sites, Thwaites Glacier in West Antarctica and Devon Ice Cap in Nunavut, Canada are dissimilar geographically and hydrologically, yet several common themes emerge from this work. First, topography alone can induce large reflectivity variations. This result is significant and rarely appreciated in the literature. Most RES analyses correlate elevated R_{bed} as sub-glacial water, yet the work presented here indicates this is overly simplistic in complex terrain. The RES simulation technique may allow researchers to evaluate whether a bright reflector is likely from material contrast at the bed (such as the contrast between water and rock), or a result of a topographic feature alone. Future research should evaluate the need for basal topography corrections in RES analysis.

In several instances, we mention limited information on basal roughness over length scales $\sim \lambda$. Roughness over such short distances may be relatively unimportant glaciologically, however it is relevant to scattering of radar energy. Given the limited data and computational constraints, a very simplistic approach to roughness was presented here. In reality, this topic should be evaluated with greater rigor in future work.

RES has been a reliable and powerful tool in assessing the sub-glacial environment

for decades. This work contributes a potentially significant advancement for interpreting RES data. Greater computational power and algorithm enhancement will enable additional advances by allowing longer and more complex simulations at higher DEM resolutions. I look forward to this method being more widely adopted within the community as a complimentary method with traditional techniques to gain important glaciological insight.

Future Work

The work in this dissertation establishes a methodology that has broad applications beyond the use cases presented here. Perhaps the highest leverage opportunity will be creating a user friendly and more computationally efficient version of the radar sounding simulator software for distribution within the glaciological community. There is a previous iteration available [26], however the work in this thesis represents multiple functionality improvements specific to ice penetrating RES studies. Greater computational efficiency could allow more complex simulations, such as investigations of specularity content. Investing time in this work could catalyze the efforts of many researchers within the community and advance our understanding of radar science in a glaciological context.

This document notes the absence of a comprehensive treatment for sub-glacial roughness and its impact on RES reflectivity. This is a critical gap in our interpretation of RES data. Future simulation studies can help calibrate radar sensitivity to roughness over length scales ranging from less than λ to many km.

Finally, the simulation methods presented here will be useful in studying icy worlds of distant planets within our solar system. NASA will perform radar surveys of Jupiter's ice-covered moon Europa within the next decade. The ocean beneath Europa's vast ice shell is considered one of the most likely habitats for extra-terrestrial life in our solar system. Modeling radar reflectivity from an array of possible surface and basal configurations will be useful to constraining the physical interpretation of actual radar returns from this mission.

REFERENCES CITED

[1] Jessica A. Badgeley, Erin C. Pettit, Christina G. Carr, Slawek Tulaczyk, Jill A. Mikucki, and W. Berry Lyons. An englacial hydrologic system of brine within a cold glacier: Blood falls, mcmurdo dry valleys, antarctica. *Journal of Glaciology*, 63:387–400, 2017. ISSN 00221430. doi: 10.1017/jog.2017.16.

[2] Lucas H. Beem, Ken C. Jezek, and C. J. Van Der Veen. Basal melt rates beneath Whillans Ice Stream, West Antarctica. *Journal of Glaciology*, 56(198):647–654, 2010. ISSN 00221430. doi: 10.3189/002214310793146241.

[3] R. Bindschadler, H. Choi, A. Wichlacz, R. Bingham, J. Bohlander, K. Brunt, H. Corr, R. Drews, H. Fricker, M. Hall, R. Hindmarsh, J. Kohler, L. Padman, W. Rack, G. Rotschky, S. Urbini, P. Vornberger, and N. Young. Getting around Antarctica: New high-resolution mappings of the grounded and freely-floating boundaries of the Antarctic ice sheet created for the International Polar Year. *The Cryosphere*, 5:569–588, 2011. ISSN 19940416. doi: 10.5194/tc-5-569-2011.

[4] Robert G Bingham and Martin J Siegert. Quantifying subglacial bed roughness in Antarctica : implications for ice-sheet dynamics and history. *Quaternary Science Reviews*, 28:223–236, 2009. doi: 10.1016/j.quascirev.2008.10.014.

[5] D. D. Blankenship, D. L. Morse, C. A. Finn, R. E. Bell, M. E. Peters, S. D. Kempf, S. M. Hodge, M. Studinger, J. C. Behrendt, and J. M. Brozena. Geologic controls on the initiation of rapid basal motion for west antarctic ice streams: A geophysical perspective including new airborne radar sounding and laser altimetry results. *The West Antarctic Ice Sheet: Behavior and Environment*, pages 105–121, 2001. doi: https://doi.org/10.1029/AR077p0105. URL `https://agupubs.onlinelibrary.wiley.com/doi/abs/10.1029/AR077p0105`.

[6] G.E.P. Box, J.S. Hunter, and W.G. Hunter. *Statistics for experimenters: an introduction to design, data analysis, and model building*. John Wiley and Sons, Inc., 1978.

[7] Douglas Brinkerhoff, Andy Aschwanden, and Mark Fahnestock. Constraining subglacial processes from surface velocity observations using surrogate-based Bayesian inference. *Journal of Glaciology*, 67(263):385–403, 2021. ISSN 00221430. doi: 10.1017/jog.2020.112.

[8] A. M. Le Brocq, A. J. Payne, M. J. Siegert, and R. B. Alley. A subglacial water-flow model for west antarctica. *Journal of Glaciology*, 55:879–888, 2009. ISSN 00221430. doi: 10.3189/002214309790152564.

[9] Sasha P. Carter, Donald D. Blankenship, Matthew E. Peters, Duncan A. Young, John W. Holt, and David L. Morse. Radar-based subglacial lake classification in Antarctica. *Geochemistry, Geophysics, Geosystems*, 8(3), 2007. ISSN 15252027. doi: 10.1029/2006GC001408.

[10] Davide Castelletti, Dustin M Schroeder, Scott Hensley, Cyril Grima, Gregory Ng, Duncan Young, Yonggyu Gim, Lorenzo Bruzzone, Alina Moussessian, and Don D Blankenship. An Interferometric Approach to Cross-Track Clutter Detection in Two-Channel VHF Radar Sounders. *IEEE Transactions on Geoscience and Remote Sensing*, 55(11):6128–6140, 2017. doi: 10.1109/TGRS.2017.2721433.

[11] Knut Christianson, Robert W. Jacobel, Huw J. Horgan, Richard B. Alley, Sridhar Anandakrishnan, David M. Holland, and Kevin J. DallaSanta. Basal conditions at the grounding zone of Whillans Ice Stream, West Antarctica, from ice-penetrating radar. *Journal of Geophysical Research: Earth Surface*, 121(11):1954–1983, 2016. ISSN 21699011. doi: 10.1002/2015JF003806.

[12] Brent C. Christner, John C. Priscu, Amanda M. Achberger, Carlo Barbante, Sasha P. Carter, Knut Christianson, Alexander B. Michaud, Jill A. Mikucki, Andrew C. Mitchell, Mark L. Skidmore, Trista J. Vick-Majors, W. P. Adkins, S. Anandakrishnan, S. Anandakrishnan, L. Beem, A. Behar, M. Beitch, R. Bolsey, C. Branecky, A. Fisher, N. Foley, K. D. Mankoff, D. Sampson, S. Tulaczyk, R. Edwards, S. Kelley, J. Sherve, H. A. Fricker, S. Siegfried, B. Guthrie, Timothy Hodson, R. Powell, R. Scherer, H. Horgan, R. Jacobel, E. McBryan, and A. Purcell. A microbial ecosystem beneath the west antarctic ice sheet. *Nature*, 512:310–313, 8 2014. ISSN 14764687. doi: 10.1038/nature13667.

[13] Winnie Chu, Dustin M. Schroeder, Helene Seroussi, Timothy T. Creyts, Steven J. Palmer, and Robin E. Bell. Extensive winter subglacial water storage beneath the Greenland Ice Sheet. *Geophysical Research Letters*, 43(24):12,484–12,492, 2016. ISSN 19448007. doi: 10.1002/2016GL071538.

[14] Christopher F Chyba and Cynthia B Phillips. Europa As an Abode of Life. *Origin of Life and Evolution of the Biosphere*, 32:47–67, 2002. doi: https://doi.org/10.1023/A:1013958519734. URL `https://link.springer.com/content/pdf/10.1023/A:1013958519734.pdf`.

[15] Timothy T. Creyts and Christian G. Schoof. Drainage through subglacial water sheets. *Journal of Geophysical Research: Earth Surface*, 114(4):1–18, 2009. ISSN 21699011. doi: 10.1029/2008JF001215.

[16] Ian Cumming and Frank Wong. *Digital Processing of Synthetic Aperture Radar: Algorithms and Implementation*. Artech House, Norwood, MA, 2005. ISBN 978-1-58053-058-3.

[17] C. F. Dow, F. S. McCormack, D. A. Young, J. S. Greenbaum, J. L. Roberts, and D. D. Blankenship. Totten Glacier subglacial hydrology determined from geophysics and modeling. *Earth and Planetary Science Letters*, 531:115961, 2020. ISSN 0012821X. doi: 10.1016/j.epsl.2019.115961. URL `https://doi.org/10.1016/j.epsl.2019.115961`.

[18] J A Dowdeswell, T J Benham, M R Gorman, D Burgess, and M J Sharp. Form and flow of the Devon Island Ice Cap , Canadian Arctic. *Journal of Geophysical Research: Earth Surface*, 109(F2):1–14, 2004. doi: 10.1029/2003JF000095.

[19] T. Dunse, T. Schellenberger, J. O. Hagen, A. Kääb, T. V. Schuler, and C. H. Reijmer. Glacier-surge mechanisms promoted by a hydro-thermodynamic feedback to summer melt. *Cryosphere*, 9(1):197–215, 2015. ISSN 19940424. doi: 10.5194/tc-9-197-2015.

[20] Hermann Engelhardt and Barclay Kamb. Basal hydraulic system of a West Antarctic ice stream: constraints from borehole observations. *Journal of Glaciology*, 43:207–230, 1997. ISSN 0022-1430. doi: DOI:10.3189/S0022143000003166. URL `https://www.cambridge.org/core/product/C62FA516ED8202DAA1CE8C6320B735AA`.

[21] T. Flament, E. Berthier, and F. Rémy. Cascading water underneath Wilkes Land, East Antarctic ice sheet, observed using altimetry and digital elevation models. *Cryosphere*, 8(2):673–687, 2014. ISSN 19940424. doi: 10.5194/tc-8-673-2014.

[22] Shuji Fujita, Takeshi Matsuoka, Toshihiro Ishida, Kenichi Matsuoka, and Shinji Mae. A summary of the complex dielectric permittivity of ice in the megahertz range and its applications for radar sounding of polar ice sheets. *Physics of Ice Core Records*, pages 185–212, 2000.

[23] Alex S. Gardner, Martin J. Sharp, Roy M. Koerner, Claude Labine, Sarah Boon, Shawn J. Marshall, David O. Burgess, and David Lewis. Near-surface temperature lapse rates over arctic glaciers and their implications for temperature downscaling. *Journal of Climate*, 22(16):4281–4298, 2009. ISSN 08948755. doi: 10.1175/2009JCLI2845.1.

[24] C Gerekos, M S Haynes, D M Schroeder, and D D Blankenship. The Phase Response of a Rough Rectangular Facet for Radar Sounder Simulations of Both Coherent and Incoherent Scattering. *Radio Science*, 58:1–30, 2023. doi: 10.1029/2022RS007594.

[25] Christopher Gerekos. *Advanced Backscattering Simulation Methods for the Design of Spaceborne Radar Sounders*. PhD thesis, Universita Degli Studi di Trento, 2020.

[26] Christopher Gerekos, Alessandro Tamponi, Leonardo Carrer, Davide Castelletti, Massimo Santoni, and Lorenzo Bruzzone. A coherent multilayer simulator of radargrams acquired by radar sounder instruments. *IEEE Transactions on Geoscience and Remote Sensing*, 56(12):7388–7404, 2018. ISSN 01962892. doi: 10.1109/TGRS.2018.2851020.

[27] Christopher Gerekos, Lorenzo Bruzzone, and Masafumi Imai. A Coherent Method for Simulating Active and Passive Radar Sounding of the Jovian Icy Moons. *IEEE Transactions on Geoscience and Remote Sensing*, 58(4):2250–2265, 2020. ISSN 15580644. doi: 10.1109/TGRS.2019.2945079.

[28] Adrien Gilbert, Florent Gimbert, Kjetil Thøgersen, Thomas V. Schuler, and Andreas Kääb. A Consistent Framework for Coupling Basal Friction With Subglacial Hydrology on Hard-Bedded Glaciers. *Geophysical Research Letters*, 49(13):1–10, 2022. ISSN 19448007. doi: 10.1029/2021GL097507.

[29] P W J Glover. 11.04 - Geophysical Properties of the Near Surface Earth: Electrical Properties. In Gerald Schubert, editor, *Treatise on Geophysics (Second Edition)*, pages 89–137. Elsevier, Oxford, second edi edition, 2015. ISBN 978-0-444-53803-1. doi: https://doi.org/10.1016/B978-0-444-53802-4.00189-5. URL https://www.sciencedirect.com/science/article/pii/B9780444538024001895.

[30] S Gogineni, T Chuah, C Allen, K Jezek, and R. K. Moore. Instruments and Methods: An improved coherent radar depth sounder. *Journal of Glaciology*, 44(148):659–669, 1998. URL https://www.cambridge.org/core/services/aop-cambridge-core/content/view/50CA9A53DF383F80E01E7312B805615B/S0022143000002161a.pdf/an_improved_coherent_radar_depth_sounder.pdf.

[31] Alexander O. Hager, Matthew J. Hoffman, Stephen F. Price, and Dustin M. Schroeder. Persistent, extensive channelized drainage modeled beneath Thwaites Glacier, West Antarctica. *Cryosphere*, 16(9):3575–3599, 2022. ISSN 19940424. doi: 10.5194/tc-16-3575-2022.

[32] Mark S. Haynes. Surface and subsurface radar equations for radar sounders. *Annals of Glaciology*, 61(81):135–142, 2020. ISSN 02603055. doi: 10.1017/aog.2020.16.

[33] Mark S. Haynes, Elaine Chapin, and Dustin M. Schroeder. Geometric power fall-off in radar sounding. *IEEE Transactions on Geoscience and Remote Sensing*, 56:6571–6585, 2018. ISSN 01962892. doi: 10.1109/TGRS.2018.2840511.

[34] Florence Hélière, Chung Chi Lin, Hugh Corr, and David Vaughan. Radio echo sounding of Pine Island Glacier, West Antarctica: Aperture synthesis processing and analysis of feasibility from space. *IEEE Transactions on Geoscience and Remote Sensing*, 45(8):2573–2582, 2007. ISSN 01962892. doi: 10.1109/TGRS.2007.897433.

[35] Andrew O Hoffman, Knut Christianson, Nicholas Holschuh, Elizabeth Case, Jonathan Kingslake, and Robert Arthern. The Impact of Basal Roughness on Inland Thwaites Glacier Sliding. *Geophysical Research Letters*, 49(14):1–11, 2022. doi: 10.1029/2021GL096564.

[36] Matthew J. Hoffman, Lauren C. Andrews, Stephen A. Price, Ginny A. Catania, Thomas A. Neumann, Martin P. Lüthi, Jason Gulley, Claudia Ryser, Robert L. Hawley, and Blaine Morriss. Greenland subglacial drainage evolution regulated by weakly connected regions of the bed. *Nature Communications*, 7, 2016. ISSN 20411723. doi: 10.1038/ncomms13903.

[37] John W. Holt, Donald D. Blankenship, David L. Morse, Duncan A. Young, Matthew E. Peters, Scott D. Kempf, Thomas G. Richter, David G. Vaughan, and Hugh F.J. Corr. New boundary conditions for the west antarctic ice sheet: Subglacial topography of the thwaites and smith glacier catchments. *Geophysical Research Letters*, 33, 5 2006. ISSN 00948276. doi: 10.1029/2005GL025561.

[38] Bryn Hubbard, Martin J Siegert, and Danny Mccarroll. Spectral roughness of glaciated bedrock geomorphic surfaces : Implications for glacier sliding. *Journal of Geophysical Research*, 105(B9):21295–21303, 2000.

[39] Tristram D L Irvine-Fynn, Andrew J Hodson, Brian J Moorman, Geir Vatne, and Alun L Hubbard. Polythermal Glacier Hydrology: A Review. *Reviews of Geophysics*, (2010):1–37, 2011. doi: 10.1029/2010RG000350.1.INTRODUCTION.

[40] Robert W Jacobel, Brian C Welch, David Osterhouse, Rickard Pettersson, and Joseph A Macgregor. Spatial variation of radar-derived basal conditions on Kamb Ice Stream, West Antarctica. *Annals of Glaciology*, 50(51):10–16, 2009. ISSN 02603055. doi: 10.3189/172756409789097504.

[41] Stewart S.R. Jamieson, Neil Ross, Jamin S. Greenbaum, Duncan A. Young, Alan R.A. Aitken, Jason L. Roberts, Donald D. Blankenship, Sun Bo, and Martin J. Siegert. An extensive subglacial lake and canyon system in Princess Elizabeth Land, East Antarctica. *Geology*, 44(2):87–90, 2016. ISSN 19432682. doi: 10.1130/G37220.1.

[42] Ian Joughin, Benjamin E Smith, and Brooke Medley. Marine Ice Sheet Collapse Potentially Under Way for the Thwaites Glacier Basin, West Antarctica. *Science*, 344(May):735–739, 2014.

[43] J Jouzel, J R Petit, R Souchez, N I Barkov, V Ya. Lipenkov, D Raynaud, M Stievenard, N I Vassiliev, V Verbeke, and F Vimeux. More than 200 meters of lake ice above subglacial lake vostok, antarctica. *Science*, 286:2138–2141, 1999. doi: 10.1126/science.286.5447.2138. URL `https://www.science.org/doi/abs/10.1126/science.286.5447.2138`.

[44] Siobhan F Killingbeck, Christine F Dow, and Martyn J Unsworth. A quantitative method for deriving salinity of subglacial water using ground-based transient electromagnetics. *Journal of Glaciology*, 68(268):319–336, 2022.

[45] Siobhan F Killingbeck, Anja Rutishauser, Martyn J Unsworth, Ashley Dubnick, S Alison, James Killingbeck, Christine F Dow, Tim Hill, Adam D Booth, and Brittany Main. Misidentified subglacial lake beneath the devon ice cap , canadian arctic : A new interpretation from seismic and electromagnetic data. *EGUSphere*, [preprint]: 1–36, 2024. doi: 10.5194/egusphere-2024-279.

[46] Arthur H. Lachenbruch. Rapid Estimation of the Topographic Disturbance to Superficial Thermal Gradients. *Reviews of Geophysics*, 6(3):365–399, 1968.

[47] Charles H. Lees. On the Shapes of the Isogeotherms Under Mountain Ranges in Radioactive Districts. *Proceedings of the Royal Society of London. Series A, Containing Papers of a Mathematical and Physical Character*, 83(563):339–346, 1910. ISSN 0950-1207. doi: 10.1098/rspa.1910.0022.

[48] Laura E. Lindzey, Lucas H. Beem, Duncan A. Young, Enrica Quartini, Donald D. Blankenship, Choon Ki Lee, Won Sang Lee, Jong Ik Lee, and Joohan Lee. Aerogeophysical characterization of an active subglacial lake system in the David Glacier catchment, Antarctica. *Cryosphere*, 14(7):2217–2233, 2020. ISSN 19940424. doi: 10.5194/tc-14-2217-2020.

[49] J.A. MacGregor, G.A. Catania, H. Conway, D.M. Schroeder, I. Joughin, D.A. Young, S.D. Kempf, and D.A. Blankenship. Weak bed control of the eastern shear margin of thwaites glacier, west antarctica. *Journal of Glaciology*, 59:900–912, 2013.

[50] Douglas Mair, David Burgess, and Martin Sharp. Thirty-seven year mass balance of Devon Ice Cap, Nunavut, Canada, determined by shallow ice coring and melt modeling. *Journal of Geophysical Research: Earth Surface*, 110(1):1–13, 2005. ISSN 21699011. doi: 10.1029/2003JF000099.

[51] G. Malczyk, N. Gourmelen, D. Goldberg, J. Wuite, and T. Nagler. Repeat Subglacial Lake Drainage and Filling Beneath Thwaites Glacier. *Geophysical Research Letters*, 47(23), 2020. ISSN 19448007. doi: 10.1029/2020GL089658.

[52] K. Matsuoka, A. Skoglund, and G. Roth. Quantarctica [data set], 2018.

[53] Kenichi Matsuoka, Joseph A. MacGregor, and Frank Pattyn. Predicting radar attenuation within the Antarctic ice sheet. *Earth and Planetary Science Letters*, 359-360:173–183, 2012. ISSN 0012821X. doi: 10.1016/j.epsl.2012.10.018. URL `http://dx.doi.org/10.1016/j.epsl.2012.10.018`.

[54] Nur Shahida Midi, Kaito Sasaki, Ryu-ichiro Ohyama, and Naoki Shinyashiki. Broadband complex dielectric constants of water and sodium chloride aqueous solutions with different DC conductivities. *IEEJ Transactions on Electrical and Electronic Engineering*, 9(S1):S8–S12, 2014. ISSN 19314981. doi: 10.1002/tee.22036.

[55] B. W.J. Miles, C. R. Stokes, A. Jenkins, J. R. Jordan, S. S.R. Jamieson, and G. H. Gudmundsson. Intermittent structural weakening and acceleration of the thwaites glacier tongue between 2000 and 2018. *Journal of Glaciology*, 66:485–495, 6 2020. ISSN 00221430. doi: 10.1017/jog.2020.20.

[56] M. Morlighem. MEaSUREs BedMachine Antarctica, Version 2, 2020.

[57] J. Mouginot, E. Rignot, and B. Scheuchl. Sustained increase in ice discharge from the Amundsen Sea Embayment, West Antarctica, from 1973 to 2013. *Geophysical Research Letters*, 41(5):1576–1584, 2014. ISSN 19448007. doi: 10.1002/2013GL059069.

[58] T. Murray, H. Corr, A. Forieri, and A. M. Smith. Contrasts in hydrology between regions of basal deformation and sliding beneath Rutford Ice Stream, West Antarctica, mapped using radar and seismic data. *Geophysical Research Letters*, 35(12):1–5, 2008. ISSN 00948276. doi: 10.1029/2008GL033681.

[59] C. S. Neal. The dynamics of the Ross Ice Shelf revealed by radio echo- sounding. *Journal of Glaciology*, 24(90):295–307, 1979. ISSN 00221430. doi: 10.1017/S0022143000014817.

[60] T. A. Neumann, A. Brenner, D. W. Hancock III, J. Robbins, A. Gibbons, J. Lee, K. Harbeck, J. Saba, S. Luthcke, and T. Rebold. Atlas/icesat-2 l2a global geolocated photon data, version 6, 2023.

[61] T. L. Noble, E. J. Rohling, A. R.A. Aitken, H. C. Bostock, Z. Chase, N. Gomez, L. M. Jong, M. A. King, A. N. Mackintosh, F. S. McCormack, R. M. McKay, L. Menviel, S. J. Phipps, M. E. Weber, C. J. Fogwill, B. Gayen, N. R. Golledge, D. E. Gwyther, A. Mc C. Hogg, Y. M. Martos, B. Pena-Molino, J. Roberts, T. van de Flierdt, and T. Williams. The Sensitivity of the Antarctic Ice Sheet to a Changing Climate: Past, Present, and Future. *Reviews of Geophysics*, 58(4):1–89, 2020. ISSN 19449208. doi: 10.1029/2019RG000663.

[62] A V Okulitch. Geology of the Canadian Arctic Archipelago, Northwest Territories and North Greenland, 1991.

[63] W.S.B. PATERSON. *The Physics of Glaciers*. Elsevier Ltd, 3rd editio edition, 1994. ISBN 978-0-08-037944-9.

[64] Leo E. Peters, Sridhar Anandakrishnan, Richard B. Alley, J. Paul Winberry, Donald E. Voigt, Andrew M. Smith, and David L. Morse. Subglacial sediments as a control on the onset and location of two siple coast ice streams, west antarctica. *Journal of Geophysical Research: Solid Earth*, 111, 1 2006. ISSN 21699356. doi: 10.1029/2005JB003766.

[65] Matthew E. Peters, Donald D. Blankenship, and David L. Morse. Analysis techniques for coherent airborne radar sounding: Application to West Antarctic ice streams. *Journal of Geophysical Research: Solid Earth*, 110(6):1–17, 2005. ISSN 21699356. doi: 10.1029/2004JB003222.

[66] Matthew E. Peters, Donald D. Blankenship, Sasha P. Carter, Scott D. Kempf, Duncan A. Young, and John W. Holt. Along-track focusing of airborne radar sounding data from west antarctica for improving basal reflection analysis and layer detection. *IEEE Transactions on Geoscience and Remote Sensing*, 45(9):2725–2736, 2007. ISSN 01962892. doi: 10.1109/TGRS.2007.897416.

[67] C Pierce, C Gerekos, M Skidmore, L Beem, D Blankenship, W S Lee, E Adams, C.-K. Lee, and J Stutz. Characterizing sub-glacial hydrology using radar simulations.

The Cryosphere, 18(4):1495–1515, 2024. doi: 10.5194/tc-18-1495-2024. URL https://tc.copernicus.org/articles/18/1495/2024/.

[68] Chris Pierce, Mark Skidmore, Lucas Beem, Don Blankenship, Ed Adams, and Christopher Gerekos. Exploring canyons beneath devon ice cap for sub-glacial drainage using radar and thermodynamic modeling (accepted). *Journal of Glaciology*, 2024.

[69] Claire Porter, Paul Morin, Ian Howat, Myoung-Jon Noh, Brian Bates, Kenneth Peterman, Scott Keesey, Matthew Schlenk, Judith Gardiner, Karen Tomko, Michael Willis, Cole Kelleher, Michael Cloutier, Eric Husby, Steven Foga, Hitomi Nakamura, Melisa Platson, Michael Wethington, Cathleen Williamson, Gregory Bauer, Jeremy Enos, Galen Arnold, William Kramer, Peter Becker, Abhijit Doshi, Cristelle D'Souza, Pat Cummens, Fabien Laurier, and Mikkel Bojesen. ArcticDEM, 2018.

[70] John C Priscu, Craig F Wolf, Cristina D Takacs, Christian H Fritsen, Johanna Laybourn-Parry, Emily C Roberts, Birgit Sattler, and W. Berry Lyons. Carbon transformations in a perennially ice-covered antarctic lake. *BioScience*, 49:997–1008, 1999. doi: https://doi.org/10.1525/bisi.1999.49.12.997.

[71] John C. Priscu, Jonas Kalin, John Winans, Timothy Campbell, Matthew R. Siegfried, Mark Skidmore, John E. Dore, Amy Leventer, David M. Harwood, Dennis Duling, Robert Zook, Justin Burnett, Dar Gibson, Edward Krula, Anatoly Mironov, Jim McManis, Graham Roberts, Brad E. Rosenheim, Brent C. Christner, Kathy Kasic, Helen A. Fricker, W. Berry Lyons, Joel Barker, Mark Bowling, Billy Collins, Christina Davis, Al Gagnon, Christopher Gardner, Chloe Gustafson, Ok Sun Kim, Wei Li, Alex Michaud, Molly O. Patterson, Martyn Tranter, Ryan Venturelli, Trista Vick-Majors, and Cooper Elsworth. Scientific access into Mercer Subglacial Lake: Scientific objectives, drilling operations and initial observations. *Annals of Glaciology*, 62(85-86): 340–352, 2021. ISSN 02603055. doi: 10.1017/aog.2021.10.

[72] E. Rignot, J. Mouginot, M. Morlighem, H. Seroussi, and B. Scheuchl. Widespread, rapid grounding line retreat of Pine Island, Thwaites, Smith, and Kohler glaciers, West Antarctica, from 1992 to 2011. *Geophysical Research Letters*, 41(10):3502–3509, 2014. ISSN 19448007. doi: 10.1002/2014GL060140.

[73] E. Rignot, J. Mouginot, and B. Scheuchl. Measures insar-based antarctica ice velocity map, version 2, 2017. URL https://nsidc.org/data/NSIDC-0484/versions/2.

[74] Eric Rignot, Jérémie Mouginot, Bernd Scheuchl, Michiel Van Den Broeke, Melchior J. Van Wessem, and Mathieu Morlighem. Four decades of Antarctic ice sheet mass balance from 1979–2017. *Proceedings of the National Academy of Sciences of the United States of America*, 116(4):1095–1103, 2019. ISSN 10916490. doi: 10.1073/pnas.1812883116.

[75] D. M. Rippin, D. G. Vaughan, and H. F.J. Corr. The basal roughness of Pine Island Glacier, West Antarctica. *Journal of Glaciology*, 57(201):67–76, 2011. ISSN 00221430. doi: 10.3189/002214311795306574.

[76] Hans Röthlisberger. Water Pressure in Intra- and Subglacial Channels. *Journal of Glaciology*, 11(62):177–203, 1972. ISSN 0022-1430. doi: 10.3189/s0022143000022188.

[77] Federica Russo, Marco Cutigni, Roberto Orosei, Cario Taddei, Roberto Seu, Daniela Biccari, Emanuele Giacomoni, Oreste Fuga, and Enrico Flamini. An Incoherent Simulator for the Sharad Experiment. *2008 IEEE Radar Conference, RADAR 2008*, 2008. doi: 10.1109/RADAR.2008.4720761.

[78] Anja Rutishauser, Donald D. Blankenship, Martin Sharp, Mark L. Skidmore, Jamin S. Greenbaum, Cyril Grima, Dustin M. Schroeder, Julian A. Dowdeswell, and Duncan A. Young. Discovery of a hypersaline subglacial lake complex beneath Devon Ice Cap, Canadian Arctic. *Science Advances*, 4(4):1–7, 2018. ISSN 23752548. doi: 10.1126/sciadv.aar4353.

[79] Anja Rutishauser, Donald D. Blankenship, Duncan A. Young, Natalie A. Wolfenbarger, Lucas H. Beem, Mark L. Skidmore, Ashley Dubnick, and Alison S Criscitiello. Widespread brine network and lake system beneath Devon Ice Cap expands potential subglacial microbial habitat. *Proceedings of the National Academy of Sciences*, pages 1–19, 2021.

[80] Anja Rutishauser, Donald D. Blankenship, Duncan A. Young, Natalie S. Wolfenbarger, Lucas H. Beem, Mark L. Skidmore, Ashley Dubnick, and Alison S. Criscitiello. Radar sounding survey over Devon Ice Cap indicates the potential for a diverse hypersaline subglacial hydrological environment. *Cryosphere*, 16(2):379–395, 2022. ISSN 19940424. doi: 10.5194/tc-16-379-2022.

[81] T. A. Scambos, R. E. Bell, R. B. Alley, S. Anandakrishnan, D. H. Bromwich, K. Brunt, K. Christianson, T. Creyts, S. B. Das, R. DeConto, P. Dutrieux, H. A. Fricker, D. Holland, J. MacGregor, B. Medley, J. P. Nicolas, D. Pollard, M. R. Siegfried, A. M. Smith, E. J. Steig, L. D. Trusel, D. G. Vaughan, and P. L. Yager. How much, how fast?: A science review and outlook for research on the instability of Antarctica's Thwaites Glacier in the 21st century. *Global and Planetary Change*, 153(April):16–34, 2017. ISSN 09218181. doi: 10.1016/j.gloplacha.2017.04.008. URL `http://dx.doi.org/10.1016/j.gloplacha.2017.04.008`.

[82] Kirk M. Scanlan, Anja Rutishauser, Duncan A. Young, and Donald D. Blankenship. Interferometric discrimination of cross-track bed clutter in ice-penetrating radar sounding data. *Annals of Glaciology*, 61(81):68–73, 2020. ISSN 02603055. doi: 10.1017/aog.2020.20.

[83] Dustin M. Schroeder, Donald D. Blankenship, and Duncan A. Young. Evidence for a water system transition beneath thwaites glacier, West Antarctica. *Proceedings of the*

National Academy of Sciences of the United States of America, 110(30):12225–12228, 2013. ISSN 00278424. doi: 10.1073/pnas.1302828110.

[84] Dustin M. Schroeder, Donald D. Blankenship, R. Keith Raney, and Cyril Grima. Estimating subglacial water geometry using radar bed echo specularity: Application to Thwaites Glacier, West Antarctica. *IEEE Geoscience and Remote Sensing Letters*, 12(3):443–447, 2015. ISSN 1545598X. doi: 10.1109/LGRS.2014.2337878.

[85] Dustin M. Schroeder, Cyril Grima, and Donald D. Blankenship. Evidence for variable grounding-zone and shear-margin basal conditions across Thwaites Glacier, West Antarctica. *Geophysics*, 81(1):WA35–WA43, 2016. ISSN 19422156. doi: 10.1190/GEO2015-0122.1.

[86] Dustin M. Schroeder, Helene Seroussi, Winnie Chu, and Duncan A. Young. Adaptively constraining radar attenuation and temperature across the Thwaites Glacier catchment using bed echoes. *Journal of Glaciology*, 62(236):1075–1082, 2016. ISSN 00221430. doi: 10.1017/jog.2016.100.

[87] U. Seipold and E. Huenges. Thermal properties of gneisses and amphibolites - high pressure and high temperature investigations of KTB-rock samples. *Tectonophysics*, 291(1-4):173–178, 1998. ISSN 00401951. doi: 10.1016/S0040-1951(98)00038-9.

[88] H. Seroussi, Y. Nakayama, E. Larour, D. Menemenlis, M. Morlighem, E. Rignot, and A. Khazendar. Continued retreat of thwaites glacier, west antarctica, controlled by bed topography and ocean circulation. *Geophysical Research Letters*, 44:6191–6199, 6 2017. ISSN 19448007. doi: 10.1002/2017GL072910.

[89] Sion Shabtaie and Charles R. Bentley. West Antarctic Ice Streams Draining into the Ross Ice Shelf: Configuration and Mass Balance. *Journal of Geophysical Research*, 92 (B2):1311–1336, 1987.

[90] Mark Skidmore, Suzanne P. Anderson, Martin Sharp, Julia Foght, and Brian D. Lanoil. Comparison of microbial community compositions of two subglacial environments reveals a possible role for microbes in chemical weathering processes. *Applied and Environmental Microbiology*, 71(11):6986–6997, 2005. ISSN 00992240. doi: 10.1128/AEM.71.11.6986-6997.2005.

[91] Benjamin E. Smith, Noel Gourmelen, Alexander Huth, and Ian Joughin. Connected subglacial lake drainage beneath Thwaites Glacier, West Antarctica. *Cryosphere*, 11 (1):451–467, 2017. ISSN 19940424. doi: 10.5194/tc-11-451-2017.

[92] M. G. Spagnuolo, F. Grings, P. Perna, M. Franco, H. Karszenbaum, and V. A. Ramos. Multilayer simulations for accurate geological interpretations of SHARAD radargrams. *Planetary and Space Science*, 59(11-12):1222–1230, 2011. ISSN 00320633. doi: 10.1016/j.pss.2010.10.013. URL `http://dx.doi.org/10.1016/j.pss.2010.10.013`.

[93] Rupali Tiwari, Vlastimil Boháč, Peter Dieška, and Gregor Götzl. Thermal properties of limestone rock by pulse transient technique using slab model accounting the heat transfer coefficient and heat capacity of heat source. *AIP Conference Proceedings*, 2305 (February), 2020. ISSN 15517616. doi: 10.1063/5.0033924.

[94] Slawek Tulaczyk, Barclay Kamb, Reed P Scherer, and Hermann F Engelhardt. Sedimentary processes at the base of a west antarctic ice stream; constraints from textural and compositional properties of subglacial debris. *Journal of Sedimentary Research*, 68:487–496, 5 1998. ISSN 1527-1404. doi: 10.2110/jsr.68.487. URL `https://doi.org/10.2110/jsr.68.487`.

[95] Slawek Tulaczyk, W. Barclay Kamb, and Hermann F. Engelhardt. Basal mechanics of Ice Stream B, West Antarctica 2. Undrained plastic bed model. *Journal of Geophysical Research*, 105(1999):483–494, 2000.

[96] Slawek M. Tulaczyk and Neil T. Foley. The role of electrical conductivity in radar wave reflection from glacier beds. *Cryosphere*, 14(12):4495–4506, 2020. ISSN 19940424. doi: 10.5194/tc-14-4495-2020.

[97] USGS. Landsat collection 2 level 2 science products, 2023.

[98] C J van der Veen, T Leftwich, R Von Frese, B M Csatho, and J Li. Subglacial topography and geothermal heat flux : Potential interactions with drainage of the Greenland ice sheet. *Geophysical Research Letters*, 34(June):1–5, 2007. doi: 10.1029/2007GL030046.

[99] Wesley Van Wychen, Luke Copland, Laurence Gray, Dave Burgess, Brad Danielson, and Martin Sharp. Spatial and temporal variation of ice motion and ice flux from Devon Ice Cap, Nunavut, Canada. *Journal of Glaciology*, 58(210):657–664, 2012. ISSN 00221430. doi: 10.3189/2012JoG11J164.

[100] Wesley Van Wychen, Jamie Davis, Luke Copland, David O. Burgess, Laurence Gray, Martin Sharp, Julian A. Dowdeswell, and Toby J. Benham. Variability in ice motion and dynamic discharge from Devon Ice Cap, Nunavut, Canada. *Journal of Glaciology*, 63(239):436–449, 2017. ISSN 00221430. doi: 10.1017/jog.2017.2.

[101] T R Vance, J L Roberts, A D Moy, M A J Curran, C R Tozer, A J E Gallant, N J Abram, T D van Ommen, D A Young, C Grima, D D Blankenship, and M J Siegert. Optimal site selection for a high-resolution ice core record in east antarctica. *Climate of the Past*, 12:595–610, 2016. doi: 10.5194/cp-12-595-2016. URL `https://cp.copernicus.org/articles/12/595/2016/`.

[102] J. S. Walder and A. Fowler. Channelized subglacial drainage over a deformable bed. *Journal of Glaciology*, 40(134):3–15, 1994. ISSN 00221430. doi: 10.1017/S0022143000003750.

[103] Douglas W. Waples and Jacob S. Waples. A review and evaluation of specific heat capacities of rocks, minerals, and subsurface fluids. Part 2: Fluids and porous rocks. *Natural Resources Research*, 13(2):123–130, 2004. ISSN 15207439. doi: 10.1023/B:NARR.0000032648.15016.49.

[104] J. Weertman. The Theory of Glacier Sliding. *Journal of Glaciology*, 5(39):287–303, 1964. ISSN 0022-1430. doi: 10.3189/s0022143000029038.

[105] Simon Willcocks, Derrick Hasterok, and Samuel Jennings. Thermal Refraction: Impactions for Subglacial Heat Flux. *Journal of Glaciology*, 67(265):875–884, 2021. ISSN 18347533. doi: 10.1080/22020586.2019.12072986.

[106] A. P. Wright, D. A. Young, J. L. Roberts, D. M. Schroeder, J. L. Bamber, J. A. Dowdeswell, N. W. Young, A. M. Le Brocq, R. C. Warner, A. J. Payne, D. D. Blankenship, T. D. Van Ommen, and M. J. Siegert. Evidence of a hydrological connection between the ice divide and ice sheet margin in the Aurora Subglacial Basin, East Antarctica. *Journal of Geophysical Research: Earth Surface*, 117(1):1–15, 2012. ISSN 21699011. doi: 10.1029/2011JF002066.

[107] D. A. Young, D. M. Schroeder, D. D. Blankenship, Scott D. Kempf, and E. Quartini. The distribution of basal water between Antarctic subglacial lakes from radar sounding. *Philosophical Transactions of the Royal Society A: Mathematical, Physical and Engineering Sciences*, 374(2059), 2016. ISSN 1364503X. doi: 10.1098/rsta.2014.0297.

[108] Hongju Yu, Eric Rignot, Helene Seroussi, and Mathieu Morlighem. Retreat of Thwaites Glacier, West Antarctica, over the next 100 years using various ice flow models, ice shelf melt scenarios and basal friction laws. *Cryosphere*, 12(12):3861–3876, 2018. ISSN 19940424. doi: 10.5194/tc-12-3861-2018.